

**Understanding radar backscatter sensitivity to vegetation water dynamics  
Sub-daily variations in ground-based experiments**

Vermunt, P.C.

**DOI**

[10.4233/uuid:1cd3a854-bd68-46ac-98f6-09db88bc0766](https://doi.org/10.4233/uuid:1cd3a854-bd68-46ac-98f6-09db88bc0766)

**Publication date**

2022

**Document Version**

Final published version

**Citation (APA)**

Vermunt, P. C. (2022). *Understanding radar backscatter sensitivity to vegetation water dynamics: Sub-daily variations in ground-based experiments*. [Dissertation (TU Delft), Delft University of Technology]. <https://doi.org/10.4233/uuid:1cd3a854-bd68-46ac-98f6-09db88bc0766>

**Important note**

To cite this publication, please use the final published version (if applicable).  
Please check the document version above.

**Copyright**

Other than for strictly personal use, it is not permitted to download, forward or distribute the text or part of it, without the consent of the author(s) and/or copyright holder(s), unless the work is under an open content license such as Creative Commons.

**Takedown policy**

Please contact us and provide details if you believe this document breaches copyrights.  
We will remove access to the work immediately and investigate your claim.

# Understanding radar backscatter sensitivity to vegetation water dynamics

Sub-daily variations in ground-based experiments



Paul Vermunt



**UNDERSTANDING RADAR BACKSCATTER  
SENSITIVITY TO VEGETATION WATER DYNAMICS**

SUB-DAILY VARIATIONS IN GROUND-BASED EXPERIMENTS





# **UNDERSTANDING RADAR BACKSCATTER SENSITIVITY TO VEGETATION WATER DYNAMICS**

**SUB-DAILY VARIATIONS IN GROUND-BASED EXPERIMENTS**

## **Proefschrift**

ter verkrijging van de graad van doctor  
aan de Technische Universiteit Delft,  
op gezag van de Rector Magnificus prof. dr. ir. T.H.J.J. van der Hagen,  
voorzitter van het College voor Promoties,  
in het openbaar te verdedigen op woensdag 13 juli 2022 om 15:00 uur

door

**Paul Christian VERMUNT**

Master of Science in Earth Sciences,  
Universiteit Utrecht, Nederland,  
geboren te Etten-Leur, Nederland.

Dit proefschrift is goedgekeurd door de

promotor: Prof. dr. ir. S.C. Steele-Dunne

promotor: Prof. dr. ir. N.C. van de Giesen

Samenstelling promotiecommissie:

Rector Magnificus,  
Prof. dr. ir. S.C. Steele-Dunne  
Prof. dr. ir. N.C. van de Giesen

voorzitter  
Technische Universiteit Delft  
Technische Universiteit Delft

*Onafhankelijke leden:*

Prof. dr. ir. W.G.M. Bastiaanssen  
Prof. dr. S.M. de Jong  
Prof. dr. L. Guerriero  
Prof. dr. J. Judge  
Dr. M. Vreugdenhil  
Prof. dr. ir. B.J.H. van de Wiel

Technische Universiteit Delft  
Universiteit Utrecht  
Tor Vergata Università Degli Studi di Roma, Italië  
University of Florida, USA  
Technische Universität Wien, Oostenrijk  
Technische Universiteit Delft, reservelid



*Keywords:* Microwave remote sensing, vegetation water content, diurnal cycle, leaf surface water, soil moisture, corn field, L-band, tower-based scatterometer

*Printed by:* Ipskamp Printing

*Front & Back:* Paul C. Vermunt

Copyright © 2022 by P. C. Vermunt

ISBN 978-94-6421-791-9

An electronic version of this dissertation is available at  
<http://repository.tudelft.nl/>.



# SUMMARY

Observing vegetation water dynamics from space offers insights into plant-water relations and water and carbon fluxes across ecosystems at local to global scales. A promising technique to observe water in the vegetation layer is radar, an active form of microwave remote sensing. Interactions between microwaves and vegetation material depend on dielectric properties of the vegetation tissue, which are a function of water content.

The research presented within this thesis aims to extend our physical understanding of the relationship between vegetation water dynamics and radar backscatter. The particular focus was on sub-daily dynamics, motivated by the dynamic nature of plant-water interactions and developments in the availability of sub-daily spaceborne radar observations. Moreover, we examined the effect of vertical water dynamics inside the vegetation layer on backscatter, which is relevant for better understanding which parts of the vegetation layer control the signal. To limit complexity, we focused on homogeneous corn fields. During ground-based experimental campaigns, we collected scatterometer data in vertical (VV), horizontal (HH) and cross (VH and HV) polarizations, and extensive measurements of water dynamics from these fields. These datasets were analyzed using statistical analyses and electromagnetic models.

First, we tested a common assumption that sub-daily changes in **vegetation water content (VWC)** have a negligible effect on backscatter (Chapter 3). Changes in water content were quantified from crop emergence to harvest. Here, we separated (a) **surface soil moisture (SSM)**, measured with sensors, (b) internal VWC, measured by means of destructive sampling, and (c) **surface canopy water (SCW)**, such as dew and rainfall interception, measured using leaf wetness sensors and geometric measurements. Next, variations in these 'moisture stores' were compared with variations in L-band radar backscatter, both on sub-daily and seasonal scales. In the early season, we found the largest sub-daily variations in backscatter, which were mainly due to changes in soil moisture and dew deposition on the soil surface. In mid- and late season, sub-daily backscatter patterns showed substantial similarities to SCW and the sap flow cycle. In addition, we found that VWC decreased by 0-20% between 6:00 and 18:00, while the backscatter coefficients also significantly dropped in this period. These results suggest that, in mid- and late season, both VWC and SCW play a much more important role in the sub-daily variation of radar backscatter than has often been assumed.

An important limitation of this study, and of many other studies on microwave observations of vegetation as well, is the lack of high temporal resolution VWC data. Without these data, it is difficult to separate and quantify signals from vegetation and soil. This should be addressed when we aim to understand and use sub-daily variations in microwave signals. Therefore, we investigated an alternative for the laborious and time-consuming destructive sampling during the day, using sap flow measurements and transpiration estimates (Chapter 4). This method allowed us to extrapolate VWC with a 15-

minute resolution. Our results showed that the water content in our corn varied by 10-20% during the day under non-stressed conditions, and up to 35% under stressed conditions. We also found that, from all polarizations, VV-pol was most sensitive to variations in VWC and SCW, closely followed by the average of the cross-pols. Moreover, backscatter variations during a typical dry day were two (HH- and cross-pol) to four (VV-pol) times more sensitive to the diurnal VWC cycle than to variations in soil moisture. Hence, with the 15-minute VWC extrapolations it was confirmed that the sub-daily variations of our radar backscatter observations were highly affected by VWC.

Finally, we also investigated the effect of the vertical moisture distribution within the vegetation layer on radar backscatter (Chapter 5). The goal was to understand which parts of the vegetation layer control the backscatter dynamics. Through destructive sampling, we found that the largest diurnal changes in VWC originated from the lower parts of the stems and the largest leaves and ears in the center of the plant. By placing leaf wetness sensors on different heights across the corn plants, we found that dew was deposited mainly in the upper and middle parts, and rainfall was intercepted throughout the entire plant. These results were used to divide the widely used *Water Cloud Model* (WCM) into three different layers. The model simulations suggest that, from mid-season onward, total backscatter was largely controlled by water in the layer with the largest leaves, 50-100 cm above the ground, which also contained the ears in the late season. According to the simulations, the two-way attenuation of the microwaves by the vegetation layers leads to a smaller contribution from the lower 50 cm to the total radar backscatter, while the top 100 cm is semi-transparent due to low water storage in that layer. These results show the importance of taking the vertical moisture distribution of a vegetation layer into account when studying the contribution of vegetation to backscatter.

Ultimately, understanding backscattering from a vegetated area will remain challenging because of complex interactions between microwaves, vegetation and soil. This thesis builds towards further understanding backscatter time series by using unique field observations with unprecedented detail. For the first time, variations in radar backscatter were linked to continuous, separate measurements of internal vegetation water content, surface canopy water and soil moisture. Insights from the field campaigns and modelling studies provide a foundation for further research on the opportunities for sub-daily and multi-frequency radar. Certainly, sub-daily radar has the potential to become an important source of data for local to global scale studies on processes related to vegetation water dynamics.



# SAMENVATTING

Het observeren van vegetatiewaterdynamiek vanuit de ruimte biedt inzichten in plant-water relaties en water- en koolstoffluxen in ecosystemen op lokale tot mondiale schaal. Een veelbelovende techniek om vegetatiewater te observeren is radar, een actieve vorm van microgolf remote sensing. Interacties tussen microgolven en vegetatiemateriaal worden bepaald door diëlektrische eigenschappen van het vegetatieweefsel, die op hun beurt een functie zijn van watergehalte.

Het onderzoek gepresenteerd in deze scriptie heeft als doel om ons fysiek begrip van de relatie tussen vegetatiewaterdynamiek en radarweerkaatsing uit te breiden. De nadruk lag in het bijzonder op de sub-dagelijkse dynamiek, gemotiveerd door de dynamische aard van plant-water interacties en ontwikkelingen in de beschikbaarheid van sub-dagelijkse observaties van radarweerkaatsing uit te ruimte. Bovendien onderzochten we het effect van verticale waterdynamiek in de vegetatielaag op radarweerkaatsing, wat relevant is om beter te begrijpen welke delen van de vegetatielaag het signaal beheersen. Om complexiteit te beperken hebben we ons gericht op homogene maïsvelden. Tijdens experimenteel veldonderzoek verzamelden we scatterometer data in verticale (VV), horizontale (HH), en kruis (VH en HV) polarisaties, en omvangrijke metingen van waterdynamiek in deze velden. Deze datasets werden geanalyseerd met behulp van statistische analyse en elektromagnetische modellen.

Ten eerste testten we de vaak gedane aanname dat sub-dagelijkse veranderingen in **vegetatiewatergehalte (VWG)** een verwaarloosbaar effect hebben op radarweerkaatsing (Hoofdstuk 3). Van opkomst van het gewas tot de oogst werden veranderingen van watergehalte gekwantificeerd. Hierbij werd onderscheid gemaakt tussen (a) bodemvocht aan de oppervlakte, gemeten met sensoren, (b) intern VWG, gemeten door middel van destructieve bemonstering, en (c) **vegetatie- oppervlaktewater (VOW)**, zoals dauw en regenvalinterceptie, gemeten met behulp van bladvochtigheidssensoren en geometrische metingen. Variaties in deze drie 'vochtreservoirs' werden vervolgens vergeleken met variaties in L-band radarweerkaatsing, zowel op sub-dagelijkse- als seizoensschaal. In het vroege seizoen vonden we de grootste dagelijkse variaties in radarweerkaatsing, die met name toegeschreven konden worden aan veranderingen in bodemvocht en dauwafzetting op het grondoppervlak. In het midden- en late seizoen toonden sub-dagelijkse patronen in radarweerkaatsing substantiële gelijkenissen met VOW en de omgekeerde sapstroomcyclus. Daarnaast vonden we dat VWG tot 20% verminderde tussen 6:00 en 18:00, terwijl radarweerkaatsing ook significant daalde in deze periode. Deze resultaten suggereren dat, in het midden- en late seizoen zowel VGW als VOW een veel belangrijker rol spelen in de dagelijkse variatie van radarweerkaatsing dan tot nu toe vaak werd aangenomen.

Een belangrijke beperking van deze studie, en ook van vele andere studies naar microgolfobservaties van vegetatie, is het gebrek aan VWG gegevens met hoge temporele resolutie. Zonder deze data is het moeilijk om signalen van vegetatie of bodem te schei-

den en te kwantificeren. Dit zal moeten worden aangepakt wanneer we sub-dagelijkse variaties in microgolfsignalen willen begrijpen en gebruiken. Daarom onderzochten we een alternatief voor de arbeid- en tijdrovende destructieve bemonsteringsmethode om VWG te meten (Hoofdstuk 4). Variatie in VWG werd bepaald middels een methode gebaseerd op de waterbalans: sapstroom (in) en transpiratie (uit). Deze methode maakte het mogelijk VWG te bepalen met een resolutie van 15 minuten. Uit de resultaten bleek dat het vochtgehalte in onze maïsplanten dagelijks met 10-20% varieerde onder normale condities, en tot 35% tijdens waterstress. Verder vonden we dat, van alle polarisaties, VV-pol het meest gevoelig was voor variaties in VWG en VOW, gevolgd door het gemiddelde van de kruis-polarisaties. Op een typische droge dag was het zelfs zo dat de variatie van radarweerkaatsing gedurende de dag twee (HH- en kruis-pol) tot vier (VV-pol) keer meer bepaald werd door de dagelijkse VWG cyclus dan door variatie in bodemvocht. Met behulp van de geëxtrapoleerde VWG gegevens werd dus bevestigd dat VWG grote invloed had op de sub-dagelijkse variaties van onze radarweerkaatsingsobservaties.

Tot slot onderzochten we ook wat het effect van de verticale vochtverdeling is binnen de vegetatielaag op radarweerkaatsing (Hoofdstuk 5). Het doel hiervan was om te begrijpen welke delen van de planten het radarsignaal het meeste bepalen. Door destructieve bemonstering vonden we dat de grootste dagelijkse veranderingen in VWG voornamelijk kwamen uit de onderste delen van de stengels, en de grootste bladeren en maïskolven in het midden van de plant. Met behulp van bladvochtigheidssensoren, geplaatst op verschillende hoogtes langs de maïsplanten, vonden we dauwafzettingen vooral op de bovenste en middelste delen van de plant, en regeninterceptie overal. Deze resultaten hebben we gebruikt om het veelgebruikte *Water Cloud Model* (WCM) in drie verschillende lagen op te delen. De modelsimulaties suggereerden dat, vanaf het midden van het seizoen, de totale radarweerkaatsing grotendeels bepaald werd door het water in de laag met de grootste bladeren, op 50-100 cm boven de grond, die in het late seizoen ook de kolven bevatte. De uitdoving van de golven door de vegetatielaag zorgden er volgens de simulaties voor dat de onderste 50 cm een kleinere bijdrage heeft aan de totale radarweerkaatsing, terwijl de bovenste 100 cm semi-transparant is. Deze resultaten laten zien waarom het van belang is om de verticale vochtverdeling van een vegetatielaag mee te nemen wanneer de bijdrage van deze vegetatie op radarweerkaatsing wordt bestudeerd.

Uiteindelijk zal het begrip van radarweerkaatsing van een begroeid gebied een uitdaging blijven vanwege de complexe interacties tussen microgolven, vegetatie en bodem. Deze scriptie bouwt verder aan een beter begrip van radarweerkaatsingstijdreeksen door gebruik te maken van unieke veldwaarnemingen met ongekende details. Voor het eerst werden veranderingen in radarweerkaatsing gelinkt aan continue, aparte metingen van intern VWG, VOW en bodemvocht. Inzichten van de veldcampagnes en modelstudies vormen een basis voor verder onderzoek naar de kansen voor sub-dagelijkse en multi-frequentie radar. Het staat buiten kijf dat sub-dagelijkse radar de potentie heeft om een belangrijke bron van data te zijn voor studies naar processen gerelateerd aan vegetatie-waterdynamiek.



# NOMENCLATURE

## List of abbreviations

|            |                                                                    |
|------------|--------------------------------------------------------------------|
| ASCAT      | Advanced Scatterometer                                             |
| BBCH       | Biologische Bundesanstalt, Bundessortenamt und CHEmische Industrie |
| CDF        | Cumulative Distribution Function                                   |
| ESA        | European Space Agency                                              |
| FAO        | Food and Agriculture Organization of the United Nations            |
| FAWN       | Florida Automated Weather Network                                  |
| GEO        | Geosynchronous Equatorial Orbit                                    |
| Globe-LFMC | Global database of Live Fuel Moisture Content                      |
| GNSS       | Global Navigation Satellite System                                 |
| HH         | Horizontal transmit and Horizontal receive                         |
| HV         | Horizontal transmit and Vertical receive                           |
| IEM        | Integral Equation Method                                           |
| IFAS       | Institute of Food and Agricultural Sciences                        |
| ISRO       | Indian Space Research Organisation                                 |
| KGE        | Kling-Gupta Efficiency                                             |
| LAI        | Leaf Area Index                                                    |
| LEO        | Low Earth Orbit                                                    |
| MEO        | Medium Earth Orbit                                                 |
| MicroWEX   | Microwave Water and Energy Balance Experiment                      |
| MIMICS     | Michigan Microwave Canopy Scattering model                         |
| NASA       | National Aeronautics and Space Administration                      |
| NISAR      | NASA-ISRO Synthetic Aperture Radar                                 |
| PolSAR     | Polarimetric Synthetic Aperture Radar                              |
| RCM        | RADARSAT Constellation Mission                                     |
| ROSE-L     | Radar Observing System for Europe - L-Band                         |
| SAR        | Synthetic Aperture Radar                                           |
| SMAP       | Soil Moisture Active Passive                                       |
| SSM        | Surface Soil Moisture                                              |
| TVM        | Tor Vergata discrete backscatter and emission Model                |
| UF-LARS    | University of Florida L-band Automated Radar System                |
| VH         | Vertical transmit and Horizontal receive                           |
| VOD        | Vegetation Optical Depth                                           |
| VV         | Vertical transmit and Vertical receive                             |
| WCM        | Water Cloud Model                                                  |
| XP         | Cross-Polarized - averaged VH and HV                               |

**List of symbols**

|                   |                                                                                           |
|-------------------|-------------------------------------------------------------------------------------------|
| $\Psi_{soil}$     | Soil water potential [kPa]                                                                |
| $\rho_{plant}$    | Plant density [ $\text{m}^{-2}$ ]                                                         |
| $\sigma^0$        | Backscatter coefficient [dB]                                                              |
| $\sigma_{HH}^0$   | Horizontally polarized backscatter [dB]                                                   |
| $\sigma_{obs}^0$  | Observed backscatter coefficient [dB]                                                     |
| $\sigma_{sim}^0$  | Simulated backscatter coefficient [dB]                                                    |
| $\sigma_{soil}^0$ | Soil contribution to backscatter [dB]                                                     |
| $\sigma_{veg}^0$  | Vegetation contribution to backscatter [dB]                                               |
| $\sigma_{VV}^0$   | Vertically polarized backscatter [dB]                                                     |
| $\sigma_{XP}^0$   | Cross-polarized backscatter [dB]                                                          |
| $\tau$            | Transmissivity [-]                                                                        |
| $\tau^2$          | Two-way transmission through the vegetation layer [-]                                     |
| $\theta$          | Volumetric soil moisture content [ $\text{m}^3\text{m}^{-3}$ ]                            |
| $\theta_I$        | Incidence angle [ $^\circ$ ]                                                              |
| $A_s$             | Sensor area [ $\text{m}^2$ ]                                                              |
| $A_{leaf}$        | Leaf area [ $\text{m}^2$ ]                                                                |
| $C$               | Water Cloud Model parameter [-]                                                           |
| $CW$              | Canopy Water [ $\text{kg m}^{-2}$ ]                                                       |
| $D$               | Water Cloud Model parameter [-]                                                           |
| $ET_0$            | Reference evapotranspiration [ $\text{mm 15min}^{-1}$ ]                                   |
| $F$               | Sap flow [ $\text{mm 15min}^{-1}$ ]                                                       |
| $H$               | Height of the vegetation [m]                                                              |
| $I$               | Irrigation [ $\text{mm 15min}^{-1}$ ]                                                     |
| $l$               | Leaf length [m]                                                                           |
| $m_d$             | Dry biomass [kg]                                                                          |
| $m_f$             | Fresh biomass [kg]                                                                        |
| $M_g$             | Gravimetric moisture content [-]                                                          |
| $M_w$             | Mass of surface water on sensor or leaf [kg]                                              |
| $P$               | Precipitation [ $\text{mm 15min}^{-1}$ ]                                                  |
| $R_s$             | Solar radiation [ $\text{W m}^{-2}$ ]                                                     |
| $SCW$             | Surface Canopy Water [ $\text{kg m}^{-2}$ ]                                               |
| $T$               | Temperature [ $^\circ\text{C}$ ]                                                          |
| $T$               | Transpiration [ $\text{mm 15min}^{-1}$ ]                                                  |
| $VWC$             | Vegetation Water Content [ $\text{kg m}^{-2}$ ]                                           |
| $W$               | Volumetric water content of the vegetation layer in the WCM [ $\text{m}^3\text{m}^{-3}$ ] |
| $w$               | Leaf width [m]                                                                            |

# CONTENTS

|                                                                                                           |            |
|-----------------------------------------------------------------------------------------------------------|------------|
| <b>Summary</b>                                                                                            | <b>v</b>   |
| <b>Samenvatting</b>                                                                                       | <b>vii</b> |
| <b>Nomenclature</b>                                                                                       | <b>ix</b>  |
| <b>1 Introduction</b>                                                                                     | <b>1</b>   |
| 1.1 The importance of monitoring vegetation water dynamics from space . . . .                             | 2          |
| 1.2 Developments in radar remote sensing of vegetation . . . . .                                          | 2          |
| 1.3 Research gaps and objectives . . . . .                                                                | 3          |
| 1.4 Thesis outline . . . . .                                                                              | 5          |
| <b>2 Field campaigns and instrumentation</b>                                                              | <b>7</b>   |
| 2.1 Campaigns . . . . .                                                                                   | 8          |
| 2.1.1 Citra 2018 . . . . .                                                                                | 8          |
| 2.1.2 Reusel 2019 . . . . .                                                                               | 9          |
| 2.2 Instrumentation and sampling . . . . .                                                                | 9          |
| 2.2.1 UF-LARS . . . . .                                                                                   | 9          |
| 2.2.2 Hydrometeorological sensors . . . . .                                                               | 10         |
| 2.2.3 Manual measurements. . . . .                                                                        | 13         |
| <b>3 Response of Sub-daily L-Band Backscatter to Internal and Surface Canopy Water Dynamics</b>           | <b>15</b>  |
| 3.1 Introduction . . . . .                                                                                | 16         |
| 3.2 Materials and Methods . . . . .                                                                       | 19         |
| 3.2.1 Study site . . . . .                                                                                | 19         |
| 3.2.2 Radar backscatter . . . . .                                                                         | 19         |
| 3.2.3 Hydrometeorology. . . . .                                                                           | 19         |
| 3.2.4 Vegetation sampling and monitoring . . . . .                                                        | 22         |
| 3.3 Results . . . . .                                                                                     | 22         |
| 3.3.1 Hydrometeorology. . . . .                                                                           | 22         |
| 3.3.2 Vegetation development and water content . . . . .                                                  | 23         |
| 3.3.3 Backscatter . . . . .                                                                               | 24         |
| 3.4 Discussion . . . . .                                                                                  | 31         |
| 3.5 Conclusions. . . . .                                                                                  | 34         |
| <b>4 Extrapolating Continuous Vegetation Water Content to Understand Sub-daily Backscatter Variations</b> | <b>39</b>  |
| 4.1 Introduction . . . . .                                                                                | 40         |
| 4.2 Estimating diurnal variations in tree water content using sap flow probes . .                         | 41         |

|          |                                                                                                                        |            |
|----------|------------------------------------------------------------------------------------------------------------------------|------------|
| 4.3      | Data and methods . . . . .                                                                                             | 42         |
| 4.3.1    | Applying the sap flow approach to estimate diurnal variations in corn VWC . . . . .                                    | 42         |
| 4.3.2    | Interpreting the behaviour of sub-daily L-band backscatter . . . . .                                                   | 45         |
| 4.4      | Results . . . . .                                                                                                      | 48         |
| 4.4.1    | Seasonal and diurnal variation of vegetation water content . . . . .                                                   | 48         |
| 4.4.2    | Reconstructions of continuous, sub-daily variations in vegetation water content . . . . .                              | 48         |
| 4.4.3    | Reconstructing a record of multiple days. . . . .                                                                      | 51         |
| 4.4.4    | The effect on sub-daily L-band backscatter . . . . .                                                                   | 52         |
| 4.5      | Discussion . . . . .                                                                                                   | 55         |
| 4.5.1    | Sub-daily vegetation water content estimates: observations and reconstructions . . . . .                               | 55         |
| 4.5.2    | Interpreting sub-daily backscatter . . . . .                                                                           | 59         |
| 4.6      | Conclusions. . . . .                                                                                                   | 60         |
| <b>5</b> | <b>Towards Understanding the Role of Vertical Canopy Moisture Distribution on Radar Backscatter Dynamics</b> . . . . . | <b>63</b>  |
| 5.1      | Introduction . . . . .                                                                                                 | 64         |
| 5.2      | Materials and Methods . . . . .                                                                                        | 65         |
| 5.2.1    | Experimental sites . . . . .                                                                                           | 65         |
| 5.2.2    | Vertical distribution of moisture . . . . .                                                                            | 65         |
| 5.2.3    | Backscatter data . . . . .                                                                                             | 67         |
| 5.2.4    | Water Cloud Model . . . . .                                                                                            | 67         |
| 5.3      | Results and discussion . . . . .                                                                                       | 69         |
| 5.3.1    | Seasonal changes of internal vegetation water distribution . . . . .                                                   | 69         |
| 5.3.2    | Sub-daily changes of internal vegetation water distribution . . . . .                                                  | 72         |
| 5.3.3    | Distribution of surface water: dew and rainfall interception . . . . .                                                 | 73         |
| 5.3.4    | Multi-layer WCM: seasonal variations . . . . .                                                                         | 74         |
| 5.3.5    | Multi-layer WCM: sub-daily variations. . . . .                                                                         | 76         |
| 5.4      | Conclusions. . . . .                                                                                                   | 78         |
| <b>6</b> | <b>Conclusions</b> . . . . .                                                                                           | <b>81</b>  |
| 6.1      | Main Findings. . . . .                                                                                                 | 82         |
| 6.2      | Implications . . . . .                                                                                                 | 83         |
| 6.3      | Directions for Further Research. . . . .                                                                               | 84         |
| 6.3.1    | Calibration/validation campaigns for microwave remote sensing of vegetation . . . . .                                  | 84         |
| 6.3.2    | Electromagnetic Modelling . . . . .                                                                                    | 86         |
| 6.4      | Concluding Remarks . . . . .                                                                                           | 87         |
|          | <b>References</b> . . . . .                                                                                            | <b>89</b>  |
|          | <b>Acknowledgements</b> . . . . .                                                                                      | <b>107</b> |
|          | <b>Curriculum Vitae</b> . . . . .                                                                                      | <b>109</b> |
|          | <b>List of Publications</b> . . . . .                                                                                  | <b>111</b> |

# 1

## INTRODUCTION

## 1.1. THE IMPORTANCE OF MONITORING VEGETATION WATER DYNAMICS FROM SPACE

Vegetation water dynamics refers to the presence and motion of water in a vegetation layer. This involves processes related to water inside vegetation tissue and water on top of vegetation surfaces, such as dew and rainfall interception. Monitoring these dynamics is crucial for applications related to (1) the health and performance of the vegetation itself, and (2) large-scale processes which are affected by vegetation-water interactions.

Dynamics in internal vegetation water content (VWC) reflect the balance of transpiration and root water uptake. Progressive dehydration occurs when transpiration exceeds root water uptake for multiple days in a row. Anomalies in the shape of the diurnal cycle of VWC can be an early warning signal for drought-induced water stress, which affects the physiological functions and growth of the vegetation (Konings et al., 2021; Nelson et al., 2018; Porporato et al., 2001; Rahman and Hasegawa, 2012; Reddy et al., 2004; Shao et al., 2008; van Emmerik et al., 2015). Consequently, VWC as a measure of plant water status has important implications for assessing the health of both natural vegetation and agricultural crops (Yebra et al., 2019).

In addition to being of direct relevance for ecosystem health, vegetation water dynamics play a crucial role in the regulation of water movement between land and atmosphere, and with that, the coupled energy and carbon cycles. Spatiotemporal observations of vegetation water dynamics are therefore essential for the parameterization of ecohydrological and land-surface models (Cosh et al., 2009; Konings et al., 2019; Nelson et al., 2018; Tian et al., 2018). There is particular need for an improved understanding of rapid (<hour), fine-scale (10-20 km) hydrological processes (Hobbs et al., 2019; Trenberth and Asrar, 2014). Remote sensing offers the possibility to cover large areas and provide spatiotemporal model inputs. A remote sensing technique of particular interest is radar (RADio Detection And Ranging), because of its sensitivity to VWC and its ability to ensure timely data.

## 1.2. DEVELOPMENTS IN RADAR REMOTE SENSING OF VEGETATION

Radar instruments operate in the microwave region of the electromagnetic spectrum, with wavelengths of 0.5-100 cm, or 0.3-300 GHz in terms of frequency. Low-frequency microwaves (up to ~10 GHz) are able to penetrate cloud cover, and are therefore most suitable to ensure timely observations of the Earth's surface (Steele-Dunne et al., 2017). A radar antenna transmits a radio wave in the direction of a target, and measures the part of the echo that reflects back towards the antenna, which is called *backscatter*. The strength (amplitude) of the backscatter depends on the properties of a target, i.e. geometry and dielectric constant. The dielectric constant is the main property of a material describing the interaction with an electromagnetic field. A higher dielectric constant is associated with stronger scattering. Hence, the large contrast between the dielectric constants of water and soil particles is the fundamental basis for the development of radar as an earth observation tool to measure surface soil moisture content (Wang and Qu, 2009). The geometry of a target determines the direction of the scattering and thus

the portion of the scattering that returns to the antenna as backscatter.

From early field experiments with truck-mounted radar instruments in the 1970s, it was found that the correlation between backscatter and soil moisture reduced with vegetation cover, particularly for the higher frequencies (Dickey et al., 1974; Ulaby et al., 1975; Ulaby, 1974, 1975). Since then, small-scale experiments and large-scale field campaigns have been set up, and empirical, semi-empirical and physical models have been developed, aiming to (1) understand the complex interactions between microwaves, vegetation and soil and (2) extract information from the acquired radar imagery, often primarily for isolating soil moisture from other signals (Attema and Ulaby, 1978; Bracaglia et al., 1995; El-rayes and Ulaby, 1987; Joseph et al., 2010; Y. Kim and van Zyl, 2009; Kurum et al., 2009; Ulaby and El-rayes, 1987; Ulaby et al., 1990). In general, it was found that total backscatter from a vegetated surface is the sum of backscatter from the soil, which is decreased by the two-way attenuation of the vegetation layer, backscatter from the vegetation, governed by its water content and geometry, and backscatter from soil-vegetation interactions (Steele-Dunne et al., 2017; Wang and Qu, 2009). Whether backscatter is dominated by contributions from soil or vegetation depends on the configurations of the radar instrument, i.e. frequency, incidence angle, and polarization.

The increased understanding of microwave interactions with vegetation aided the development of several other applications. The launch of the first synthetic aperture radar (SAR) systems since 1978 (Woodhouse, 2017) led to the availability of higher resolution backscatter data (meters instead of kilometers with scatterometers), which advanced the development of applications such as land cover classification (Cloude and Pottier, 1997; Qi et al., 2012), monitoring biomass accumulation (Santoro et al., 2015; Yu and Saatchi, 2016), monitoring crop phenological stage (Khabbazan et al., 2019; Vreugdenhil et al., 2018) and detection of deforestation (Reiche et al., 2018; Thiel et al., 2006). Moreover, the sensitivity to vegetation water content (VWC) has been used in studies on plant water response to drought (Frolking et al., 2011; Saatchi et al., 2013) and forest fire susceptibility (Leblon et al., 2002; Saatchi et al., 2007).

The applications are constrained by satellite revisit times of multiple days, and single-frequency acquisitions. However, current developments in satellite radar mission design suggest that sub-daily radar becomes available in the next decades (Hobbs et al., 2019; Hu et al., 2016). In fact, commercial X-band (9.65 GHz) SAR system constellations are already being populated in Low Earth Orbit, and should be capable of delivering hourly data within a couple of years (Farquharson et al., 2021; Ignatenko et al., 2020). These developments suggest that the potential applications of spaceborne radar are now expanding to the measurement of rapid processes, such as diurnal vegetation water dynamics.

### 1.3. RESEARCH GAPS AND OBJECTIVES

The future availability of sub-daily spaceborne radar data offers a unique opportunity to study vegetation water dynamics from local to global scale with unprecedented detail. However, there are a lot of open questions to be answered to understand the full potential of these developments. Most importantly, the extent to which vegetation water dynamics affect variations in radar backscatter, particularly at sub-daily scale, is still poorly understood. This thesis aims to extend our physical understanding of this relationship.



It is often assumed that the influence of sub-daily variations in internal VWC and surface canopy water (SCW), i.e. dew and rainfall interception, on backscatter is negligible. However, there are clear indications that this assumption is invalid. Some studies found structural differences between morning and evening overpass backscatter from scatterometers in sun-synchronous orbits with Ku-band (13.4 GHz; Frolking et al., 2011) and C-band (5.3 GHz; Friesen et al., 2012; Schroeder et al., 2016; Steele-Dunne et al., 2019; Wood et al., 2002) frequencies. Other studies found diurnal cycles in aggregated backscatter data from a Ku-band (13.5 GHz) scatterometer in a non-sun-synchronous orbit (Konings et al., 2017; Paget et al., 2016; van Emmerik et al., 2017). Given that penetration depths for these frequencies are low, backscatter should have been mainly sensitive to the vegetation layer (Dickey et al., 1974; Z.-L. Li et al., 2021; Ulaby et al., 1984). Because changes in vegetation structure should be low on a sub-daily timescale, these results suggest that sub-daily variations in VWC and/or SCW are sufficiently detectable with spaceborne radar.

To support this hypothesis, reference can be made to ground-based experiments, in which tower-based backscatter observations are related to *in situ* field measurements. Brisco et al., 1990 for example related two full days of destructively sampled gravimetric moisture content of wheat plants and soil to variations in backscatter observations from a Ku-, C- and L-band truck-mounted scatterometer. It was shown that C- and L-band sub-daily variability was comparable to the diurnal cycle of plant moisture content when plant moisture content was high, and comparable to soil moisture variations when plant moisture content was low. Gillespie et al., 1990 used the same instrument to conclude that the presence of dew, assessed by visual inspection, indeed had an effect on backscatter by comparing backscatter patterns between one night with and one night without dew. Other experiments found relations between the amount of rainfall interception from trees to variations in X-band (8.9 -10.4 GHz) backscatter and attenuation (Bouten et al., 1991; De Jong et al., 2002).

These ground-based experiments are crucial for a fundamental understanding of backscatter sensitivity to sub-daily vegetation water dynamics. However, the experiments are sparse and the data sets too limited to quantify the relative importance of VWC, SCW and soil moisture on sub-daily backscatter variations. Moreover, the extent to which water storage in an aboveground vegetation layer varies on a sub-daily level is poorly described in literature, due to the difficulty and labor intensity of the measurements. Hence, the first objective of this dissertation is to **quantify the sub-daily variation of water storage in the aboveground vegetation layer, both internal VWC and external SCW, and to understand how these, together with surface soil moisture, control sub-daily variations in backscatter.**

To better understand the effect of vegetation water dynamics on backscatter, we should not only focus on the total aboveground VWC or SCW. We also need to know which parts of the vegetation layer control that backscatter. This is first and foremost important for a good interpretation of the radar observations. In addition, it offers possibilities for the development of multi-frequency radars, with different penetration depths, to retrieve information from the vertical profile of the vegetation layer. From studies on backscatter sensitivity to soil moisture, it is known that, in general, lower frequencies penetrate deeper into the vegetation layer than higher frequencies (Dickey et al.,

1974; Z.-L. Li et al., 2021; Ulaby et al., 1984). However, backscatter sensitivity to different depths or layers in the canopy is poorly understood.

Some studies have incorporated two vertical vegetation layers into physical models (Link et al., 2022; Ulaby et al., 1990) and the semi-empirical Water Cloud Model (WCM; Hoekman, 1987; L. Liu et al., 2012; Ulaby et al., 1984). Although these studies provide useful insights in the importance of vertical inhomogeneity of moisture on backscatter, the differences between the layers were not based on a realistic vertical distribution of moisture in the vegetation layer. A lack of observational data to describe the vertical moisture distribution limits the research on this issue. Hence, the second objective of the work presented in this dissertation is to **measure the vertical distribution of moisture in the vegetation layer, and to incorporate a realistic distribution in a multi-layer WCM to better understand which parts of the vegetation layer control the backscatter dynamics.**

The measurements were conducted in two ground-based experiments. Corn was chosen as our main crop of interest for a couple of reasons. First, an agricultural crop such as corn is relatively simple and homogeneous, which makes it accessible to sample and model. There are already electromagnetic model versions for corn (e.g. Bracaglia et al., 1995), which makes calibration and validation using field observations easier. Second, peak corn water content can reach to around  $5 \text{ kg m}^{-2}$ , which is higher than most other crops and offers the opportunity to measure dominant control on backscatter from vegetation for the commonly used frequencies (X, C and L-band). Ultimately, if we can understand the relation between backscatter and vegetation water dynamics from a homogeneous agricultural field, that could be the start of a better understanding of more complex ecosystems.

## 1.4. THESIS OUTLINE

The contents presented in this dissertation are based on a description of the experimental set-up and three self-contained journal articles. Some overlap between these chapters may be present.

Chapter 2 presents an overview of the experimental set-ups and essential details about the instrumentation from the campaigns in Citra (FL,USA) and Reusel (NL). Chapter 3 presents the results from the campaign in Florida. For different stages in the season, we quantify fluctuations of internal and surface canopy water and soil moisture, and illustrate their effect on sub-daily patterns of L-band backscatter. A key limitation of this study, the absence of high resolution sub-daily VWC, is addressed in Chapter 4. In this chapter, we extrapolate a continuous record of internal VWC using sparse destructive vegetation sampling and hydrometeorological data. The resulting time series is used to quantify the separate effects of VWC, SCW and soil moisture on backscatter through multiple linear regression. Chapter 5 shifts focus from temporal variability to the influence of the vertical distribution of canopy water on backscatter. In particular, multi-layer model simulations were performed to understand which parts of the vegetation layer control the backscatter dynamics. Finally, Chapter 6 gives an overview of the main findings, along with implications and recommendations for further research.



# 2

## FIELD CAMPAIGNS AND INSTRUMENTATION

*The research presented in this dissertation is based on intensive experimental work. This chapter gives a concise overview of the experimental set-up for two campaigns: in Florida (2018), and in the Netherlands (2019). In addition, specifications about the instrument and measuring approaches, which were largely similar for both campaigns, are given. Specific information about the sensor installation, measurement frequency and data processing is further discussed in the related Chapters 3-5.*

---

Parts of this chapter have been published in:

Vermunt, P. C., Khabbazan, S., Steele-Dunne, S. C., Judge, J., Monsivais-Huertero, A., Guerriero, L., and Liu, P. W. (2020). Response of Subdaily L-Band Backscatter to Internal and Surface Canopy Water Dynamics., *IEEE Transactions on Geoscience and Remote Sensing* **59**, (9), 7322 - 7337.

Vermunt, P. C., Steele-Dunne, S. C., Khabbazan, S., Judge, J., and Van de Giesen, N. C. (2022). Extrapolating Continuous Vegetation Water Content To Understand Sub-daily Backscatter Variations, *Hydrology and Earth System Sciences* **26**, 1223-1241 .

## 2.1. CAMPAIGNS

The purpose of the campaigns was to acquire data which helps us to understand the relation between water dynamics in the field and variations in radar backscatter. Water storage and movement was measured using a combination of hydrometeorological sensors and destructive sampling. Time series of the backscatter coefficients were acquired from ground-based scatterometer observations.

There are substantial similarities between the experimental campaigns. However, major differences include the availability of backscatter observations, the frequency of the destructive sampling and the type of corn. These will be discussed in sections 2.1.1 and 2.1.2. In both campaigns, the field set-up was organized around the observations from a multi-frequency (X-, C-, and L-band) scatterometer. Unfortunately, the data from this instrument could not be used due to system failure. Hence, the measurements from this system are not further discussed in this dissertation. However, because of its importance for the experimental set-up, the footprint of this system is included in the schematic overviews of the campaigns (Fig. 2.1 and 2.2).

### 2.1.1. CITRA 2018

The field experiments conducted for the research presented in this dissertation were part of the larger MicroWEX-12 (Microwave Water and Energy Balance Experiment, no. 12) project. MicroWEX-12 was conducted at the UF/IFAS Extension Plant Science Research and Education Unit (PSREU), Citra, Florida (29.410° N, 82.179° W), in Spring 2018. Figure 2.1 shows a schematization of the experimental set-up. The sensors and areas which were related to other studies were not included in this map.

On a sandy soil (>90% sand), sweet corn (*Zea mays L. var. rugosa*) was grown in an east-west direction. The field was irrigated with a center-pivot irrigation system. On the north side of the field, two radar systems (UF-LARS and TUD-scat) acquired measurements adjacent to each other and perpendicular to the row direction. To avoid any radio frequency interference, the acquisitions from the microwave sensors were coordinated. Because TUD-scat failed, details of its measurements are excluded in this dissertation. However, the footprint of this scatterometer is included due to its importance for the field set-up. Figure 2.1 shows that the conservative footprints of UF-LARS (42m x 21m) and TUD-scat (70m x 35m) partly overlap. These conservative footprints are areas that are larger than the actual radar footprints. All sensors and hardware (section 3.2.3) were installed outside these footprints to avoid metal materials affecting the backscatter observations. In addition, all foot traffic within the radar footprints was avoided, to prevent any changes in soil roughness. Measurements of soil roughness, crop development (height, LAI, BBCH, geometry), and crop density (section 2.2.3) were conducted at numerous random locations outside the footprints. Destructive sampling (section 2.2.3) was performed in the designated areas, leaving no impact on sensor measurements. Cutting, weighing and drying of the samples was performed on the terrain of PSREU, close to the weather station. Soil moisture sensors were calibrated at Frazier-Rogers Hall at the University of Florida in Gainesville.

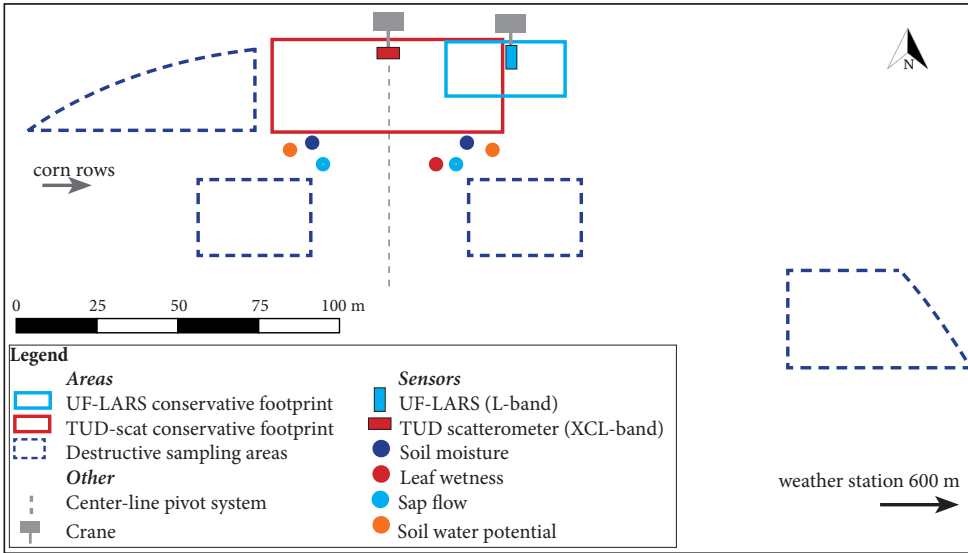


Figure 2.1: Schematization of the experimental set-up during the MicroWEX-12 campaign at Citra, Florida (29.410° N, 82.179° W), in 2018.

### 2.1.2. REUSEL 2019

A subsequent campaign was set up in Reusel, the Netherlands (51.319° N, 5.173° E), on the terrain of *Van den Borne Aardappelen* in the growing season of 2019. An important goal for this campaign was to capture the diurnal cycles of VWC. Figure 2.2 shows a schematization of the experimental set-up. The experimental design has many similarities with the MicroWEX-12 campaign.

Field corn was grown for silage on a sandy soil, and irrigated with a gun sprinkler irrigation system. A weather station was installed at the edge of the field, in between the corn field and a field with sugar beets. Cutting and weighing the fresh samples was performed in a shed on the terrain. Oven-drying and weighing the dry samples was performed in the WaterLab at Delft University of Technology. Because data from the TUD-scat system could not be used, no ground-based radar observations were available for this campaign.

## 2.2. INSTRUMENTATION AND SAMPLING

### 2.2.1. UF-LARS

Observations of radar backscatter coefficients ( $\sigma^0$ ) were acquired from the University of Florida L-band Automated Radar System (UF-LARS), a tower-based scatterometer (Figure 2.3). This system operates at a center frequency of 1.25 GHz, and is designed to collect data at four polarization combinations (HH, VV, HV and VH) with a dual polarization horn antenna. It was mounted on a Genie aerial work platform at a height of 14 m above the ground. From there, the field was scanned with a fixed incidence angle of 40°.

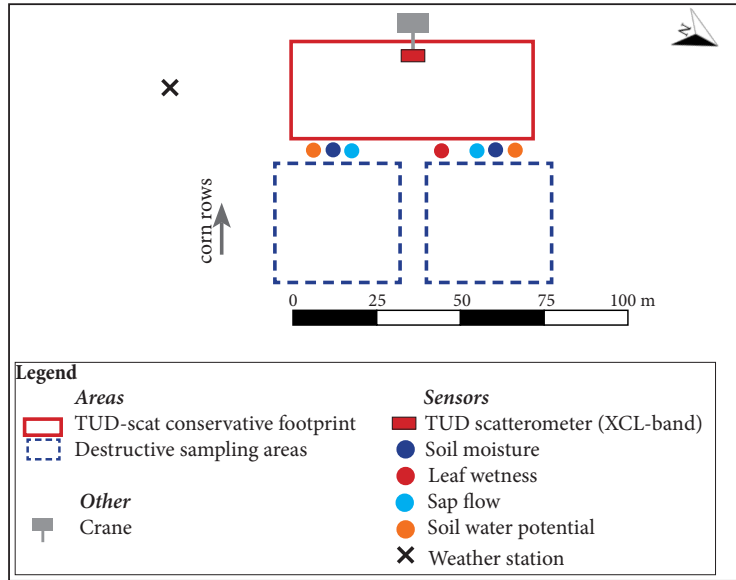


Figure 2.2: Schematization of the experimental set-up for the campaign at Reusel, the Netherlands (51.319° N, 5.173° E), in 2019.

The backscatter coefficients are computed using the Single Target Calibration Technique (STCT) (P.-W. Liu, 2013; Sarabandi and Ulaby, 1990). To suppress fading, 27 independent samples are averaged (P.-W. Liu et al., 2016); nine samples were taken at 30 MHz increments from 1130-1370 MHz, for each of the three azimuthal scans at  $-9^\circ$ ,  $0^\circ$ , and  $+9^\circ$ . The total error was estimated by P.-W. Liu et al., 2016 to be 1.71 dB, and includes a systematic error of 1.49 dB and a random error of 0.85 dB (fading). The systematic error was estimated, via error propagation, by combining the measurement errors of calibration target geometry (1.4 dB), ranges between antenna to terrain (0.17 dB) and calibration target (0.35 dB), and incidence angle (0.32 dB; Nagarajan et al., 2014).

Ground range and azimuth resolutions were calculated based on the 3 dB beamwidth of  $14.7^\circ$  in the E-plane and  $19.7^\circ$  in the H-plane (Nagarajan et al., 2014). The resulting single-scan footprints in HH, VV, and cross-pol were 40.0, 39.7, and 29.1 m<sup>2</sup>, respectively. An overview of the system specifications is given in Table 2.1. A full description of the system specifications can be found in Nagarajan et al., 2014 and P.-W. Liu et al., 2016.

### 2.2.2. HYDROMETEOROLOGICAL SENSORS

Hydrometeorological sensors were installed to acquire continuous (15 minute resolution) data on water storage and movement in the soil and vegetation layer.

#### LEAF WETNESS

Dielectric leaf wetness sensors, produced by METER Group (München, Germany), were installed to measure the surface water on the vegetation (see Fig. 2.4(a)). These sensors are designed to approximate thermodynamic and surface properties of actual leaves,



Table 2.1: UF-LARS system specifications

| Parameter                |            | UF-LARS                |
|--------------------------|------------|------------------------|
| Frequency (GHz)          |            | 1.25                   |
| 3dB Beamwidth (deg)      | E-plane    | 14.7                   |
|                          | H-plane    | 19.7                   |
| Bandwidth (MHz)          |            | 300                    |
| Antenna type             |            | Dual-polarization horn |
| Range resolution (m)     | HH/VV/XP   | 8.5/6.2/6.2            |
| Azimuth resolution (m)   | HH/VV/XP   | 4.7/6.4/4.7            |
| $NE\sigma^0$ (dB)        |            | -23.43/-25.58/-48.12   |
| Error in $\sigma^0$ (dB) | Systematic | 1.49                   |
|                          | Random     | 0.85                   |
| Incidence angle (deg)    |            | 40                     |
| Platform height (m)      |            | 14                     |



Figure 2.3: Scattermeters in Florida 2018 before sowing. The UF-LARS system is mounted to the blue crane (right).

which means that the presence of liquid water films and droplets on the sensors and leaves closely match (METER Group Inc., 2019). The sensors measure the dielectric constant of the sensor's upper surface, which is altered by the presence of water. The output signal [mV] is automatically converted to a universal scale called *counts*, to ensure that sensor outputs are universal regardless of the excitation voltage of the used data logger. For the EM50 data logger used here,  $\text{counts} = \text{voltage [mV]} / 0.733$  (METER Group Inc., 2019).

#### SAP FLOW

Sap flow sensors, produced by Dynamax Inc. (Houston, TX, USA), were installed from the moment the corn stems reached a 15 mm diameter. Flexible collar straps with built-

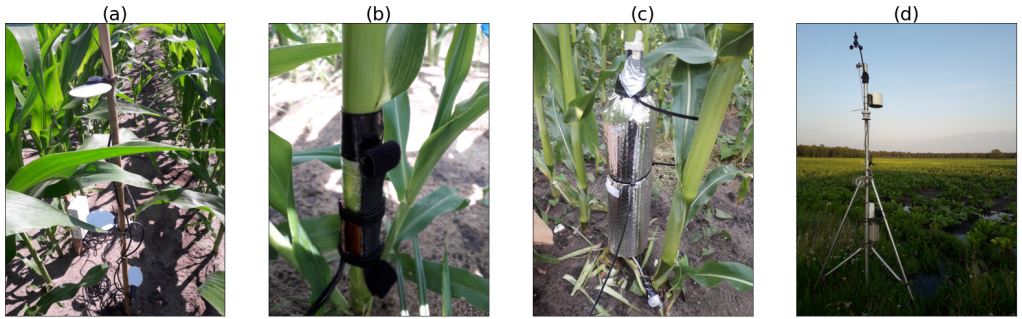


Figure 2.4: Hydrometeorological sensors, with (a) leaf wetness sensors, (b) sap flow sensor, (c) sap flow sensor after insulation, (d) weather station.

in heater strip and thermocouples are wrapped around the stems about 20 cm above the ground (see Fig. 2.4(b)), and then insulated and protected from environmental conditions such as rain and radiation (see Fig. 2.4(c)). The measurement is based on the stem heat balance theory (Sakuratani, 1981). The entire circumference of the stem receives a constant heat input from the heater strip. As sap movement carries heat, thermal dissipation corresponds to the sap flow rate. The change in temperature is used as a tracer for sap flow [ $\text{g h}^{-1}$ ], thereby taking into account the heat transfer to the stem tissue and the ambient air. The sensors were connected to a CR1000 Measurement and Control Datalogger produced by Campbell Scientific Inc. (Logan, UT, USA). This logger was powered by a 12V battery, which was charged by a solar panel (2018), or exchanged every few days with a fully charged battery (2019).

#### SOIL MOISTURE

To estimate volumetric soil moisture, EC-5 sensors (METER Group) were used. These sensors produce an output voltage that is dependent on the dielectric constant of the soil around the sensor. Factory calibration translates the output voltage into volumetric soil moisture ( $\text{m}^3\text{m}^{-3}$ ). For the campaign in Citra, 2018 (section 2.1.1), the sensors were calibrated in the laboratory using soil samples from the field, in five stages of dry down after saturating the soil. For the campaign in Reusel, 2019 (section 2.1.2), we used the factory calibration. Data was stored in EM50 loggers.

#### SOIL WATER POTENTIAL

Soil water potential was measured using T4e pressure transducer tensiometers (UMS GmbH, 2011). The measurement principle of these sensors is based on the difference between soil water tension, measured by a piezoelectric pressure sensor, and atmospheric pressure. A ceramic cup at the bottom of the tensiometer is water-permeable and gas-impermeable, and is used to transfer the soil water tension as a negative pressure into the tensiometer. This ceramic cup was regularly refilled externally through capillary tubes while it remained installed in the ground. The drier the soil, the more often a refill was required. The tensiometers were also connected to the CR1000 Datalogger.

### METEOROLOGICAL DATA

During the campaign in Citra, 2018 (section 2.1.1), open access data from the Florida Automated Weather Network (FAWN)<sup>1</sup> were used to obtain meteorological data. This weather station was located <600 m east from the experimental site. Data from precipitation, air temperature, solar radiation, relative humidity and wind speed with 15-min frequency were downloaded.

For Reusel, 2019 (section 2.1.2), a weather station was installed within 100 meters from the other sensors and sampling areas (Fig. 2.4(d)), next to the corn field. This station collected precipitation with a ECH2O rain model ECRN-100 rain gauge, solar radiation with an Apogee SP-212 pyranometer, wind and gust speed and wind direction with a Davis Cup anemometer, and temperature and relative humidity with a HOBO Temperature/RH Smart Sensor model S-THB-M008.

### 2.2.3. MANUAL MEASUREMENTS

In addition to sensor observations, manual measurements were conducted to acquire data on vegetation water content, crop growth and soil roughness, which could not be measured with our *in situ* sensors.

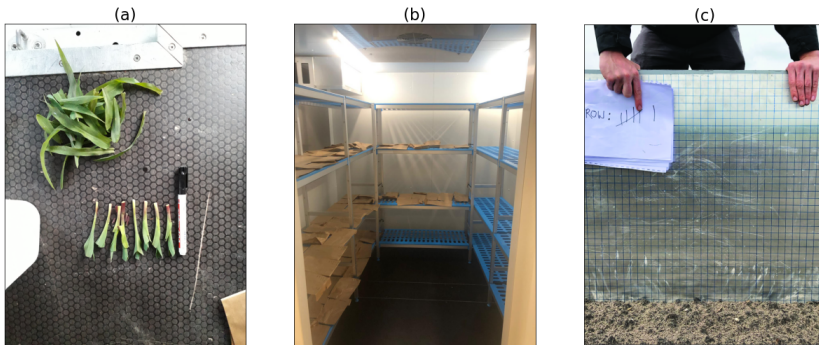


Figure 2.5: Manual measurements, with (a) destructive sampling, (b) walk-in oven for sampling drying, and (c) mesh board for roughness measurements.

### DESTRUCTIVE SAMPLING

Destructive sampling was conducted to acquire data on VWC and dry biomass. Samples were taken from designated sampling areas (Fig. 2.1 and 2.2). Each sampling time, a random meter was chosen along a random row, from which the two plants with an average height were taken. This was repeated three (Reusel, 2019) to four (Citra, 2018) times. To reduce water loss from the samples, they were cut and weighed as soon as possible in a cool shed or office. Stems, leaves, tillers, tassel and ears were separated (Fig. 2.5(a)) and labelled. Stems were cut in sections of 10 cm, and numerically labelled from the base (0-10 cm) to the top (e.g. 170-180 cm). Similarly, leaves were labelled from the base (leaf 1) to the top (e.g. leaf 15). Any surface water present on the plant tissue was removed with

<sup>1</sup><https://fawn.ifas.ufl.edu/data/>

paper towel before weighing. Constituents with the same labels were collected in paper bags and weighed to determine fresh biomass. Then, they were placed in a walk-in oven (Fig. 2.5(b)) and dried at 60 °C for 4-7 days, depending on the growth stage, i.e. the water content in the samples. Finally, the bags were weighed again to determine dry biomass.

### GROWTH MONITORING

Corn development was manually monitored. Height above the ground (m) was measured for each of the destructive samples. Phenological stages were determined using the *Biologische Bundesanstalt, Bundessortenamt and Chemical industry* (BBCH) scale for corn (Meier et al., 2009). Both row spacing and plants per meter were measured at 40 random locations in the field, from which plant density [ $\text{m}^{-2}$ ] was calculated. Regular measurements of leaf height, length and width were conducted, from which leaf areas were estimated assuming that corn leaves have an elliptical shape. Leaf area index (LAI) was derived from leaf areas and plant density.

### SOIL ROUGHNESS

Soil roughness measurements were conducted manually between sowing and emergence using a 1 m long meshboard (Fig. 2.5(c)), based on the approach described by Jang et al., 2005. On random locations outside the radar footprints, the meshboard was placed parallel, and perpendicular to the row direction. At each location, the meshboard was moved twice, and photographed, to collect a 3 m long image of the soil. The pictures from the soil surface disturbing the grid on the board were used to digitally estimate the soil root mean square height and correlation length.

# 3

## RESPONSE OF SUB-DAILY L-BAND BACKSCATTER TO INTERNAL AND SURFACE CANOPY WATER DYNAMICS

*The previous chapter gave an overview of the field experiments conducted for this thesis. Sensors and sampling strategies were carefully described. The results of this chapter are based on the intensive, sub-daily data collected in Citra, Florida, 2018. The motivation for this study is that the latest developments in radar mission concepts indicate that sub-daily SAR data will become available in the next decades. This chapter aims to quantify variations in water storage inside a corn canopy, and understand their effect on L-band backscatter observations.*

---

This chapter is based on:

Vermunt, P. C., Khabbazan, S., Steele-Dunne, S. C., Judge, J., Monsivais-Huertero, A., Guerriero, L., and Liu, P. W. (2020). Response of Subdaily L-Band Backscatter to Internal and Surface Canopy Water Dynamics., *IEEE Transactions on Geoscience and Remote Sensing* **59**, (9), 7322 - 7337.

### 3.1. INTRODUCTION

Global, daily to sub-daily monitoring of vegetation water dynamics is essential to address fundamental questions surrounding the role of vegetation in the climate system, and to provide information for a range of applications from agriculture and water management to weather prediction (Fisher et al., 2017). Vegetation temporally stores water inside its tissue and on its surface, and this water is transferred back to the climate system through transpiration and evaporation. Global evapotranspiration (ET) amounts from reanalysis data, land surface model and diagnostic products disagree by up to 50% (Jiménez et al., 2011; Mueller et al., 2013), and trends are uncertain (Mao et al., 2015). Uncertainty in ET partitioning is even more severe than uncertainty in estimating ET itself (S. T. Allen et al., 2020; Blyth and Harding, 2011). Lack of understanding of rainfall interception by vegetation and its loss through evaporation is a key limitation of current methods to estimate and partition ET, and is essential for land surface modelling and understanding the role of vegetation in land-atmosphere interactions (de Jong and Jetten, 2007; van Dijk et al., 2015). Robust modelling of interception is hindered by holes in our basic process understanding (S. T. Allen et al., 2020), and a lack of information about surface canopy water (SCW), i.e. water storage on vegetation surfaces as a result of dew formation or intercepted precipitation (Klamerus-Iwan et al., 2020). Furthermore, there is a fundamental need for leaf wetness monitoring to understand how projected changes in climate will influence the timing, frequency, duration and intensity of leaf wetting events and their effects on plant function in terms of water relations, gas exchange, energy balance, pathogens and pests, and reproduction (Dawson and Goldsmith, 2018).

A new perspective on ET and leaf wetness may be provided by sub-daily synthetic aperture radar (SAR), which gives direct insight into the mass balance of the vegetation. Active microwave remote sensing has been found to be sensitive to canopy water storage, depending on frequency, polarization, incidence angle, and vegetation cover (C. Allen and Ulaby, 1984; Brisco et al., 1990; El-rayes and Ulaby, 1987; Gillespie et al., 1990; Ulaby et al., 1975; Ulaby, 1975; Ulaby and El-rayes, 1987). This sensitivity has mainly been studied to account for the confounding effect of vegetation on soil moisture retrieval (e.g. Joseph et al., 2008; O'Neill et al., 1996; Ulaby, 1982). However, radar is also a valuable tool for vegetation monitoring, and well-suited to many applications including forest biomass and height (Quegan et al., 2019), change detection (Reiche et al., 2018), ecology and plant physiology (Konings et al., 2019), and agricultural crop classification and monitoring (Steele-Dunne et al., 2017). The launch of ESA's Sentinel-1 mission (Torres et al., 2012) in 2014 has accelerated the development of new applications for SAR in vegetation monitoring. By providing freely-available data at an unprecedented high temporal resolution, Sentinel-1 has stimulated rapid development of products for monitoring natural and agricultural landscapes. However, the repeat time of 6-12 days still limits the current state of the art to products related to biomass, leaf area index (LAI), phenological stage, change (e.g. harvest, tillage) and anomaly detection (El Hajj et al., 2019; Khabbazan et al., 2019; Mercier et al., 2020; Satalino et al., 2018; Veloso et al., 2017; Vreugdenhil et al., 2018). The RADARSAT Constellation Mission (RCM) was launched in 2019, and consists of three identical SAR satellites. The resulting denser temporal sampling of RCM (4-day revisit time) compared to RADARSAT-2 (12-day revisit time), is also expected to improve the potential of real-time agricultural monitoring with the



RADARSAT series (Mahdianpari et al., 2019).

The motivation for the current study is that the latest developments in radar mission concepts indicate that sub-daily SAR data will become available in the next decades. CapellaSpace<sup>1</sup> and Iceye<sup>2</sup> are currently populating constellations of X-band (~10 GHz) SAR systems in Low Earth Orbit (LEO), capable of delivering hourly data with resolutions of 10 m or less (e.g. Stringham et al., 2019). An alternative is to place a SAR instrument in a geostationary orbit. A mission of particular interest is HydroTerra, one of the candidates bidding to become the European Space Agency's 10th Pathfinder mission. HydroTerra, is a C-band (~5 GHz) geostationary (GEO) SAR mission which will deliver data at various spatial and temporal resolutions to meet the science needs of users (Hobbs et al., 2019). L-band (~1 GHz) geostationary SAR missions are also under development (Hu et al., 2016). With Medium Earth Orbit (MEO) SAR, at altitudes between those of LEO and GEO, trade-offs in system and orbit parameters allow a range of possibilities in terms of spatial and temporal resolution (Matar et al., 2020). The goal of this chapter is to demonstrate the potential value of sub-daily SAR to monitor internal and surface canopy water, and exploit this emerging technology as a tool to address fundamental challenges in our understanding of the role of vegetation in the climate system.

Several studies have demonstrated that spaceborne radar is capable of detecting plant water variations during the day. Konings et al., 2017, Paget et al., 2016, and van Emmerik et al., 2017, used aggregated data from the non-sun-synchronous RapidScat scatterometer (2014-2016) to demonstrate that the diurnal cycles in Ku-band radar backscatter were discernible over vegetated areas. Konings et al., 2017, and van Emmerik et al., 2017, related variations in the daily cycle of Ku-band backscatter to vegetation water stress in the humid tropical forests of Central Africa and the Amazon respectively. Other studies used aggregated data from scatterometers in sun-synchronous orbits to study diurnal variations in canopy water (Friesen et al., 2012; Froliking et al., 2011; Schroeder et al., 2016; Steele-Dunne et al., 2019). Froliking et al., 2011, found Ku-band backscatter over the Amazonia to be up to 1.0 dB lower at 6:00 compared to 18:00. This difference decreased when a major regional drought continued. Schroeder et al., 2016, and Friesen et al., 2012, observed diurnal differences in C-band backscatter in the United States (~10:00 and 22:30) and on a global scale (~9:30 and 21:30), respectively. In a study on North-American grasslands, Steele-Dunne et al., 2019, found mean differences between evening (21:30) and morning (9:30) observations of C-band backscatter between -0.6 and 0.6 dB, depending on region and season. The limitation of radar data from current satellites is that they are in sun-synchronous orbits, and data only available at fixed times (e.g. ASCAT at 10 am/10 pm). These times may not coincide with the ideal times to observe plant water variations, do not provide enough detail to capture and study daily cycles, and their data generally needs to be aggregated to draw meaningful conclusions. The future availability of spaceborne sub-daily SAR data therefore offers a unique possibility to study vegetation water dynamics at an unprecedented temporal resolution.

Ground-based radar experiments on sub-daily variations in backscatter have a longer heritage, and have shown that radar backscatter is sensitive to vegetation water changes during the day. Using a truck-mounted dual-pol radar spectrometer scanning densely

---

<sup>1</sup><https://www.capellaspace.com/>

<sup>2</sup><https://www.iceye.com/>



vegetated sorghum fields, Ulaby and Batlivala, 1976, combined 13 data acquisitions within ten days, where each acquisition was conducted at a different time of day. Aggregating these data, they found clear diurnal variations which they attributed to vegetation. Brisco et al., 1990, used a truck-mounted Ku-, C-, and L-band quad-pol scatterometer to study sub-daily fluctuations in backscatter measurements of a wheat canopy. They measured three full days, spread over two years. The results showed that, for C- and L-band, the diurnal backscatter variation correlated well with measured vegetation water content in the vegetative stage of the crop, while the correlation with soil moisture was higher when the plants were senescing. In addition, they showed that bulk vegetation water content (including surface and internal water content) and HH-polarized C-band backscatter with  $20^\circ$  incidence angle in the vegetative stage of wheat following a diurnal cycle with maxima just after sunrise and minima between solar noon and sundown. Using results from the same experiment, Gillespie et al., 1990, evaluated the effect of dew. The presence of dew was assessed by visual inspection, and backscatter patterns between two nights with and without dew were compared. They concluded that dew has an effect on C-band signals in particular, and that dew and internal canopy water effects can be differentiated according to timing and strength of response.

Other ground-based experiments focused on trees (Bouten et al., 1991; De Jong et al., 2002). Bouten et al., 1991, measured the vertical attenuation profile of a Douglas fir stand before and after rain events. The X-band microwave generator and receiver were mounted on two towers, 12.5 m apart, and the beam of the transmitter was pointed in the direction of the receiver. They found a clear increase in attenuation after canopy wetting. Moreover, they estimated canopy surface water storage from precipitation and through-fall measurements, and found high correlations with increments of the vertically integrated attenuation profiles. De Jong et al., 2002, analyzed the relation between vertically polarized X-band backscatter and rainfall interception for a single ash tree. Backscatter observations during 14 rain storms were averaged, and compared to dry situations. The results showed a logarithmic increase of backscatter with cumulative precipitation, supported by physical model simulations. In addition, several studies have observed a diurnal cycle in trunk dielectric constant, which has been related to tree water status and sap flow (McDonald et al., 1990; McDonald et al., 2002; McDonald et al., 1992; Salas et al., 1994; Weber and Ustin, 1991; Zimmermann et al., 1995).

These ground-based experiments successfully demonstrated that radar backscatter is sensitive to variations in total vegetation water content. However, the limited datasets leave many open questions in terms of the sensitivity of radar backscatter to surface versus internal water content, the influence of phenological stage and providing a quantitative link to water transport processes in the vegetation.

The aim of this chapter was to quantify fluctuations of internal and surface canopy water and their effect on sub-daily patterns of L-band backscatter with a view to demonstrating the potential value of sub-daily spaceborne radar backscatter for monitoring vegetation water dynamics. An intensive field campaign was conducted over an entire growing season of corn, combining temporally dense radar backscatter observations with continuous observations of leaf surface wetness, surface and root zone soil moisture, sap flow and meteorological variables, and frequent destructive vegetation sampling. These data were analyzed during the early-, mid- and late-season to study how

backscatter in each polarization is affected by variations of internal and surface water content, and how this sensitivity varies as the crop develops. Data from the fully grown canopy were also combined to obtain an average daily cycle, and insight into the influence of surface canopy water on the amplitude and timing of the daily cycle of backscatter.

## 3.2. MATERIALS AND METHODS

### 3.2.1. STUDY SITE

The experiments were conducted in the spring of 2018 at the Plant Science Research and Education Unit (PSREU) of the University of Florida and the Institute of Food and Agricultural Sciences (UF/IFAS) at Citra, Florida (29.410N, 82.179W). Sweet corn (*Zea mays L. var. rugosa*) was sown in rows on April 13 and harvested on June 18. The average plant density was 7.9 plants m<sup>-2</sup>. The soil at the field site consists of >90% sand (Bongiovanni et al., 2015; Bongiovanni et al., 2018), which allows for high infiltration rates. Early in the growing season, the corn field was irrigated several times with a center-pivot irrigation system. Irrigation was applied in the evening to minimize evaporative losses.

### 3.2.2. RADAR BACKSCATTER

Observations of radar backscatter were made with the University of Florida L-band Automated Radar System (UF-LARS), which was mounted to a Genie manlift, lifted to 14 m height, and set to scan the field with an incidence angle of 40°. This system operates at a center frequency of 1.25 GHz, and collects four polarization combinations (HH, VV, HV and VH) simultaneously. The backscatter coefficients ( $\sigma^0$ ) are computed using the Single Target Calibration Technique (STCT) (P-W. Liu, 2013; Sarabandi and Ulaby, 1990). Further specifications of this system, including accuracy and resolution, can be found in section 2.2.1.

For most of the season, 32 averaged  $\sigma^0$  observations were obtained per day. For the last eight days of the season, the number of acquisitions was reduced to 16 to avoid radio frequency interference with other microwave sensors in the field. HV and VH polarizations were averaged, and further shown as average cross-pol. Averaged cross-polarized backscatter is expressed as  $\sigma_{XP}^0$ . Sampling areas (section 3.2.4) and *in situ* sensors (section 3.2.3) were located outside the arc swept by the radar, to avoid disturbing the scene.

### 3.2.3. HYDROMETEOROLOGY

Meteorological data were obtained from the Florida Automated Weather Network (FAWN)<sup>3</sup>. The 18-meter tall FAWN weather station was located <600 m east from the experimental site. Observations of rainfall, air temperature on 2 m height, solar radiation, relative humidity and wind speed are available every 15 minutes. Reference evapotranspiration (ET<sub>o</sub>) was calculated from these data using an hourly version of the Penman-Monteith approach (Zotarelli et al., 2010).

Sap flow is the flux of water through the plant, as water extracted by the roots is transported to the leaves to replenish water lost through transpiration. In large trees, the time

<sup>3</sup><https://fawn.ifas.ufl.edu/data/>

lag between transpiration and sap flow measured at the base of a stem can be on the order of several hours, while the time lag between transpiration and sap flow at the crown is much smaller (Čermák et al., 2007; Meinzer et al., 2004; Phillips et al., 2008). For corn, we observed that the time lag between calculated reference evapotranspiration and sap flow on the stem was on the order of minutes. Therefore sap flow is a useful indicator of the timing and strength of the daily transpiration cycle which drives internal canopy water dynamics during the day.

Sap flow rates of four representative plants were measured with SGEX-19 Dynagage sap flow sensors (Dynamax Inc., Houston, TX, USA), which were installed close to other sensors, just outside the radar footprint. See Chapter 2, section , for details about the measurement principle of these sensors. The built-in sap flow calculator of the Dynagage Flow32-1K system was used to estimate the sap flow rate [ $\text{g h}^{-1}$ ] for each plant every 15 minutes. Sap flow [ $\text{mm 15min}^{-1}$ ] was calculated by averaging over the four sensors, converting the average weight of water to volume using the density of liquid water at  $25^\circ\text{C}$  ( $0.997 \text{ g cm}^{-3}$ ), and multiplying the results for an ‘average’ plant with the plant density. Because installation of a SGEX-19 sensor requires a stem diameter of at least 15 mm, the sensors were first installed on May 18.

Data gaps, e.g. due to battery failure or poor contact, were filled using a linear relationship between sap flow and the transpiration component of FAO crop evapotranspiration ( $K_{cb}ET_o$ ) (R. G. Allen et al., 1998). Here,  $ET_o$  is the reference evapotranspiration, i.e. the evapotranspiration from a hypothetical, well-watered grass reference surface, calculated using meteorological data from FAWN and the FAO Penman-Monteith method.  $K_{cb}$  is the basal crop coefficient for transpiration of a sweet corn canopy at potential rate. The multiplication with  $K_{cb}$  converts hypothetical evapotranspiration of a grass surface into transpiration of a sweet corn canopy, assuming no limitation of water (R. G. Allen et al., 1998). Linear regression between sap flow ( $F$ ) and  $K_{cb}ET_o$  was described by

$$F = 0.7222 \times K_{cb}ET_o - 0.001 \quad (3.1)$$

with  $R^2 = 0.871$ , based on  $n = 2389$  observations.

Leaf wetness due to dew and interception was monitored using three PHYTOS31 dielectric leaf wetness sensors (see section 3.2.3).

The sensors were attached to a wooden pole in between two rows in the early season. They were reattached to the corn plants once the stems were strong enough. The sensors were installed at different heights to capture the vertical distribution of water droplets in the canopy. The empirical model of Cobos, 2013, was used to estimate the mass of water ( $M_w$ ) deposited on the sensor surface [ $\text{g m}^{-2}$ ] from the sensor output (counts, see section 3.2.3):

$$M_w = 1.54 \times \exp(5.8 \times 10^{-3} \times \text{counts}) \quad (3.2)$$

Estimation of the mass of water on the canopy, Surface Canopy Water (SCW), was performed in two steps. First, regular measurements of leaf height, length and width were conducted, and leaf areas were estimated by assuming that corn leaves have an elliptical shape:

$$A_{leaf} = \pi \times l \times \frac{w}{4} \quad (3.3)$$

where  $A_{leaf}$  is the leaf area [ $\text{m}^{-2}$ ],  $l$  is leaf length [m] and  $w$  is leaf width [m]. Second, it was assumed that the wetness of a leaf at any height could be approximated as that of the nearest sensor.

$$SCW = \rho_{plant} \times \sum_{i=1}^n A_{leafi} \times M_{wi} \quad (3.4)$$

where SCW is surface canopy water per square meter of ground [ $\text{kg m}^{-2}$ ],  $\rho_{plant}$  is the average number of plants per  $\text{m}^{-2}$ ,  $M_{wi}$  is the water mass on the sensor closest to leaf  $i$  [ $\text{kg m}^{-2}$ ], and  $n$  is the number of leaves per plant.

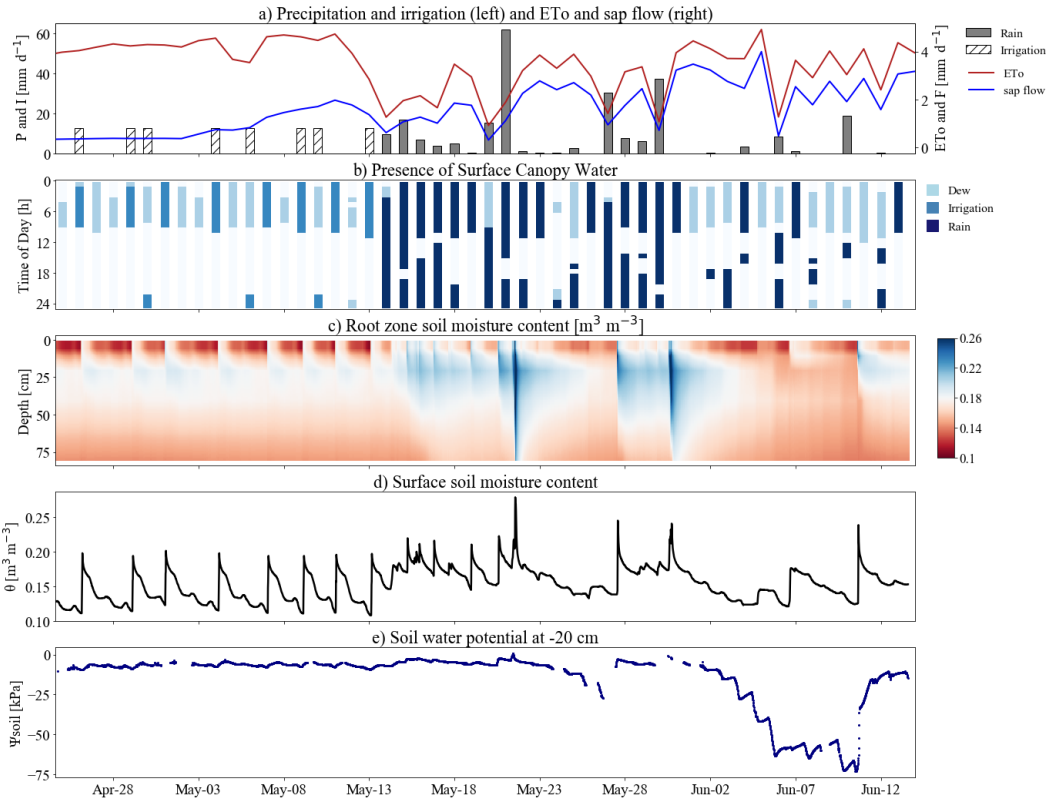


Figure 3.1: Time series of (a) rainfall, irrigation and reference evapotranspiration (ETo), (b) presence of surface canopy water resulted from dew, irrigation or rain, (c) volumetric root zone soil moisture content, (d) surface soil moisture content only, (e) soil water potential at 20 cm depth.

Root zone soil moisture was measured with ten Decagon EC-5 sensors (see Chapter 2), which were installed in two pits at five different depths: 5, 10, 20, 40 and 80 cm. The pits were located 40 meters apart, but centered between the same two rows. Site-specific calibration was performed yielding a linear regression  $R^2$  of 0.993. Soil moisture was similar in both pits. Hence, the presented results are the averages over the two pits.

Linear interpolation between the measurements was applied to visualize root zone soil moisture.

Soil water potential was monitored using two T4e pressure transducer tensiometers (UMS GmbH, 2011). These were installed 40 meters apart, close to the soil moisture pits. The centers of the ceramic cups were located at a depth of 20 cm. The presented results are the averaged signals of both tensiometers.

### 3.2.4. VEGETATION SAMPLING AND MONITORING

Vegetation water content (VWC) and dry biomass ( $m_d$ ) were measured using destructive sampling (see Chapter 2, section 2.2.3). Field-representative VWC [ $\text{kg m}^{-2}$ ] was derived from equation 5.1:

$$VWC = (m_f - m_d)\rho_{plant} \quad (3.5)$$

where  $m_f$  is the average fresh weight or fresh biomass of the eight samples [kg],  $m_d$  is the average dry weight or dry biomass of the eight samples [kg], and  $\rho_{plant}$  is the number of plants per square meter of ground. Gravimetric water content,  $M_g$ , is the mass of water per unit mass of fresh biomass (equation 5.2):

$$M_g = \frac{m_f - m_d}{m_f} \quad (3.6)$$

Equations 5.1 and 5.2 were applied for each of the plant constituents (i.e. leaves, stems, tillers, ears) separately.

Sampling was conducted before sunrise (6am) to minimize the effect of transpiration on the measurements that represent seasonal variability of VWC and  $M_g$ . These predawn measurements were scheduled three times per week. On one of these three days, one extra sampling was performed during the day in order to capture diurnal variations. This second sampling was at 6pm, which would be the time of the corresponding evening pass for a sun-synchronous satellite such as SMAP (Entekhabi et al., 2010).

Plant growth stages were visually identified three times per week, using the *Biologische Bundesanstalt, Bundessortenamt and Chemical industry* (BBCH) scale for corn (Meier et al., 2009). The cut samples were used to measure plant heights. Leaf area index (LAI) was calculated by multiplying the averaged, estimated leaf areas by plant density.

## 3.3. RESULTS

### 3.3.1. HYDROMETEOROLOGY

Fig. 3.1 shows the hydrometeorological and soil moisture conditions during the growing season. The first three weeks of the season were characterized by high levels of reference evapotranspiration (ET<sub>o</sub>) and an absence of precipitation (Fig. 3.1a). On several days, midnight irrigation was applied to control soil moisture content (Fig 3.1a-d), leading to a soil water potential which is favorable for root water extraction as soon as the roots reach deep enough (Fig 3.1e). These conditions allowed for high rates of transpiration. Water films on leaf surfaces were detected every morning (Fig 3.1b) as a result of dew formation, interception of sprinkler irrigation or a combination of both, and disappeared at around 10:00 every morning.

The mid-season weather conditions featured frequent, tropical rainfall and thunderstorms (Fig. 3.1a). This resulted in water droplets on the canopy for long periods during the day (Fig. 3.1b), and several sharp increases in root zone soil moisture content (Fig. 3.1c). Limited rain between May 22 and May 27 led to a temporary reduction in root zone soil moisture content and potential (Fig. 3.1d-e).

A dry period with high temperatures and solar radiation, started on June 1. This produced high evaporative demand (ET<sub>o</sub> in Fig. 3.1a), which resulted in a rapid decrease of soil moisture in the root zone. Despite the limited root zone soil moisture, leaf surfaces were wet every morning, mainly because of dew formation (Fig. 3.1b). A substantial rain event on June 10 ended the dry period.

### 3.3.2. VEGETATION DEVELOPMENT AND WATER CONTENT

The sweet corn crop development is illustrated in Fig. 3.2. Corresponding explanations of the BBCH phenology codes can be seen in Table 3.1. Fig. 3.2(a) shows the plant height and dry biomass accumulation [kg m<sup>-2</sup>] of the total plant and individual plant constituents during the life cycle, based on destructive vegetation sampling data. Fig. 2 (b) and (c) show how the water content of the plant and its constituents vary during the growing cycle. Fig. 3.2(b) shows the mass of water stored in [kg m<sup>-2</sup>], a measure commonly used in microwave remote sensing. Fig. 3.2(c) shows this water storage in terms of gravimetric moisture content, which is the mass of water per total mass of the plant. This is more closely related to the relative water content used by plant physiologists.

First plant emergence was observed on April 19, six days after sowing. Although leaf and stem dry biomass ( $m_d$ ) increased at similar rates until plants reached half their final height (Fig. 3.2a), stems held substantially more water (Fig. 3.2b-c). At the end of the vegetative stage, 65% of all VWC was stored in the stems.

In the reproductive stage, ear formation coincided with VWC decreases in all other constituents, especially in the stems. From May 30 to June 6, water storage in the stems decreased by almost 30%: -0.8 kg m<sup>-2</sup>, as the ears formed and separated from the main stem (Fig. 3.2b). Leaf senescence of the lowest leaves occurred from June 2 onward. The reproductive stage largely coincided with the dry period shown in Fig. 3.1. The corn was harvested five days after the last sampling.

The results of the seven days of twice-daily destructive vegetation sampling are shown in Fig. 3.3. The figure shows the internal canopy water differences between 6:00 and 18:00 for the total plant and the most important constituents (by biomass). The smallest  $\Delta M_g$  was observed on May 16, when cloud and rain limited transpiration. Significant decreases in internal water content were observed in the early season, as a result of high atmospheric demand for evapotranspiration (Fig. 3.1(a)), a shallow root zone, and a relatively dry upper soil (Fig. 3.1(c)). These differences in  $M_g$  translate to small  $\Delta$ VWC (Fig. 3.3b) due to the limited fresh biomass in the early vegetative stages. In the reproductive stage, diurnal moisture losses in stems increased, while such losses decreased for ears. At this stage, ears grow and store water, while the internal water content of the stems starts to decrease. These sub-daily variations were substantial compared to the seasonal predawn  $M_g$  variations (Fig. 3.2c). It should be noted that maximum sub-daily moisture variations may be higher than the difference between 6:00 and 18:00.

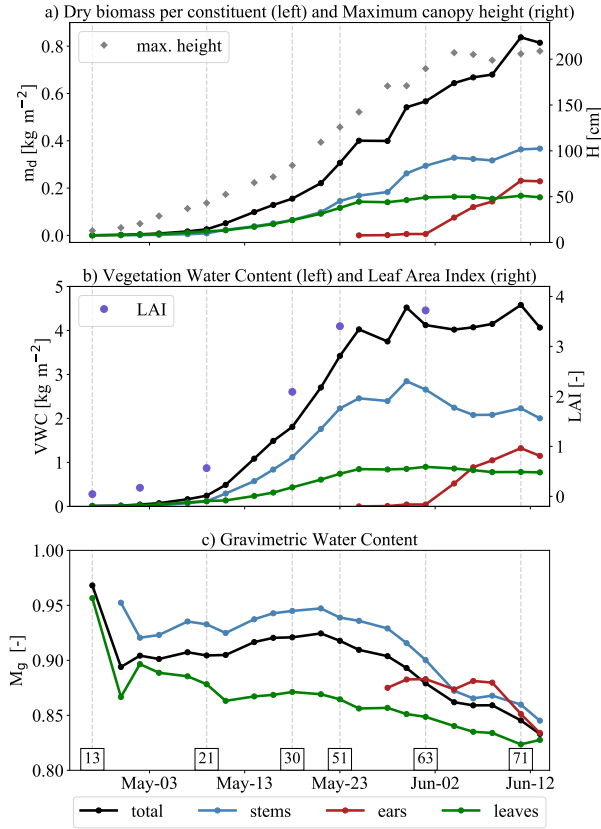


Figure 3.2: Seasonal patterns of (a) dry biomass and maximum canopy height, (b) predawn vegetation water content and leaf area index, and (c) predawn gravimetric water content, including the contributions of dominant plant constituents to total. Important phenological stages are represented by BBCH codes, which are explained in Table 3.1.

### 3.3.3. BACKSCATTER

#### SEASONAL VARIATIONS IN BACKSCATTER

Backscatter coefficients (VV, HH, average cross-pol) are shown in Fig. 4.9. Backscatter increased in all polarizations with the growth of the crop. Co-polarized backscatter increased from  $< -14$  dB after planting to about  $-5$  dB when plants reached half of their total biomass, while cross-polarized backscatter increased from  $< -32$  dB to about  $-16$  dB.

The influence of early season irrigation events (Fig. 3.1) is apparent in all polarizations (Fig. 4.9). Sensitivity to wetting events (irrigation and rainfall) decreased as the canopy grew and  $\sigma^0$  became increasingly sensitive to wet biomass (Appendix).

The increasing trend in  $\sigma^0$  due to vegetation growth tapers off around May 20. These high values, 3-4 days prior to plant VWC and LAI maxima can be explained by the heavy rainstorms around May 20. Precipitation from these storms increased both canopy surface wetness and soil moisture, which produced high  $\sigma^0$  values in all polarizations. Nonethe-



Table 3.1: Crop development stages

| BBCH | Stage of development                                            | Dates  |
|------|-----------------------------------------------------------------|--------|
| 13   | Leaf development – 3 leaves (V)                                 | Apr 25 |
| 21   | Start of tiller formation (V)                                   | May 7  |
| 30   | Start of stem elongation (V)                                    | May 18 |
| 51   | Start of tassel emergence (V)                                   | May 23 |
| 63   | Male: start pollen shedding.<br>Female: stigma tips visible (R) | Jun 1  |
| 71   | Start of grain development:<br>kernels at blister stage (R)     | Jun 11 |

V=vegetative stage. R= reproductive stage.

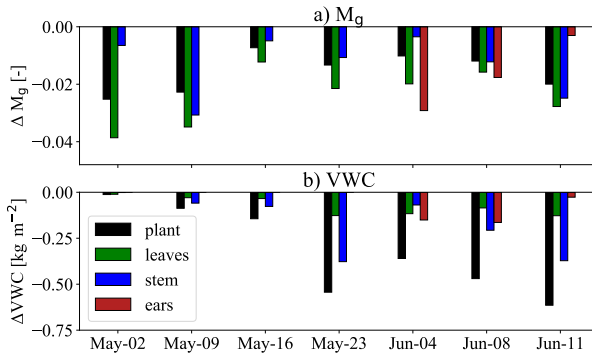


Figure 3.3: Change (6:00 minus 18:00) in internal canopy water content of total plant and dominant constituents, represented as (a) gravimetric moisture loss and (b) equivalent weight of moisture loss [ $\text{kg m}^{-2}$ ].

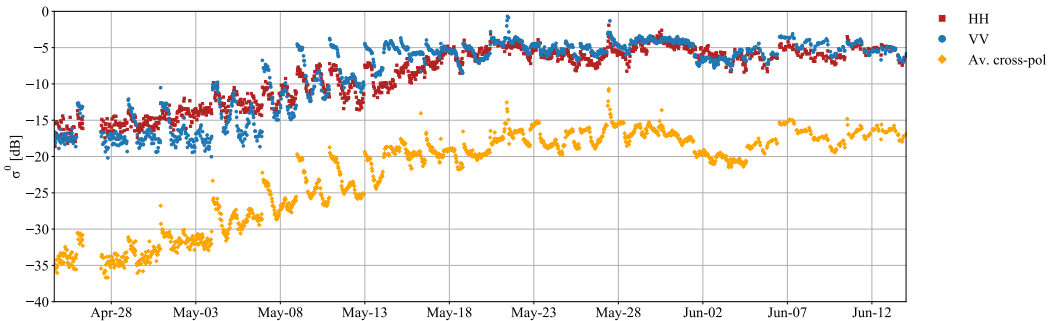


Figure 3.4: Time series of observed L-band co- and cross-polarized backscatter.

less, responses to some events after this date were observed. The decrease in  $\sigma^0$  from

June 1 corresponds with the drop in soil moisture (Fig. 3.1) and the sharp reduction in stem water content (Fig. 3.2b). Backscatter increased again following small rain events and the formation and separation of ears.

#### EARLY SEASON

Two three-day periods in the early season are highlighted in Fig. 3.5. Fig. 3.5 (a-c) shows a period 11-13 days after emergence when bare soil exposure was still considerable and plant height was just 15-20 cm. Fig. 3.5 (a) shows co- and cross-polarized backscatter. Fig. 3.5 (b) shows raw data counts from two leaf wetness sensors positioned 7cm above the ground, as well as the sap flow. Fig. 3.5 (c) shows the precipitation at the nearby weather station and the soil moisture observed at 5cm depth. The irrigation event on April 30 lead to an increase in soil moisture at 5cm depth, and a sharp increase in  $\sigma^0$  of up to 5dB. Clear cyclic variations of 2-3 dB are observed in  $\sigma^0$ , particularly in  $\sigma_{VV}^0$ . These cannot be explained by the 5cm soil moisture, but seem to follow the accumulation and dissipation of dew on the vegetation and soil surface as indicated by leaf wetness sensor (LWS) data in Fig. 3.5 (b). The LWS counts increase during the night as dew accumulates on the sensor. The LWS counts decrease rapidly after sunrise as the increase in solar radiation allows the dew to evaporate. On each of the days shown in Fig. 5, and also in Fig. 3.1 (b), the dew has generally dissipated by 10:00 am. It is important to note that, in addition to forming on the leaves and the LWS, dew also forms as a film of water on the soil surface. It is clear from Fig. 3.5 (c) that it is insufficient to infiltrate the soil and reach the sensor at 5cm. However, L-band backscatter is dominated by surface scattering from the soil at this stage (Joerg, 2018; McNairn et al., 2009; Monsivais-Huertero et al., 2018; Stamenković et al., 2015, and Fig. 3.10), and the difference between a wet (e.g.  $0.3 \text{ cm}^3 \text{ cm}^{-3}$ ) and dry (e.g.  $0.1 \text{ cm}^3 \text{ cm}^{-3}$ ) soil can produce differences of up to 3.5 (HH) and 6 (VV) dB (Dubois et al., 1995). We postulate, therefore, that the accumulation and dissipation of this film of water on the soil surface is the most important reason behind the cyclic  $\sigma^0$  variations in Fig. 3.5 (a). The effect of dew on the topsoil is also clear in VV where the irrigation event on April 30 increases  $\sigma_{VV}^0$  from -18 dB to -13 dB, a value at which it stays due to the presence of dew until sunrise the following morning. Moreover,  $\sigma_{VV}^0$  ramps up as dew accumulates in the early hours of May 2, before decreasing again at sunrise.

Fig. 3.5 (d-f) shows the measurements of one week later when the maximum plant height has increased to 37 cm (May 7) and 43 cm (May 9), LAI is around 0.57 and VWC is increasing from  $0.16 \text{ kg m}^{-2}$  (May 7) to  $0.23 \text{ kg m}^{-2}$  (May 9). While soil moisture values are comparable to those observed the week before, the  $\sigma^0$  values in Fig. 3.5 (d) are around 4 dB higher than those in Fig. 3.5 (a) in all polarizations. From Fig. 3.10, this can be attributed to the increase in vegetation scattering in all polarizations, an increase in double-bounce in VV, and an increase in vegetation ground scattering in HH and cross-pol. In other words, the backscatter is increasing due to plant growth, and microwave interactions with the vegetation are becoming increasingly important. Sap flow values are higher than in Fig. 3.5 (b) due to increase in plant area and transpiration. The LWS have been repositioned at 10cm and 20cm to accommodate the growing plant, and a sensor was added at 30cm on May 7.

Irrigation events on May 6 and 9 lead to sharp increases in soil moisture and  $\sigma^0$ . Increases of 8 dB (VV), 4 dB (HH) and 5-6 dB (cross-pol) were observed in response to

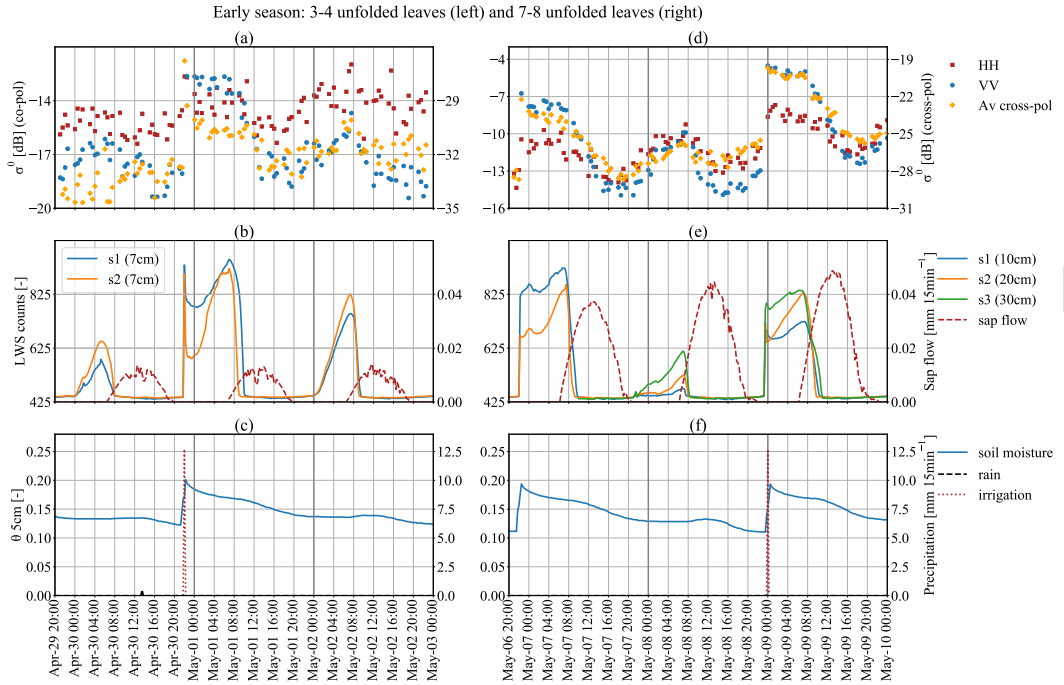


Figure 3.5: Early season patterns of co- and cross-polarization backscatter (upper row), raw data counts from the leaf wetness sensors and sap flow (middle row), and surface soil moisture and precipitation (lower row). The left figures show a 3-day period when plants reach 15-20 cm, while the right figures show a 3-day period when plants reach 43-65 cm. Note that the vertical axes of the left and right backscatter plots are different.

the event on May 9. On the May 7 and 9, initial rapid increases in LWS counts due to interception of irrigation were followed by more gradual increases as dew accumulated during the night. Steady dew accumulation is also observed during the night of May 7-8. On all three days, the accumulated moisture dissipated quickly after sunrise. The cyclic variations in  $\sigma^0$  are clearer than they were in Fig. 3.5, and their correspondence with the LWS data is even more striking. The  $\sigma^0_{VV}$  is particularly responsive to the presence of water on the soil and vegetation. This may be due to the important role of double-bounce in  $\sigma^0_{VV}$  at this time.

MID-SEASON

Fig. 3.6 shows two periods in the mid-season. Note that average  $\sigma^0$  increased significantly since early season, as a result of plant growth. In the time period shown in Fig. 3.6 (a-c), the corn had started to tassel, and leaves had almost reached final sizes (Fig. 3.2).

Fig. 3.10 shows that, for this growth stage,  $\sigma^0$  is dominated by vegetation scattering. There are limited contributions from double-bounce in VV and HH, and the vegetation-ground term in HH. This is consistent with earlier research (Joerg, 2018; McNairn et al., 2009; Monsivais-Huertero et al., 2018; Stamenković et al., 2015).

Low intensity rain events on May 23, 24 and 25 were intercepted by the almost fully

Mid-season: tassle emergence (left) and start of reproductive stage (right)

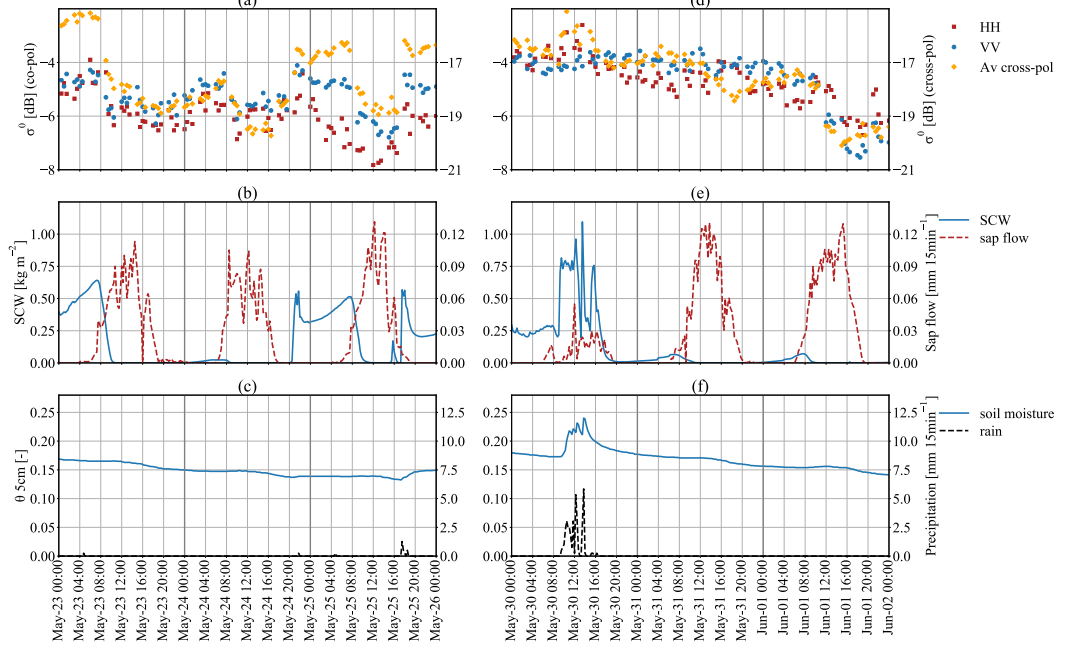


Figure 3.6: Mid-season patterns of co- and cross-polarization backscatter (upper row), surface canopy water and sap flow (middle row), and surface soil moisture and precipitation (lower row). The left column shows a 3-day period when plants reach 125–140 cm, while the right column shows a 3-day period when plants reach 180–189 cm. Note that the vertical axes of backscatter and surface canopy water are different from Fig. 3.5.

grown leaves and had a negligible impact on soil moisture. This suggests that  $\sigma^0$  variations in Fig. 3.6a can be attributed to variations in SCW and internal VWC (Fig. 3.6a-b). Cross-pol backscatter, which is sensitive to leaf moisture content, increased rapidly in response to interception in the evenings of May 24 and May 25. The presence of dew in the early hours of May 23 and 25, and interception on May 24 and 25 resulted in elevated values of  $\sigma_{XP}^0$ . Rapid dissipation of dew in the early morning on May 23 and 25 produced a  $\sim 2$ dB drop in  $\sigma_{XP}^0$ . The difference in response of the three polarizations to SCW is particularly noticeable during the interception and dew events early on May 25, and could be explained by their relative sensitivities to different canopy constituents. Note that estimated interception sometimes exceeds measured rainfall. This could be due to (1) the simplistic model used to convert sensor output to full canopy interception (see section 3.2.3), (2) spatial rainfall variability (rainfall was collected 600 meters from studied field), (3) accuracy of rainfall data ( $\sim 0.25$  mm) or (4) spatial heterogeneity of interception itself due to e.g. variations in plant architecture.

Backscatter in all polarizations reflects variations in internal water content. Recall from Fig. 3.3 that internal water losses were high in this period ( $\sim 0.5$  kg m<sup>-2</sup>) because of a relatively high atmospheric water demand (Fig. 3.1). The rise in sap flow and transpiration resulted in a decrease in  $\sigma^0$ , and water uptake in the evening resulted in an

increase.

Fig. 3.6(d-f) illustrates the observations of one week later, after a four-day period of heavy rainfall (Fig. 3.1). The last rain event on May 30 was followed by two dry and hot days, resulting in a decrease in surface soil moisture. The limited variation in  $\sigma_{VV}^0$  and  $\sigma_{HH}^0$  in response to the sharp increases in SCW and soil moisture suggests that co-pol backscatter saturated at  $\sim -4$  dB. Despite high rates of sap flow on May 31, diurnal cycles of  $\sigma_{VV}^0$  and  $\sigma_{HH}^0$  were not observed. This saturation was probably caused by a combination of a wet field (Fig. 3.1) and a peak in VWC (Fig. 3.2). May 31 was characterized by high evapotranspiration rates, causing canopy surface water to disappear, and soil moisture to decrease. Meanwhile, stem water content started to drop significantly (Fig. 3.2). These losses of water led to a decrease in co-pol backscatter, which resulted in observed diurnal cycles of  $\sigma^0$  again (Fig. 3.6d). Dips in cross-polarized backscatter (May 31) and all polarizations (June 1) coincide with the dissipation of dew and peaks of sap flow.

### LATE SEASON

Fig. 3.7 shows observations from two periods in the late season during which the corn plants experienced the lowest root zone water availability of the season (Fig. 3.1(c and e)). Recall from Fig. 3.3 that diurnal water fluctuations in response to transpiration during these days were considerable. Nonetheless, the plants were able to recover from water losses after solar noon; predawn  $M_g$  did not decrease with higher rates than in the wet period before (Fig. 3.2). Simulations in Fig. 3.10 suggest that  $\sigma_{XP}^0$  and  $\sigma_{VV}^0$  were dominated by vegetation scattering, while  $\sigma_{HH}^0$  still had limited sensitivity to ground-related terms.

The diurnal VWC cycles were discernible in  $\sigma^0$  in all polarizations, particularly on the days without rainfall. On June 5, there is a noteworthy decrease of almost 4dB in all polarizations. This coincides with a significant loss of internal water content (Fig. 3.3) due to transpiration (sap flow in Fig. 3.7 (b)). The minimal change in soil moisture at this time, and the fact that the decrease is consistent across polarizations suggests that this is a decrease in vegetation scattering due to the observed drop in internal water content. From midnight on June 9 to noon on June 10, soil moisture barely changes. Backscatter on the other hand, especially VV and cross-pol, increases with dew accumulation during the night and decreases as dew dissipates and transpiration leads to internal water content losses during the day. A similar response is observed in the response to dew and transpiration in the early hours of June 11. Again, the minimal variation in soil moisture and the consistency across polarizations suggest that this is a response to internal and surface canopy water dynamics rather than sensitivity to soil moisture.

Precipitation events on June 4, 6 and 10 (Fig. 3.7 (c) and (f)) resulted in spikes in interception (SCW in Fig. 3.7(b) and (e)). The precipitation event of June 10 led to a substantial and prolonged increase of soil moisture. The limited effect this prolonged increase had on backscatter (particularly  $\sigma_{VV}^0$  and  $\sigma_{XP}^0$ ) confirms the strong reduction to soil moisture sensitivity at this stage. Given the lack of sensitivity to surface soil moisture in VV and cross-pol, it is likely that these backscatter increases are primarily in response to interception rather than moisture on the soil surface.

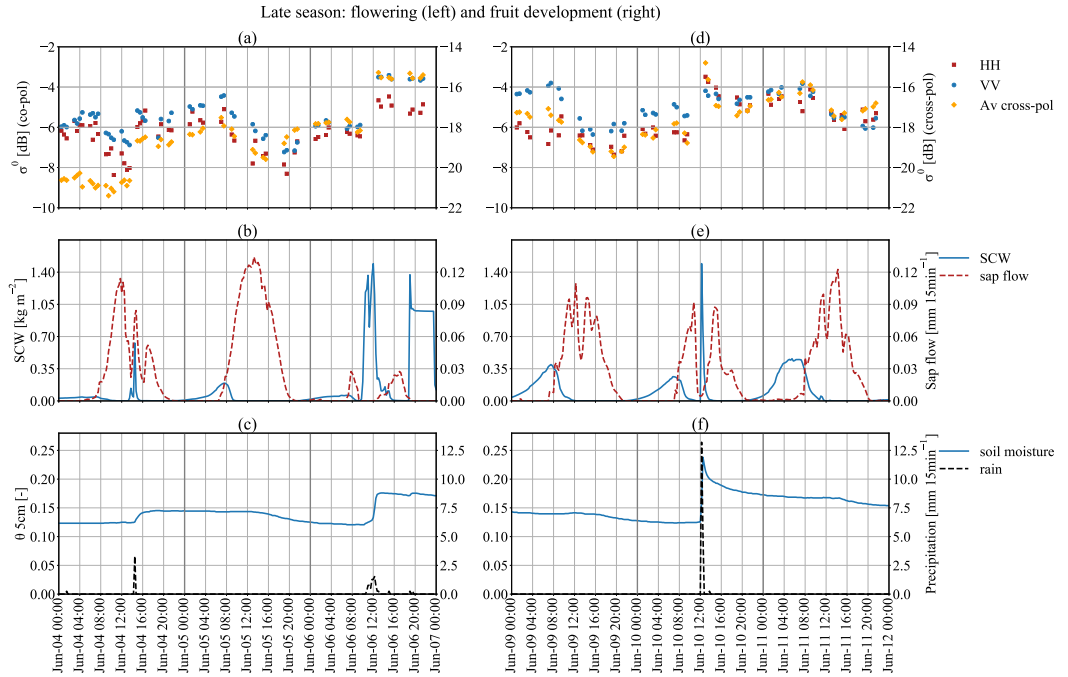


Figure 3.7: Late season patterns of co- and cross-polarization backscatter (upper row), surface canopy water and sap flow (middle row), and surface soil moisture and precipitation (lower row). Maximum canopy height was stabilized at 205 cm during this period. Note that the temporal density of backscatter is less than in previous figures.

### MEAN DAILY CYCLES

Fig. 3.5-3.7 show that sub-daily variations in  $\sigma^0$  included rapid variations due to the interception of intermittent precipitation events, and slower variations due to dew formation and dissipation and internal water content variations. To minimize the influence of random individual precipitation events and gain some insight into the average daily cycle, data were averaged over a 21-day period between May 23 and the last day of the experiment, June 13. This is the period in which  $\sigma^0$  did not increase anymore as a result of crop growth (Fig. 4.9). Previous studies and model simulations suggest that the effect of soil moisture on  $\sigma^0$  in all polarizations is limited in this period (Fig. 3.10, McNairn et al., 2009; Monsivais-Huertero et al., 2018; Stamenković et al., 2015).

Fig. 3.8 shows the mean diurnal cycle of  $\sigma^0$ , SCW and sap flow, soil moisture and precipitation over this period. Clear daily cycles can be observed in  $\sigma^0$ , sap flow and SCW. Peaks of VV and cross-pol coincide with the peak in SCW, and the start of the sap flow/transpiration cycle. After sunrise, the increase in net radiation drove transpiration and led to dissipation of dew from the canopy. Backscatter dropped on average with 0.7 dB (VV), 0.6 dB (HH), and 1.0 dB (cross-pol) between sunrise and 15:00. After 15:00, there is a downward trend in sap flow and an upward trend in  $\sigma^0$ . Most rainfall events occurred during daytime and they explain the fluctuations in averaged SCW during the afternoon.

The peak values in rainfall at 09:45 and 12:15 were due to two major convective rainfall events, each of which resulted in a significant increase in average soil moisture but only a modest and transient effect on average SCW and  $\sigma^0$ .

To exclude the effect of rainfall completely, the four days without any rainfall within this period were plotted separately in Fig. 3.9. Note that there was a decreasing trend in  $\sigma^0$  during this period due to the loss of internal water content of the stems in this growth stage, and the limited root zone soil moisture availability between June 5 and 9. Also note that sap flow was high in this period, so high sub-daily variations of internal water content are expected. Temporal patterns were similar to those in Fig. 3.8, although the timing of the  $\sigma^0$  minima are slightly different. Cross-polarized backscatter changed inflection again after the peak hours of evapotranspiration, while VV-polarized backscatter changed inflection with the start of dew formation. In both Fig. 3.8 and Fig. 3.9, nocturnal increase is only observed in  $\sigma_{VV}^0$  and  $\sigma_{XP}^0$ . In the absence of precipitation, the average diurnal difference in  $\sigma^0$  on these four days was 2.4 dB (VV), 1.6 dB (HH) and 2.0 dB (cross-pol).

### 3.4. DISCUSSION

Consistent with previous studies (e.g. Paloscia et al., 1999), L-band sensitivity to scattering from vegetation correlated with the buildup of VWC during the season (Fig. 3.2). With low vegetation, early season  $\sigma^0$  patterns in all polarizations were consistent with soil moisture responses to wetting events (irrigation, precipitation), and even showed strong similarities with dew deposition on the topsoil (Fig. 3.5). Similar wetting events, with similar soil moisture responses, showed a much smaller effect on  $\sigma^0$  in all polarizations in mid and late season (Fig. 4.9 and Fig. 3.7). In mid and late season, and particularly beyond May 18, differences between  $\sigma_{VV}^0$  and  $\sigma_{HH}^0$  were minimal. This can only be explained by the predominance of volume scattering, i.e. direct vegetation scattering, since stem attenuation and scattering, as well as double bounce are polarization dependent Liao et al., 2016. This predominance of vegetation scattering is confirmed by the physical model simulations in the Appendix and Fig. 3.10. Although it is not a persistent contribution, double bounce can still cause some sensitivity to soil moisture at HH polarization until the end of the season. The seasonal increased sensitivity to vegetation and reduced sensitivity to soil confirms previous work on L-band (e.g. Joseph et al., 2008; Monsivais-Huertero et al., 2018; Paloscia et al., 1999).

Sub-daily backscatter variability has been attributed to variations in VWC in several studies (e.g. Konings et al., 2017; Steele-Dunne et al., 2012; van Emmerik et al., 2017). However, these satellite-based studies lacked ground validation data. The unprecedented destructive sampling data presented in this study confirm that sub-daily variations in VWC are substantial ( $>0.5 \text{ kg m}^{-2}$ , Fig. 3.3) even though corn is an isohydric species (i.e. water content is regulated through active stomatal control). This motivates further research to include other species.

The deepest drops in  $\sigma^0$  were observed after the acquisition at 9:30, when dew almost dissipated completely (Fig. 3.9). This is also observed on dry days in Fig. 3.6 and Fig. 3.7. Since transpiration rates become substantial after this time, this suggests that diurnal VWC fluctuations govern the most substantial part of the sub-daily  $\sigma^0$  cycles in mid- and late season.

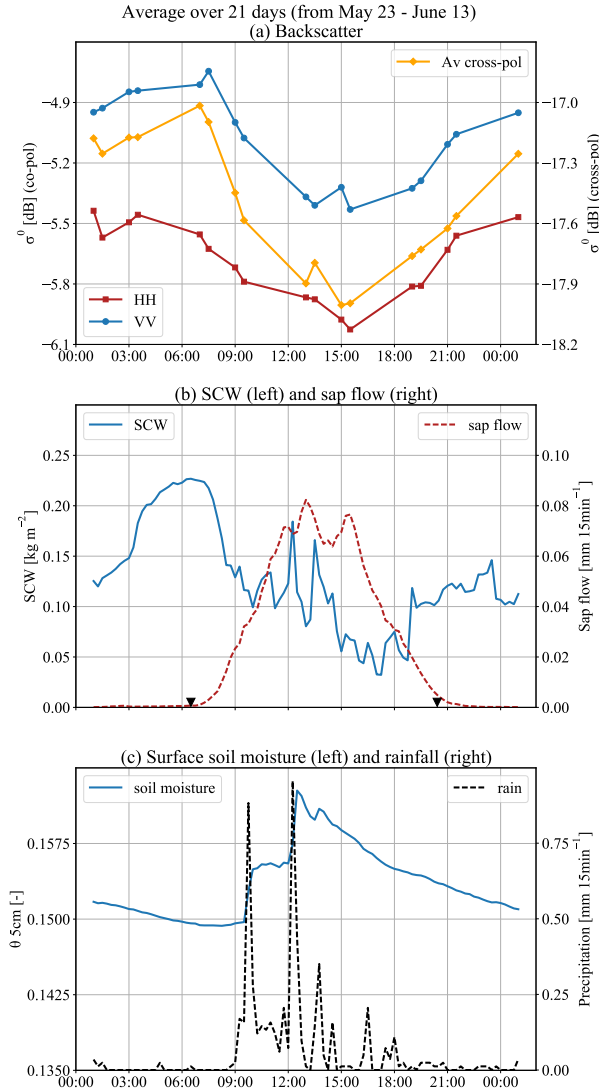


Figure 3.8: Mean daily cycles of (a) co- and cross-polarized backscatter, (b) surface canopy water and transpiration, and (c) soil moisture and rainfall, for the last 21-days of the season. Timing of sunrise and sunset are depicted with triangles in (b).

Several studies have attributed differences in diurnal backscatter to the presence of dew, but did not account for variations in internal VWC (e.g. Herold et al., 2001; Hornbuckle et al., 2010; Wood et al., 2002). The combination of intensive destructive vegetation sampling, continuous leaf wetness monitoring and high-revisit backscatter provides unique insight into their combined influence on the dynamics of sub-daily backscatter and how that varies throughout the season. Gillespie et al., 1990 provide one of the few



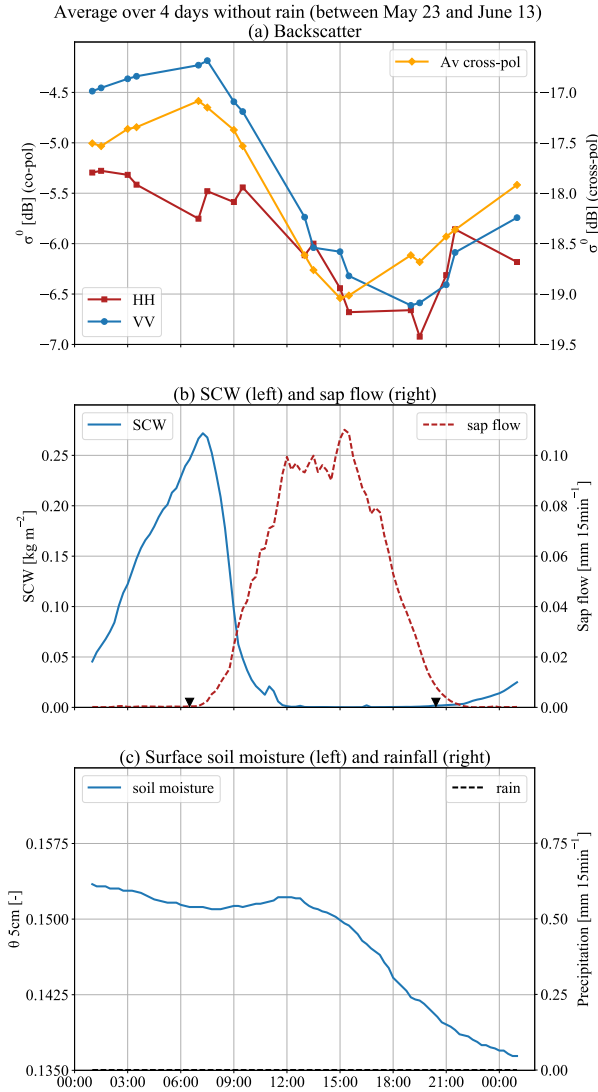


Figure 3.9: Mean daily cycles of (a) co- and cross-polarized backscatter, (b) surface canopy water and transpiration, and (c) soil moisture and rainfall, for only the 4 dry days within the last 21-days of the season. Timing of sunrise and sunset are depicted with triangles in (b).

studies in which both internal and surface water are considered in the context of dew detection. They found that the C-band HH-pol backscatter on a night without dew had a peak 1.5 hours after sunrise, corresponding to the peak in their observations of internal VWC Gillespie et al., 1990. On the other hand, the backscatter peak on a night with dew was at sunrise, which is the moment beyond dew starts to disappear. Similarly, our L-band observations show a sub-daily backscatter maximum around sunrise,

particularly in VV and cross-pol (Fig. 3.8 and Fig. 3.9). This is consistent with the peaks of dew accumulation and suggests that dew can have a significant effect on the timing and magnitude of the maximum of the sub-daily backscatter cycle. While Gillespie et al., 1990 provided the first indication that dew formation and dissipation determines the peak of (C-band, HH-pol) backscatter, the dataset was limited to two nights and the use of visual inspection to confirm the presence of dew. Our inclusion of continuous leaf wetness sensors allowed us to capture the accumulation, peak and dissipation of dew every night for the entire growing season, ensuring that our conclusions are based on a diverse range of events.

The inclusion of continuous leaf wetness measurements also provides unique, new insight into L-band backscatter sensitivity to rainfall interception. Light rain events, intercepted by the vegetation, caused strong fluctuations in  $\sigma^0$  (3dB in cross-pol and 2dB in co-pol), even though soil moisture was constant (see Fig. 3.6a-c). The presence of surface canopy water is not considered in current electromagnetic models (e.g. Bracaglia et al., 1995; Monsivais-Huertero et al., 2018; Ulaby et al., 1990) or retrieval algorithms (e.g. Dubois et al., 1995; Hosseini et al., 2015; Joseph et al., 2008). The results presented here demonstrate that SCW can have a significant effect on  $\sigma^0$ . Accounting for SCW in models and retrieval algorithms can therefore be expected to lead to improved retrievals of soil and vegetation variables.

The significant effect of both dew and interception on  $\sigma^0$  illustrates the value of including continuous leaf wetness sensors in microwave field campaigns and experiments. In this study, SCW was estimated from leaf Wetness Sensor data using a simple weighting based on LAI. While this was sufficient to demonstrate the important influence that SCW has on the canopy, rigorous validation of SCW is essential in future experiments that seek to establish quantitative relationships between SCW and  $\sigma^0$ . Given that microwaves penetrate the vegetation, future research should also examine how the vertical distribution of surface canopy water influences its effect on  $\sigma^0$ .

### 3.5. CONCLUSIONS

Results from an intensive experimental campaign combining sub-daily radar and vegetation water dynamics observations were used to explore the sensitivity of L-band radar backscatter to variations in surface and internal canopy water content of corn. The daily cycle in radar backscatter was found to vary in amplitude depending on the growth stage of the vegetation. Though the strongest diurnal variations were observed during the early vegetative stages, the limited vegetation scattering and attenuation during this time suggests that these variations are attributed to surface soil moisture fluctuations and heavy dew on the uppermost skin of the soil. As the canopy approached full biomass, the sensitivity to the underlying soil was strongly reduced, and the diurnal cycle in radar backscatter was found to reflect temporal patterns in surface and internal water content.

Radar backscatter, especially in cross-pol, was found to be sensitive to surface canopy water, with temporal variations in radar backscatter closely following the slow accumulation and rapid dissipation of dew, and exhibiting transient but significant increases in response to interception. In addition to being a variable of interest in its own right, the

prevalence of dew during the night and early morning and its influence on the radar backscatter highlights the potential influence of overpass time on the interpretation of radar observations from sun-synchronous satellites for vegetation monitoring. It also highlights the potential benefit of being able to choose sub-daily SAR data at specific overpass times to avoid the confounding influence of dew on the retrieval of biomass and internal water content. Both the effects of surface and internal canopy water on backscatter underscore the importance of including canopy water dynamics in physical models, particularly those used to simulate sub-daily radar observations.

One of the key challenges of exploiting sub-daily spaceborne SAR will be to disentangle surface and internal water content. Continuous monitoring of surface canopy water significantly improved the interpretation of sub-daily radar. During daytime, interception events are often transient and easily identifiable, and dew dissipation is often rapid. However, the slower dynamics of dew accumulation and internal water content variations are more difficult to separate. Developing a reliable approach to monitor VWC continuously would ease this separation of signals, and would improve the interpretation of sub-daily radar significantly. The sensitivity to surface and internal water content variations was found to be polarization dependent. This suggests that sub-daily polarimetric SAR (PolSAR) could be particularly useful to disentangle surface from internal canopy water variations.

The results demonstrate a potentially valuable application for sub-daily spaceborne SAR missions. However, the dataset is limited to a single crop type and a single radar configuration. There are many open questions to be addressed. Planned and candidate missions have been proposed that could yield data at different frequencies. Additional experimental research is essential to explore the sensitivity of backscatter from L-, to Ku-band to canopy water dynamics given the influence that frequency will have on both the penetration depth in the canopy and the sensitivity to the various vegetation constituents. The influence of viewing geometry also warrants investigation. The incidence angle of radar backscatter observations from geostationary satellites varies by latitude. Hence, the suitability of sub-daily SAR data may be limited to certain latitudinal bands. For constellations, a time series of data for a given location on the ground will combine acquisitions that may vary by incidence and azimuth angle. Both influence backscatter, particularly in agricultural areas, so their impact on the relative sensitivity to surface and internal water content and soil moisture and roughness should be characterized. Moreover, given the importance of rainfall interception on the radar signals and its complexity, more research should be conducted on better estimating interception, under different conditions, for different types and stages of vegetation, and the effect of the distribution of intercepted water in the canopy on backscatter.

The future availability of sub-daily fine resolution data on surface and internal water content offers an extraordinary opportunity to study plant water dynamics from a new perspective, and at the landscape scales most relevant for understanding water and carbon exchanges in the climate system. By providing information on rapid surface and internal plant water dynamics, sub-daily spaceborne SAR has the potential to become a valuable source of data in the fields of hydrology, land surface modelling, climate modelling, numerical weather prediction and plant physiology.

## APPENDIX: ELECTROMAGNETIC MODEL SIMULATIONS

A physical model for corn, developed at the Tor Vergata University of Rome (Bracaglia et al., 1995; Della Vecchia et al., 2006), was used to illustrate contributions of soil and vegetation components to total backscatter, and the changes during the season. This model is based on radiative transfer theory and provides polarimetric backscatter of agricultural fields. It is able to simulate both scattering and extinction properties of vegetation elements and of the underlying soil applying the most suitable electromagnetic approximation, depending on the scatterer size and shape. Furthermore, it is able to take into account multiple scattering of any order and it can separate contributions of different scatterers in the vegetation canopy.

The inputs for the model are listed in Table 3.2. Soil root mean square (RMS) height was estimated using the meshboard approach described in Jang et al., 2005, and was measured in the period between sowing and crop emergence. Correlation length is very difficult to measure accurately, because it is extremely variable (Álvarez-Mozos et al., 2008). Therefore, we chose the correlation length which gave the best fit between simulated and observed  $\sigma^0$  during the bare soil period. Plant density was averaged over 40 randomly chosen samples. The model was run with a daily time step. Because the model does not account for surface canopy water, soil moisture values at 10:00 were used to ensure that dew had dissipated from the canopy at the observation time. Since water on leaves suppresses transpiration (Dawson and Goldsmith, 2018), the internal water content at 10:00 should be close to 6:00 observations. Time series of vegetation parameters were linearly interpolated. Similar to the observed  $\sigma^0$ , cross-polarized backscatter represents the average of VH and HV polarizations.

The model simulations (RMSE=3.91 dB) are presented in Fig. 3.10. Note that the observed co-polarized backscatter is underestimated by the model, while the cross-pol increase due to vegetation growth is very well reproduced. *Vegetation* scattering refers to the volume scattering by the vegetation layer. *Ground* scattering refers to direct scattering solely from the ground. *Vegetation-ground* scattering represents multiple scattering effects due to interactions between the vegetation and ground. *Double-bounce* scattering represents the contribution coming from specular reflection from the soil followed by specular reflection by stems, and viceversa.

Co-polarized backscatter was dominated by the direct ground contribution in the early season. Increasing VWC during the vegetative stages (Fig. 3.2) results in attenuation of the ground contribution, and an increase in the vegetation, vegetation-ground and double-bounce terms. Double-bounce scattering increases with stem growth and is most significant in VV during the early vegetative stages.

Both co-polarized  $\sigma^0$  simulations are dominated by direct vegetation scattering after May 16, when LAI>1, and VWC>1.5 kg m<sup>-2</sup>. After May 23, when LAI>3.5 and VWC>3.5 kg m<sup>-2</sup>,  $\sigma_{VV}^0$  simulations can be almost completely explained by direct scattering from vegetation in mid- and late season, and other scattering mechanisms are negligible. However, indirect and direct scattering from the ground still contribute to  $\sigma_{HH}^0$  to some degree in this period. These results are comparable to those of Stamenković et al., 2015, where a larger double bounce effect at HH polarization is observed, due to a much smoother soil surface. Cross-polarized backscatter ( $\sigma_{XP}^0$ ) was dominated by direct scattering from vegetation, even when the plants were still small.

Table 3.2: Input parameters for model simulation

| Parameter                     | Single value or time series |
|-------------------------------|-----------------------------|
| Frequency                     | 1.25 GHz                    |
| Incidence angle               | 40°                         |
| Soil rms height               | 2.5 cm                      |
| Soil correlation length       | 33 cm                       |
| Surface soil moisture (10:00) | Time series                 |
| Crop height                   | Time series                 |
| $M_g$ cylinders (stems)       | Time series                 |
| $M_g$ discs (leaves)          | Time series                 |
| No. of leaves                 | Time series                 |
| LAI                           | Time series                 |
| Stem height                   | Time series                 |
| Stem radius                   | Time series                 |
| Leaf area                     | Time series                 |
| Plant density                 | 8 plants m <sup>-2</sup>    |

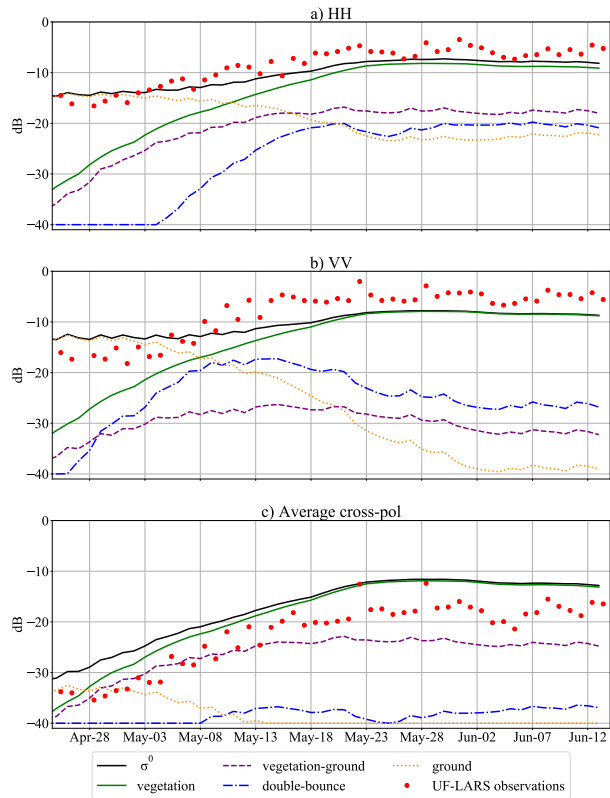


Figure 3.10: Tor Vergata model simulations for (a) HH-polarized backscatter, (b) VV-polarized backscatter, and (c) cross-polarized backscatter. UF-LARS observations at 10:00 are plotted for reference.

# 4

## EXTRAPOLATING CONTINUOUS VEGETATION WATER CONTENT TO UNDERSTAND SUB-DAILY BACKSCATTER VARIATIONS

*Chapter 3 showed that sub-daily L-band backscatter was sensitive to both transient rainfall interception, and slower daily cycles of internal canopy water and dew. These results demonstrate a potentially valuable application for the next generation of spaceborne radar missions. The results also show that an in-depth analysis of the role of vegetation water content (VWC) is challenging, because it requires sub-daily measurements of VWC changes which are notoriously hard to obtain. Future studies that aim to relate microwave observables to VWC would benefit from a more efficient method to detect sub-daily VWC. This chapter presents a methodology adopted from the tree physiology community to reconstruct continuous VWC from sap flow measurements and estimates of evapotranspiration. The results are used to demonstrate that sub-daily changes in backscatter are consistent with diurnal variability in VWC, in addition to surface canopy water and soil moisture.*

---

This chapter is based on:

Vermunt, P. C., Steele-Dunne, S. C., Khabbazan, S., Judge, J., and Van de Giesen, N. C. (2022). Extrapolating Continuous Vegetation Water Content to Understand Sub-daily Backscatter Variations, *Hydrology and Earth System Sciences* **26**, 1223-1241 .

## 4.1. INTRODUCTION

The long heritage of research on remote soil moisture and biophysical parameter retrieval has shown that backscatter is sensitive to dielectric properties of vegetation, which is strongly related to its water content (Konings et al., 2019; Steele-Dunne et al., 2017). For a long time, this sensitivity to vegetation water content (VWC), here defined as the weight of water captured inside the plant material above a square metre of ground ( $\text{kg m}^{-2}$ ), was considered a barrier to soil moisture retrieval. In the last decade however, backscatter sensitivity to VWC has been used for studies on plant hydraulics and water stress in agriculture and ecosystems (e.g. El Hajj et al., 2019; Frohling et al., 2011; Konings et al., 2017; Schroeder et al., 2016; Steele-Dunne et al., 2012; Steele-Dunne et al., 2019; van Emmerik et al., 2017).

The increasing temporal and spatial resolution of spaceborne radar observations creates opportunities for more detailed and extensive (eco)hydrological studies. In addition to the frequent C-band Synthetic Aperture Radar (SAR) observations from Sentinel-1 (Torres et al., 2012) and the RADARSAT Constellation Mission (Thompson, 2015), other frequencies such as the L- and S-band mission NISAR (launch planned in 2023), the L-band mission ROSE-L (2028), and the P-band mission BIOMASS (2023) will be available within the next decade (Pierdicca et al., 2019; Quegan et al., 2019; Rosen et al., 2017). Moreover, commercial providers such as Capella Space and ICEYE are building satellite constellations with X-band instruments (Farquharson et al., 2021; Ignatenko et al., 2020). These constellations will ensure multiple observations per day. As a result, the availability of spaceborne backscatter observations in the near future will offer a unique possibility to study vegetation water dynamics on different spatiotemporal scales.

However, we currently lack crucial knowledge on backscatter sensitivity to vegetation water dynamics. Soil moisture retrieval algorithms, for example, generally consider the confounding effects of vegetation water as time invariant or seasonally variant only (S.-B. Kim et al., 2017). Well-established electromagnetic models have been developed and calibrated based on seasonally variant VWC only (e.g. Bracaglia et al., 1995). Moreover, the effect of surface canopy water (SCW), i.e. dew or rainfall interception, is also usually ignored (Vermunt et al., 2020; Xu et al., 2021). The omission of sub-daily vegetation water dynamics causes potential retrieval errors Brancato et al., 2017 and, more importantly, hinders our understanding of the extent to which radar backscatter could be used to monitor vegetation water dynamics. Without this knowledge, the upcoming spaceborne observations cannot be used to their full potential.

Several studies have related observed diurnal backscatter cycles to vegetation water dynamics. Clear diurnal cycles were found in tower-based observations from forest stands (e.g. Hamadi et al., 2014; Monteith and Ulander, 2021) and agricultural cropland (e.g. Vermunt et al., 2020), as well as in aggregated satellite observations from larger forested areas (Konings et al., 2017; Paget et al., 2016; van Emmerik et al., 2017). These studies have made important contributions to the understanding of sub-daily backscatter behaviour. However, a persistent challenge is the lack of in situ data for ground truth validation. In situ soil moisture can be routinely measured using a variety of sensors (Cosh et al., 2016; Dobriyal et al., 2012). Surface canopy water can be measured continuously using leaf wetness sensors (Cosh et al., 2009; Vermunt et al., 2020). However, internal VWC is still generally measured using laborious destructive sampling, particularly in



agricultural fields (e.g. van Emmerik et al., 2015; Vreugdenhil et al., 2018; Ye et al., 2021). This is acceptable for monitoring seasonal changes, but is prohibitively time-consuming and labour-intensive for sub-daily variations. Hence, it is crucial to find a more efficient way to obtain continuous, quantitative estimates of sub-daily VWC variations.

For woody constituents in trees, dendrometers have been used to infer water content non-destructively after detrending, and similarly, time- and frequency-domain reflectometry (TDR and FDR) and capacitance-style sensors have been used to derive water content indirectly by measuring dielectric permittivity (Konings et al., 2021). Moreover, a water balance-style approach using sap flow sensors have been used by the tree physiology community to estimate diurnal changes in tree stem water storage (Čermák et al., 2007; Goldstein et al., 1998; Köcher et al., 2013; Meinzer et al., 2004; Phillips et al., 2008).

The objectives of this chapter were to test the potential of this non-destructive sap flow approach for estimating sub-daily VWC variations in herbaceous plants and to use these estimates to better understand what controls sub-daily variations in L-band backscatter. Specifically, we adapted this sap flow methodology, described in Sect. 4.2, to estimate 15 min changes in corn VWC using sap flow sensors and a weather station. An extensive data set from a field campaign in the Netherlands in 2019 was used to evaluate the adapted method against diurnal cycles of VWC obtained by destructive sampling. Finally, the technique was applied to reconstruct sub-daily VWC variability of multiple consecutive days from another field campaign in Florida in 2018. In this campaign, high temporal resolution tower-based polarimetric L-band backscatter was collected. The reconstructed VWC was used, together with simultaneously collected soil moisture and surface canopy water (SCW), to gain a better understanding of what controls sub-daily backscatter behaviour.

## 4.2. ESTIMATING DIURNAL VARIATIONS IN TREE WATER CONTENT USING SAP FLOW PROBES

Diurnal variations in internal VWC have been estimated in trees before, mainly in studies focused on understanding the functional role of stem water reserves on daily tree water use. A well-established in situ method uses sap flow probes at the base of the stem and in the crown (e.g. Čermák et al., 2007; Goldstein et al., 1998; Köcher et al., 2013; Meinzer et al., 2004; Phillips et al., 2008). This method is based on the time lag between transpiration and basal sap flow, as a result of a tree's hydraulic capacitance, which is the change in water content per unit change in water potential (e.g.  $\text{kg MPa}^{-1}$ ; Goldstein et al., 1998; Oguntunde et al., 2004). Morning transpiration, driven by the atmospheric evaporative demand, causes the depletion of internal VWC in the crown and, depending on the hydraulic capacitance, a drop in water potential. In response to the resulting potential gradient, sap flow rates increase to replenish the depleted VWC. As long as transpiration rates exceed basal sap flow rates, water is withdrawn from internal VWC, and when basal sap flow exceeds transpiration, internal VWC is refilled. Consequently, the diurnal variation in tree VWC could be calculated from the cumulative differences between basal sap flow and whole-crown transpiration (see the second term of Eq. 4.1).

$$\text{VWC}(t) = \text{VWC}(t_0) + \sum_{i=t_0}^t (F_i - T_i) \Delta t, \quad (4.1)$$

where  $\text{WVC}(t)$  is the estimated WVC at time  $t$ ,  $\text{WVC}(t_0)$  is a reference WVC at  $t = 0$ ,  $F$  is basal sap flow,  $T$  is whole-crown transpiration, both in mass per unit of time, and  $\Delta t$  is the duration of a time step.

In these studies on trees, whole-crown transpiration was estimated from branch and basal sap flow based on two assumptions. First, time lags between branch sap flow in the crown and transpiration were assumed to be negligible compared to time lags between branch and basal sap flow. Hence, the averaged daily cycles of sap flow in the monitored branches were assumed to approximate the cycles of whole-crown transpiration. Second, most studies assumed that the 24 h sums of whole-crown transpiration and basal sap flow were equal (Čermák et al., 2007; Goldstein et al., 1998; Köcher et al., 2013; Phillips et al., 2008). This assumption made it possible to estimate whole-crown transpiration rates by first dividing averaged branch sap flow by its daily sum and then multiplying by the daily sum of basal sap flow. The corresponding assumption is that all water that is withdrawn from internal WVC is replaced within 24 h.

### 4.3. DATA AND METHODS

Section 4.3.1 relates to the adjustments and data required to make the sap flow approach (Sect. 4.2) applicable to corn. Data from a field campaign in the Netherlands in 2019 were used to evaluate the adjusted method. Section 4.3.2 relates to the methodology and data used from our field campaign in Florida in 2018 for interpreting sub-daily backscatter behaviour.

#### 4.3.1. APPLYING THE SAP FLOW APPROACH TO ESTIMATE DIURNAL VARIATIONS IN CORN WVC

##### ADJUSTMENTS AND EVALUATION OF THE SAP FLOW APPROACH

We investigated the potential of the sap flow method (Sect. 4.2) for estimating diurnal WVC variations in corn plants. The largest differences between corn plants and trees are related to hydraulic capacitance and structure. Corn plants have much lower hydraulic capacitance than most trees (Langensiepen et al., 2009) and, hence, shorter time lags between transpiration and basal sap flow. As a consequence, installing a sap flow sensor as a surrogate for transpiration would be problematic, since the assumption of a negligible time lag between transpiration and upper sap flow, compared to the lag with basal sap flow, is invalid. Moreover, transpiring corn leaves are somehow evenly distributed across the stem, in contrast to trees with a crown, which makes the placement of a second sensor to represent transpiration nearly impossible. For these reasons, we estimated transpiration using indirect estimates of reference evapotranspiration ( $\text{ET}_0$ ) instead. Details from sap flow measurements and  $\text{ET}_0$  estimates are given in Sect. 4.3.1.

A widely used approach to derive transpiration from  $\text{ET}_0$  is a linear conversion using crop factors, e.g. the FAO 56 dual-crop coefficient model (R. G. Allen et al., 1998). However, in many cases, these estimations systematically over- or underestimate direct observations of transpiration (Ding et al., 2013; Rafi et al., 2019) or sap flow (Langensiepen et al., 2009), while basal sap flow and transpiration at the leaves must equal over a sufficiently long time period (Swanson, 1994). For our data sets, Penman–Monteith-derived transpiration (R. G. Allen et al., 1998) is systematically lower than measured sap flow.

Table 4.1: The three tested approaches to estimate transpiration (T) using Penman-Monteith derived ET<sub>0</sub> estimates and sap flow measurements.

| Approach                 | assumptions                                                                              | equations                                                 |
|--------------------------|------------------------------------------------------------------------------------------|-----------------------------------------------------------|
| Linear-24h               | withdrawn water is replaced within 24-hours.<br>T is linearly related to ET <sub>0</sub> | $T(t) = ET_0(t) F_{24h} / ET_{0_{24h}}^*$<br>(4.2)        |
| Linear- multiple days    | withdrawn water is replaced within $n$ days.<br>T is linearly related to ET <sub>0</sub> | $T(t) = ET_0(t) F_{nd} / ET_{0_{nd}}^*$ (4.3)             |
| Nonlinear - CDF-matching | withdrawn water is replaced within $n$ days.<br>CDF of T equals CDF of F                 | $T(t) = a^\dagger ET_0(t) + b^\dagger ET_0(t)^2$<br>(4.4) |

\*subscripts 24h and nd relate to the 24-hour sum and  $n$ -days sum, respectively.

†  $a$  and  $b$  are found by a 2<sup>nd</sup> order polynomial fit through ranked F and ET<sub>0</sub> data, illustrated in Fig. 4.4(c) .

Because sap flow is our most direct measurement, we chose to estimate transpiration by rescaling ET<sub>0</sub> estimates using sap flow measurements. This means that information on the diurnal shape of ET<sub>0</sub> is derived from the Penman–Monteith equation and that these ET<sub>0</sub> estimates are then scaled so that the resulting transpiration estimates are consistent with sap flow over a given period of time.

We tested three different approaches to rescale ET<sub>0</sub> estimates using sap flow measurements. The first approach was similar to the rescaling of branch sap flow to whole-crown transpiration in trees, described in Sect. 4.2. Transpiration was assumed to equal basal sap flow during a 24 h period, and 15 min ET<sub>0</sub> estimates were divided by their 24 h sum and then multiplied by the 24 h sum of basal sap flow (see Eq. 2 in Table 4.1).

However, the assumption of complete replacement of withdrawn water within 24 h may not always hold. This is, for example, the case when water accumulates as a result of growth or when a plant is unable to replace the transpired water within a day as a result of stress. Therefore, we also tested the effect of either relaxing this assumption or using multiple days instead, i.e. 3, 5, or 7 consecutive days surrounding the day of interest or all measured days in the data set. Both approaches assume a simple, linear relation between ET<sub>0</sub> and transpiration. It will be shown that this assumption can cause an offset between the timing of the diurnal cycles of sampled and reconstructed VWC. This issue was addressed by adopting the cumulative distribution function (CDF) matching method, previously used to rescale satellite-derived surface soil moisture to observations (Brocca et al., 2011; Drusch et al., 2005; Reichle and Koster, 2004). This nonlinear approach removes systematic differences between two data sets by matching the CDFs of both data sets (Brocca et al., 2011). Here, we matched the CDFs of the ET<sub>0</sub> and sap flow data. This was achieved by first ranking all 15 min data from both data sets from low to high values and then fitting a second-order polynomial function through the scatterplot of both ranked data sets. Subsequently, this function was used to convert the 15 min ET<sub>0</sub> data to transpiration estimates. CDF matching was also performed for 1, 3, 5, and 7 consecutive days and all available days. Figure 4.4 illustrates CDF matching and

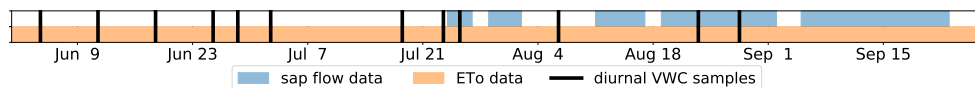


Figure 4.1: Availability of the data required to evaluate the adjusted methodology for estimating 15 min VWC variations. The availability of the sap flow,  $ET_0$ , and sampling data matched on 25 July and 23 and 28 August.

its results for 3 d of our data.

VWC samples obtained by destructive sampling during the 2019 campaign (Sect. 4.3.1) were used to validate the method. For the selected days (Fig. 4.1), we used one of the five sampling times to constrain the daily cycle ( $VWC(t_0)$  in Eq. 4.1). The other four independent samples were compared against the estimated diurnal cycle of VWC variations. For each day, we calculated the root mean square error (RMSE) between the four independent samples and reconstructed VWC on these four times. All five samples were used as ( $VWC(t_0)$ ) once to determine the best time to constrain the reconstruction.

In summary, we adapted and evaluated the sap flow methodology to estimate diurnal cycles of corn VWC through the following three steps.

1. The diurnal cycle of transpiration was estimated from  $ET_0$  and sap flow data, using three different approaches (Table 4.1).
2. Sub-daily variations in VWC were estimated by calculating the cumulative difference between 15 min basal sap flow and transpiration estimates (Eq. 4.1).
3. The resulting estimates of diurnal VWC variations were compared against destructive measurements of VWC.

## EXPERIMENTAL SITE AND DATA COLLECTION

### Experimental site 2019

The field campaign in The Netherlands was conducted in Reusel (51.319° N, 5.173° E), at Van Den Borne Aardappelen. There, field corn was planted on a sandy soil with a density of eight plants per square metre (hereafter  $m^{-2}$ ), and harvested, for silage after the required senescence, 148 d after planting. The Netherlands has a temperate maritime climate. However, maximum national temperature records were broken close to the field site during the growing season of 2019, and it was the second anomalously dry summer in a row (Bartholomeus et al., 2020).

### Sap flow

Sap flow was monitored near the base of the stem using stem flow gauges produced by Dynamax Inc. (Houston, TX, USA). See Chapter 2 for details about these sensors. Sensor output ( $g\ h^{-1}$ ) is converted to millimetres per 15 min ( $mm\ 15\ min^{-1}$ ) using the density of liquid water and the planting density. Because the sensors are designed to fit a certain range of stem diameters, we collected data in the mid- and late season.

In 2019, a maximum of two sensors were installed due to power limitations. Because one sensor failed, the used data are from a single sensor. Gaps in the time series were caused by disturbances in the connection with the battery.

### Reference evapotranspiration

A weather station was installed at the edge of the experimental site, with a ECH2O rain model ECRN-100 rain gauge, Apogee SP-212 pyranometer (solar radiation), a Davis Cup anemometer (wind and gust speed and wind direction), and a HOBO Temperature/RH Smart Sensor model S-THB-M008 (temperature and relative humidity). Reference evapotranspiration ( $ET_0$ ) was estimated using the Penman–Monteith approach described by Zotarelli et al., 2010.

### Sampling

Plant fresh ( $m_f$ ) and dry ( $m_d$ ) biomass were measured by destructive sampling (see Chapter 2, section 2.2.3). Field-representative VWC ( $\text{kg m}^{-2}$ ) was estimated by multiplying the difference between fresh and dry biomass per plant (kg) with the number of plants per  $\text{m}^2$  ( $\rho_{\text{plant}}$ ; see Eq. 5.1).

$$\text{VWC} = (m_f - m_d) \rho_{\text{plant}}. \quad (4.8)$$

In 2019, we aimed to capture full diurnal cycles of VWC. Hence, we sampled at five equally distributed times, between sunrise and sunset, on 12 d spread throughout the season. Seasonal VWC variations were monitored by predawn sampling only.

Figure 4.1 shows the availability of the data required to evaluate the adjusted methodology for estimating 15 min VWC variations. The availability of sap flow,  $ET_0$ , and VWC sampling data matched on 25 July and 23 and 28 August.

### Surface canopy water and soil moisture

Measurements of surface canopy water (dew and interception) and root zone soil moisture were used as ancillary data sets to support the evaluation of the reconstructed VWC estimations. Surface canopy water (SCW) was monitored using PHYTOS 31 leaf dielectric wetness sensors. A total of, three sensors were installed on different heights in the vegetation layer, and one sensor failed during the season. Measured leaf areas were used to convert sensor output to full-canopy SCW ( $\text{kg m}^{-2}$ ). Details of this conversion and sensor properties are described in sections 3.2.3 and 3.2.3, respectively.

Soil moisture ( $\theta$ ) was observed in two pits with 15 min resolution, using EC-5 sensors at 5, 10, 20, 40, and 80 cm depth. These measurements were averaged based on depth. Root zone soil moisture was estimated by integrating the measurements from all depth over a soil column of 100 cm, based on the thickness of the soil layer associated with the depth of the sensor.

## 4.3.2. INTERPRETING THE BEHAVIOUR OF SUB-DAILY L-BAND BACKSCATTER

### APPROACH AND DATA REQUIREMENT

To gain a better understanding of what controls sub-daily L-band backscatter behaviour, we analysed tower-based observations using continuous time series of the three moisture stores in the corn field, namely (1) VWC, (2) SCW, and (3) surface soil moisture ( $\theta$ ). Details of the collection of these time series are given in Sect. 4.3.2. The longest period

for which we had all data available was from 4 June 00:00 LT to 13 June 10:15 LT. During this period, the corn is at maximum height and leaf area index (LAI) and is 1–2 weeks before harvest on 18 June. All analyses were conducted for this period.

Insights in the separate effects of the three different moisture stores on sub-daily backscatter ( $\sigma^0$ ) variations were gained by quantifying their relations through multiple linear regression. The relation between sub-daily backscatter variations and changes in these dynamic moisture stores was described as follows:

$$\begin{aligned} \sigma^0(t) = & \sigma_{t_0}^0 + a(\theta_t - \theta_{t_0}) + b(\text{VWC}_t - \text{VWC}_{t_0}) \\ & + c(\text{SCW}_t - \text{SCW}_{t_0}), \end{aligned} \quad (4.9)$$

where  $t_0$  is the first radar acquisition time of the day (01:00 LT) and assumes linear relations between  $\sigma^0$  and the individual moisture stores. The regression coefficients  $a$  ( $\text{dB m}^{-3}$ ),  $b$  ( $\text{dB kg}^{-1} \text{m}^{-2}$ ), and  $c$  ( $\text{dB kg}^{-1} \text{m}^{-2}$ ) were used to quantify the change in backscatter within a day as a result of change in moisture and were derived for each polarization separately.

#### EXPERIMENTAL SITE AND DATA COLLECTION

##### Experimental site 2018

The field campaign in Florida, USA, was conducted in Citra (29.410° N, 82.179° W), at the Plant Science Research and Education Unit (PSREU) of the University of Florida and the Institute of Food and Agricultural Sciences (UF/IFAS). Sweetcorn was planted in a sandy soil, with a density of 7.9 plants per  $\text{m}^{-2}$ , and harvested after 66 d, in mid-June, for human consumption. The climate of this area in Florida is humid subtropical, and the 2018 spring growing season was characterized by high temperatures, high-intensity rainfall, and thunderstorms.

##### Backscatter

High temporal resolution L-band backscatter data were collected with the polarimetric University of Florida L-band Automated Radar System (UF-LARS) throughout the growing season of 2018. This system was mounted on a Genie aerial work platform at a height of 14 m above the ground. The scatterometer scanned the cornfield, with an incidence angle of 40°, and acquired 16 observations spread throughout the day in the late season. The installation of sensors and vegetation sampling was performed outside the arc swept by the radar. A comprehensive description of the observations and the UF-LARS system can be found in section 2.2.1 and Nagarajan et al., 2014, respectively. *Cross-polarization* (cross-pol) is used to refer to the average of the HV- (horizontal transmit and vertical receive) and VH-polarized (vertical transmit and horizontal receive) backscatter. The symbols used for VV-, HH-, and cross-pol backscatter are  $\sigma_{\text{VV}}^0$ ,  $\sigma_{\text{HH}}^0$  and  $\sigma_{\text{XP}}^0$ , respectively.

##### Reconstruction of diurnal VWC variations for multiple consecutive days

To support the analysis of variations in the L-band backscatter, a 10 d time series of diurnal VWC variations was reconstructed for the 2018 data. The methodology used for the reconstruction was based on adjustments and evaluation of the sap flow approach presented in Sect. 4.3.1. The required sap flow and  $\text{ET}_0$  data sets were similar but slightly

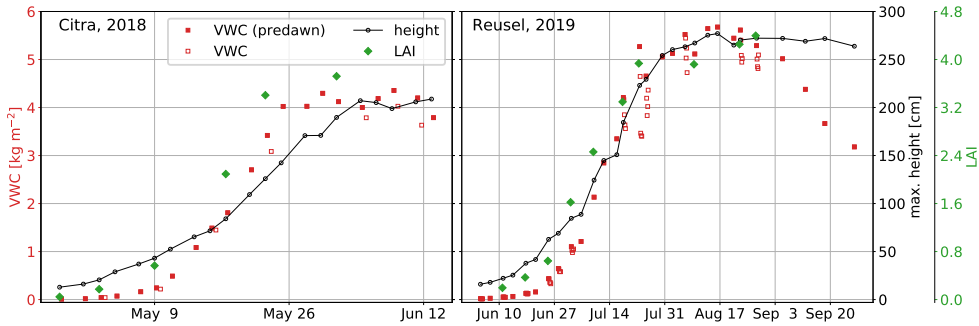


Figure 4.2: Vegetation water content (VWC), crop height, and leaf area index (LAI) from the field experiments in Citra (2018) and Reusel (2019). Filled red markers indicate predawn measurements, while open markers indicate non-predawn measurements at 18:00 LT (2018) and morning to sunset (2019).

different. In 2018, four sap flow sensors were installed simultaneously on four different plants, and the data were averaged. Gaps in the time series were caused by disturbances in the connection with the battery or solar panel.

Meteorological data with 15 min resolution were obtained from the nearby Florida Automated Weather Network (FAWN) weather station, located within 600 m from the experimental field. Observations of rainfall, air temperature (2 m), solar radiation, relative humidity, and wind speed were downloaded from the Report Generator (<https://fawn.ifas.ufl.edu/data/reports/>, last access: 10 October 2018).  $ET_0$  was estimated using the same Penman–Monteith approach described by Zotarelli et al., 2010.

In contrast to the 2019 data set, VWC samples were not collected to capture the full diurnal cycle. Instead, these samples were obtained 4 times per week, i.e. 3 d at 06:00 LT, and also at 18:00 LT on one of these days, originally to capture differences between morning and evening passes for a sun-synchronous satellite such as SMAP (Entekhabi et al., 2010). Moreover, the presented VWC data for 2018 are averages of eight plants instead of six. The samples were used to constrain the reconstructed VWC variations.

The period of consecutive days for the analysis was limited by the availability of sap flow data. A 10 d time series was found in mid- to late season which contained continuous sap flow and weather data, L-band backscatter, and 5 sampling days. On these days, samples were used to constrain the VWC record. On the 5 d without sampling, the VWC records were constrained either at the end of previous sampling day (forward reconstruction) or at the start of next sampling day (backward). In case there was a gap between the forward and backward reconstructions, the average of both was considered the best estimate of VWC.

### Soil moisture and surface canopy water

For the analysis of sub-daily variations in the L-band backscatter, we also collected 15 min variations in surface soil moisture, at 5 cm depth, and SCW. Together with VWC, they form the moisture stores of a cornfield which are considered to affect sub-daily backscatter. Details of the sensors and measurements are described in Sect. 4.3.1 and extensively in Vermunt et al., 2020.



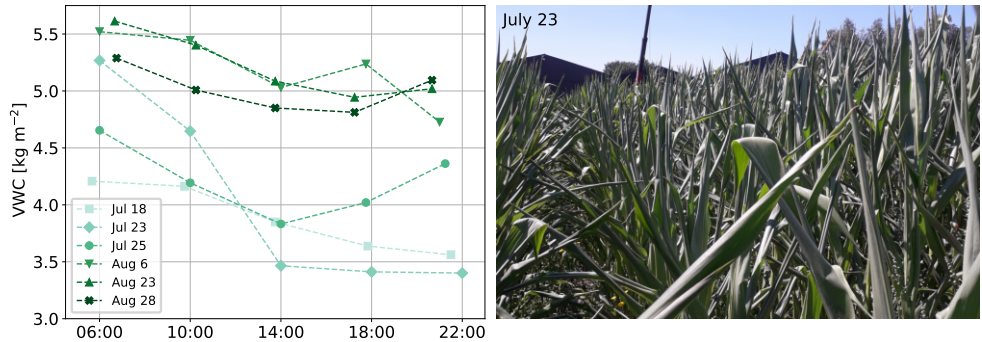


Figure 4.3: Sampled vegetation water content (VWC) in the mid-season, 2019 (a), and a picture of rolled leaves (b), taken around the third measurement on 23 July, as a sign of drought stress.

## 4.4. RESULTS

### 4.4.1. SEASONAL AND DIURNAL VARIATION OF VEGETATION WATER CONTENT

Figure 4.2 illustrates the seasonal and diurnal variations of VWC (kg m<sup>-2</sup>) from destructive sampling in the 2018 and 2019 campaigns. From the early to mid-season, VWC increased as a result of biomass accumulation. The field corn from 2019 was allowed to senesce before harvest, resulting in a significant reduction in water storage in the plants from 23 August onward. The sweetcorn from 2018 was harvested before considerable senescence.

The open markers are the non-predawn measurements, which were at 18:00 LT (2018), and at four evenly distributed times between sunrise and sunset (2019). The range of these latter diurnal measurements gives an indication of the amplitude of the daily cycle of VWC. On most days, the diurnal minimum was 10%–20% lower than the predawn water storage. An exception was 23 July, when predawn water storage was depleted by 35.4% during the day. Figure 4.3 magnifies the mid-season measurements and illustrates the difference between water depletion in the non-stressed conditions compared to the stressed date. The photograph was taken around the third measurement on 23 July. This picture shows leaf rolling, which is a mechanism to reduce the leaf area exposed for transpiration and a sign of drought stress. Normal-shaped leaves were observed again as a result of irrigation, which was applied right after the last sampling on 23 July, in order to ensure the crop's survival.

### 4.4.2. RECONSTRUCTIONS OF CONTINUOUS, SUB-DAILY VARIATIONS IN VEGETATION WATER CONTENT

As described in Sect. 4.3.1, we tested three approaches to estimate transpiration from  $ET_0$  and sap flow. As an alternative to the straightforward linear conversions, we proposed to test the nonlinear CDF matching principle (Table 4.1). Figure 4.4 illustrates the procedure of estimating transpiration using this principle, using 3 d of sap flow and  $ET_0$  data. We take 25 July 2019 as an example and use the data from 24 and 26 July as well (Fig. 4.4a).



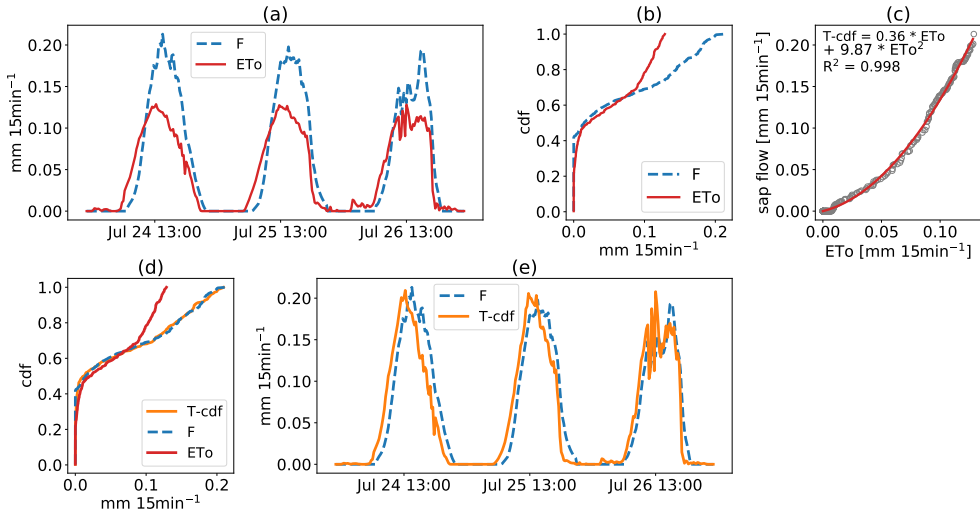


Figure 4.4: Example of  $ET_0$  rescaling to approximate transpiration (2019 campaign), using the CDF matching approach. (a) Sap flow ( $F$ ) and reference evapotranspiration ( $ET_0$ ) data from 24–26 July 2019. (b) Cumulative distribution function (CDF) of both data sets in this period. (c) Second-order polynomial fit through ranked  $F$  and  $ET_0$  data, used to derive the CDF-matched transpiration estimate (T-cdf), which was added to the CDF plot in panel (d). Panel (e) shows the final result of the CDF matching.

On 25 July, which was particularly warm and sunny, we measured a maximum temperature of  $39.0^\circ\text{C}$  in the field. Figure 4.4b illustrates the difference between the CDFs of sap flow and  $ET_0$ , which is particularly evident at the 35% highest rates ( $< 0.07 \text{ mm } 15 \text{ min}^{-1}$ ),  $ET_0$  rates were slightly higher than sap flow rates. As these systematic differences between both rates may be unrealistic, a second-order polynomial was fitted through the scatterplot with ranked  $ET_0$  and sap flow data (Fig. 4.4c) and was used to match the CDFs (Fig. 4.4d). The resulting CDF-matched transpiration estimate (T-cdf; Fig. 4.4e) was used to estimate  $\Delta\text{VWC}$  at any point in time using the approach described in Fig. 4.5.

The procedure to reconstruct 15 min changes in VWC is depicted in Fig. 4.5, again with 25 July as an example. Figure 4.5a illustrates the effects of the three approaches on estimate transpiration from  $ET_0$  and sap flow (Table 4.1). T-cdf and T-3 d represent the CDF-matched and linear estimates of transpiration, for which 3 d of data were used, i.e. 24–26 July. What stands out is that the CDF-matched rescaling (T-cdf) provides a significantly higher peak compared to the linear rescaling (T-24 h and T-3 d). On the other hand, when  $ET_0$  rates are  $0.09 \text{ mm } 15 \text{ min}^{-1}$  or lower, T-cdf was lower than the linear estimates. Both linear transpiration estimates were close in this particular case, which means that the ratio of the 24 h sum of sap flow over  $ET_0$  was close to the ratio of the 3 d sum of sap flow over  $ET_0$ . Figure 4.5b shows the diurnal cycles of basal sap flow ( $F$ ) and transpiration. Here, the simplest linear transpiration estimate (T-24 h) was depicted as an example. The difference between sap flow and transpiration gave the estimated depletion and refilling of internal water storage (Fig. 4.5c). If transpiration rates exceeded sap flow rates at some point in time, the line is below zero, which indicates a deple-

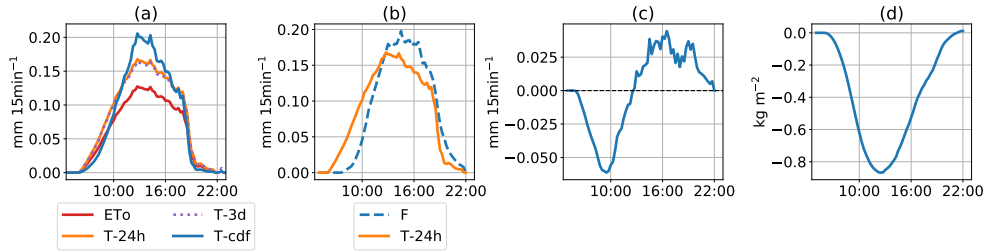


Figure 4.5: A four-step procedure to reconstruct the diurnal variation in VWC. An example for 25 July 2019. Panel (a) shows the diurnal cycles of reference evapotranspiration ( $ET_0$ ) and the three transpiration estimates (see Table 4.1). Panel (b) shows the diurnal cycles of sap flow ( $F$ ) and one of the transpiration estimates (T-24 h). Panel (c) is the difference between sap flow and transpiration, where negative values indicate depletion of water storage, and positive values indicate refill. Panel (d) illustrates the resulting cumulative change in stored water ( $\Delta VWC$ ) during the day.

4

tion of water storage. Positive values indicate refilling. Finally, the cumulative difference between sap flow and transpiration represents the diurnal change in plant water storage or  $\Delta VWC$  (Fig. 4.5d). The minimum VWC was reached around 12:45 LT, when  $0.87 \text{ kg m}^{-2}$  of the predawn water storage was depleted. This is close to the maximum diurnal difference of  $0.82 \text{ kg m}^{-2}$  observed on that day from destructive sampling (Fig. 4.3).

Diurnal cycles of VWC were reconstructed for both linear and nonlinear transpiration estimates, using  $\Delta VWC$  (Fig. 4.5d) and one destructive sample (Figs. 4.2 and 4.3) per day as a constraint. Results were compared against the other destructive samples. The effect of both the time of the constraint and the number of days considered for the transpiration estimation on the VWC reconstructions were evaluated. The RMSEs of the 2019 data are presented in Tables 4.2–4.3. A general optimal combination of the time of the constraint and the number of days to consider could not be found. Using CDF-matched transpiration estimates resulted in a better agreement with the destructive sampling data than using linear correction in 80 % of the cases. The best reconstructions from 2019 (Tables 4.2 and 4.3) are presented in Fig. 4.6 and differentiated by the approach to estimate transpiration. Differences between environmental conditions are shown in Fig. 4.7. Figure 4.6 illustrates the improvement of the reconstruction when using more than 1 d of data for the estimation of transpiration (second and third rows). The upper row clearly shows that the linear 24 h approach does not allow for a difference between the start- and end-of-day VWC, while the inclusion of multiple days does. In addition, the reconstruction on 25 July illustrates the possible improvement that CDF matching can have. On 25 July and 28 August, the RMSEs of the lowest plots were 8 % and 12 % of the amplitude of the diurnal cycles, respectively. On 23 August, the agreement is poor, especially later in the day, and this percentage is 36.9 %. On this day, reconstructions and samples disagree for all three approaches to estimating transpiration but less so for the CDF matching procedure.

For the 2018 campaign, we had a maximum of two VWC samples per day. Table 4.4 shows the offset between one of the samples and the reconstructed VWC, which was constrained by the other sample for 4, 8, and 11 June. The lowest offsets were found when transpiration was estimated using all data (12 d), and when CDF matching was

Table 4.2: Root mean squared error (RMSE) between reconstructed and sampled VWC. The rows represent time of constraining the reconstruction, while the columns represent the considered period for linear ETo correction

|           | July 25 |        |          | August 23 |        |        |        |          | August 28 |        |        |        |          |
|-----------|---------|--------|----------|-----------|--------|--------|--------|----------|-----------|--------|--------|--------|----------|
|           | 1 day   | 3 days | all data | 1 day     | 3 days | 5 days | 7 days | all data | 1 day     | 3 days | 5 days | 7 days | all data |
| predawn   | 0.212   | 0.272  | 1.107    | 0.369     | 0.310  | 0.256  | 0.282  | 0.547    | 0.178     | 0.097  | 0.095  | 0.063  | 0.352    |
| morning   | 0.314   | 0.369  | 1.082    | 0.500     | 0.444  | 0.389  | 0.416  | 0.655    | 0.176     | 0.110  | 0.108  | 0.078  | 0.315    |
| afternoon | 0.187   | 0.220  | 0.704    | 0.375     | 0.346  | 0.318  | 0.331  | 0.468    | 0.129     | 0.090  | 0.089  | 0.075  | 0.227    |
| evening   | 0.266   | 0.321  | 1.036    | 0.446     | 0.392  | 0.337  | 0.364  | 0.601    | 0.206     | 0.138  | 0.136  | 0.106  | 0.351    |
| sunset    | 0.247   | 0.311  | 1.131    | 0.516     | 0.448  | 0.379  | 0.413  | 0.706    | 0.150     | 0.074  | 0.072  | 0.047  | 0.317    |

Table 4.3: Root mean squared error (RMSE) between reconstructed and sampled VWC. The rows represent time of constraining the reconstruction, while the columns represent the considered period for CDF-matching

|           | July 25 |        |          | August 23 |        |        |        |          | August 28 |        |        |        |          |
|-----------|---------|--------|----------|-----------|--------|--------|--------|----------|-----------|--------|--------|--------|----------|
|           | 1 day   | 3 days | all data | 1 day     | 3 days | 5 days | 7 days | all data | 1 day     | 3 days | 5 days | 7 days | all data |
| predawn   | 0.155   | 0.140  | 0.070    | 0.303     | 0.380  | 0.295  | 0.310  | 0.458    | 0.135     | 0.112  | 0.153  | 0.149  | 0.379    |
| morning   | 0.114   | 0.104  | 0.124    | 0.296     | 0.390  | 0.313  | 0.331  | 0.508    | 0.121     | 0.078  | 0.100  | 0.088  | 0.286    |
| afternoon | 0.140   | 0.136  | 0.125    | 0.309     | 0.351  | 0.311  | 0.319  | 0.402    | 0.091     | 0.060  | 0.075  | 0.067  | 0.212    |
| evening   | 0.094   | 0.081  | 0.113    | 0.244     | 0.333  | 0.259  | 0.276  | 0.451    | 0.142     | 0.084  | 0.103  | 0.083  | 0.306    |
| sunset    | 0.177   | 0.162  | 0.083    | 0.471     | 0.548  | 0.460  | 0.474  | 0.623    | 0.102     | 0.070  | 0.106  | 0.097  | 0.325    |

applied. Consequently, we used the transpiration calculated based on this combination for further use of reconstructed VWC.

Table 4.4: Offset between reconstructed and sampled VWC. The rows represent the method used for transpiration estimation, while the columns represent the considered period.

|        | June 4 |        |        |          | June 8 |        |        |        |          | June 11 |        |        |          |
|--------|--------|--------|--------|----------|--------|--------|--------|--------|----------|---------|--------|--------|----------|
|        | 1 day  | 3 days | 5 days | all data | 1 day  | 3 days | 5 days | 7 days | all data | 1 day   | 3 days | 5 days | all data |
| linear | 0.202  | 0.250  | 0.149  | 0.055    | 0.412  | 0.071  | 0.241  | 0.022  | 0.022    | 0.556   | 0.790  | 0.739  | 0.543    |
| cdf    | 0.134  | 0.180  | 0.185  | 0.063    | 0.292  | 0.106  | 0.209  | 0.147  | 0.128    | 0.456   | 0.476  | 0.521  | 0.267    |

#### 4.4.3. RECONSTRUCTING A RECORD OF MULTIPLE DAYS

Figure 4.8 shows the procedure for reconstructing the 10 d VWC record from 2018 data. On 4, 8, and 11 June, evening samples (18:00 LT) were used as constraints rather than predawn samples (06:00 LT), which resulted in smaller gaps between consecutive days (Fig. 4.8c). On days without sampling, VWC records were the averages of forward or backward reconstructions. On 9 and 10 June, the weighted average based on the distance to the sampling date was considered as the best estimate of VWC.

The diurnal VWC pattern on 5 and 6 June seems physically implausible because one would not expect an enormous increase in VWC on the warmest and driest day (5 June) and a drop on the most rainy/cloudy day (6 June). Despite the advantage of CDF matching, as opposed to linear conversion to better reflect diurnal extremes, the anomalous dynamics of 5 and 6 June are not captured sufficiently.

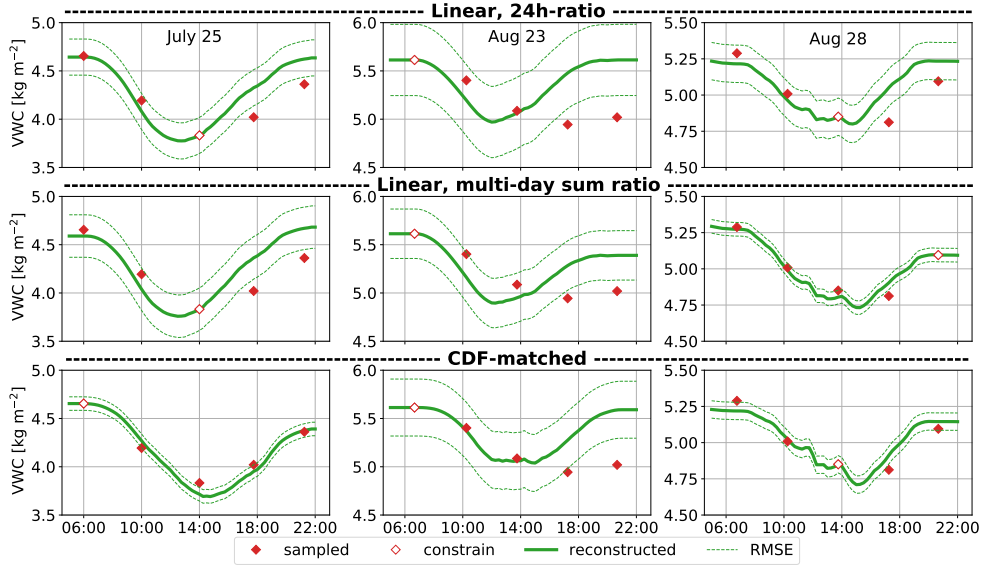


Figure 4.6: Best diurnal VWC reconstructions for 25 July and 23 and August 28 (2019) for three different methods of estimating transpiration. The upper row shows the results for using the simplest, linear estimate of transpiration. The middle row shows the reconstructions using linear estimates of transpiration but now considering 3, 5, and 7 d rather than 24 h. The lower row shows the results after CDF matching, considering all data, and 5 and 3 d for the CDF matching, respectively. The dashed green lines represent one RMSE above and one RMSE below the reconstructed VWC. The measurement which is used to constrain the reconstructed line is accentuated with an open marker.

#### 4.4.4. THE EFFECT ON SUB-DAILY L-BAND BACKSCATTER

Figure 4.9 illustrates the potential value of reconstructing VWC records for interpreting the time series of microwave remote sensing data, in this case L-band backscatter. The upper three panels show the VV- (vertically), HH- (horizontally) and cross-polarized backscatter coefficients, respectively. Figure 4.9d shows the sampled and reconstructed VWC, together with the total canopy water (CW), which is the sum of the reconstructed VWC and SCW (kg m<sup>-2</sup>). The latter is either rainfall interception, which is characterized by rapid increases and is often transient because of daytime evaporation, or dew formation, which accumulates gradually during the night and dissipates quickly after sunrise. Figure 4.9e shows the volumetric soil moisture at -5 cm depth.

Sub-daily variability of > 2 dB was found in all three polarizations. A sharp backscatter increase after rainfall was observed in all polarizations. Slow downward trends were also found, corresponding with the drydown in soil moisture. However, on a sub-daily timescale, the backscatter variability shows strong similarities with diurnal patterns of canopy water (Fig. 4.9d). These diurnal cycles are most clearly visible in VV-pol. Figure 4.10 magnifies the diurnal variations for 3 d without rainfall, i.e. 7, 9, and 11 June. These days demonstrate clear similarities between the diurnal behaviour of the backscatter, mainly VV- and cross-pol, and canopy water. These similarities are particularly present in the period between midnight and mid-afternoon, when surface soil moisture is rela-

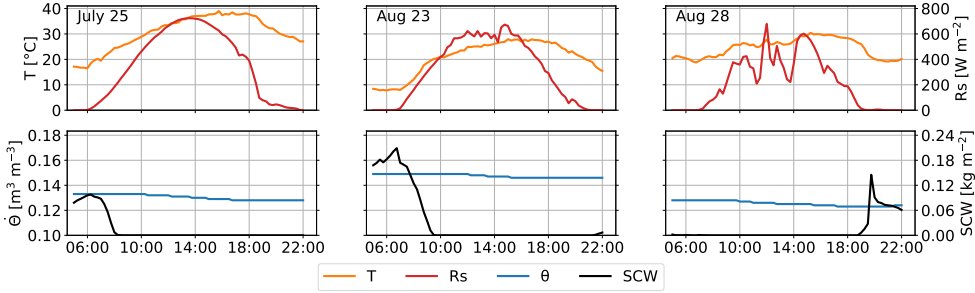


Figure 4.7: Environmental conditions on the sampling days of 25 July and 23 and 28 August (2019). The upper row shows air temperature ( $T$ ) and solar radiation ( $R_s$ ), and the lower row shows root zone soil moisture ( $\theta$ ) and surface canopy water (SCW).

Table 4.5: Estimated regression coefficients per polarization for the period June 7-13, 2018 (equation 4.9).

|                                          | VV-pol | HH-pol | Cross-pol |
|------------------------------------------|--------|--------|-----------|
| $a$ [dB/m <sup>3</sup> m <sup>-3</sup> ] | 24.06  | 39.47  | 38.83     |
| $b$ [dB/kgm <sup>-2</sup> ]              | 2.93   | 2.29   | 2.45      |
| $c$ [dB/kgm <sup>-2</sup> ]              | 0.62   | 0.38   | 0.73      |

tively stable. In fact, when randomly occurring rain events are excluded, the sub-daily backscatter behaviour can be analysed using the following three distinct sub-daily periods: (1) from midnight to early morning, (2) from early morning to afternoon, and (3) from afternoon to midnight. The aggregated data in Fig. 4.11 help to visualize the dynamics in these periods. Because rain fell more often in the afternoon and evening, the exclusion of periods with rainfall led to data aggregation across 9, 6, and 4 d in these three periods, respectively. Around midnight, dew started to form until its peak between 07:00 and 07:30 LT, which is within 1 h after sunrise around 06:30 LT. In this same period, VWC was stable and surface soil moisture decreased slightly. VV- and cross-polarized backscatter increased, following dew formation, while HH-polarized stayed relatively stable. From early morning (07:30 LT) to afternoon (14:00 LT), dew dissipated and VWC dropped significantly. The same holds for backscatter in all polarizations, while surface soil moisture was still relatively stable. Finally, the last period of the day is characterized by the refilling of the plant's internal water storage and a decrease in soil moisture. The fact that backscatter in all polarizations remains relatively constant between 15:00 and 19:30 LT suggests the counterbalancing effects of soil moisture and VWC on backscatter in this period. During the last four aggregated acquisitions between 19:00 and 21:30 LT, VV- and cross-polarized backscatter show a slightly increasing trend similar to VWC.

The separate effects of the different moisture stores on backscatter ( $\sigma^0$ ) were quantified through multiple linear regression. Because we considered the VWC reconstructions from 5 and 6 June as being less reliable, the period between 7 and 13 June was used for the regression. Table 4.5 presents the estimated regression coefficients found for this period (see Eq. 4.9). A summary of the multiple regression statistics is given in

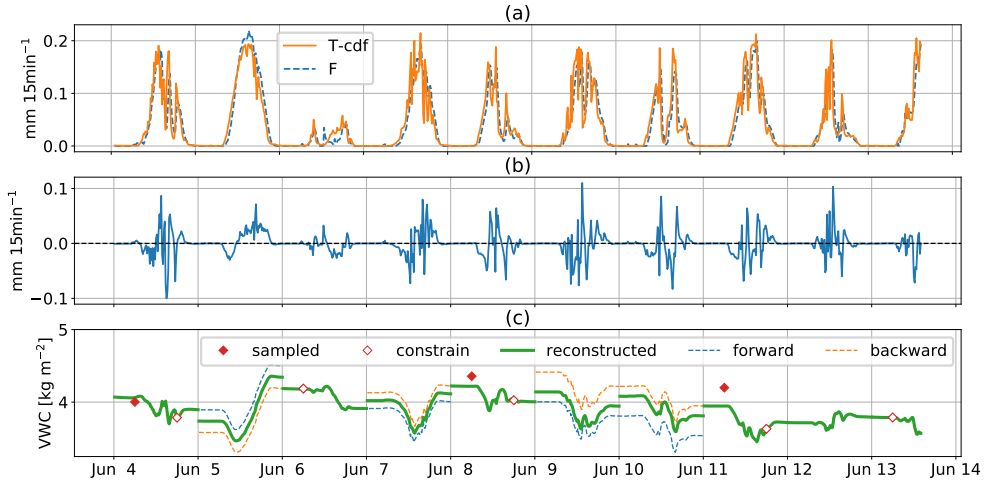


Figure 4.8: A 10 d reconstruction of VWC, with (a) sap flow ( $F$ ) and estimated transpiration ( $T$ -cdf). (b) The difference between sap flow and transpiration and (c) the sampled and reconstructed VWC is shown. In between sampling days, VWC estimates are the weighted average between forward and backward reconstructions from the consecutive sampling days (based on the time to the closest sampling day). The measurements which are used to constrain the reconstructed line are accentuated with open markers.

Table 4.6. The regression coefficients suggest that, from all polarizations, VV-pol was most sensitive to internal vegetation water storage and least sensitive to soil moisture. Compared to other polarizations, HH-pol was least sensitive to VWC and SCW and most sensitive to soil moisture. Cross-pol was more sensitive to SCW than the other polarizations. Note that the coefficients from soil and vegetation water stores (Table 4.5) have non-homogeneous physical units. Nonetheless, these coefficients indicate that, for a typical dry day during the campaign of 2018, e.g. 9 June, the soil moisture reduction of  $0.015 \text{ m}^3 \text{ m}^{-3}$  translates to a  $-0.4$ ,  $-0.6$ , and  $-0.6$  dB change in VV-, HH-, and cross-polarized backscatter, respectively. During the same day, VWC changed by  $0.5 \text{ kg m}^{-2}$ , which would translate to a change of 1.5 dB (VV), 1.2 dB (HH) and 1.2 dB (cross). This indicates that, on this typical dry day, a diurnal variation in VWC leads to an almost 4 times higher change in VV-polarized backscatter (dB) than a diurnal change in soil moisture does. On the same day, the changes in HH- and cross-polarized backscatter (dB) were 2 times higher for the diurnal VWC variations than for the soil moisture drydown. The  $0.4 \text{ kg m}^{-2}$  dew formation and dissipation caused  $\sigma^0$  to vary by 0.2 dB (VV), 0.2 dB (HH), and 0.3 dB (cross).

Figure 4.12 presents the results of using the regression coefficients (Table 4.5) and the time series of VWC, SCW, and soil moisture to describe diurnal variations in backscatter. Each day is constrained by the first radar observation of the day at 01:00 LT. Note, from the  $R^2$  values in Table 4.6, that 68%–71% of the variance in backscatter is explained by the three predictors. The  $P$  values for SCW are always higher than those for VWC and soil moisture. Nonetheless, with the exception of the SCW coefficient in the case of HH backscatter ( $P > |t| = 0.286$ ), all  $P$  values are  $< 0.05$ , indicating statistical significance. However, note from Fig. 4.12a and c that the observed nocturnal backscatter

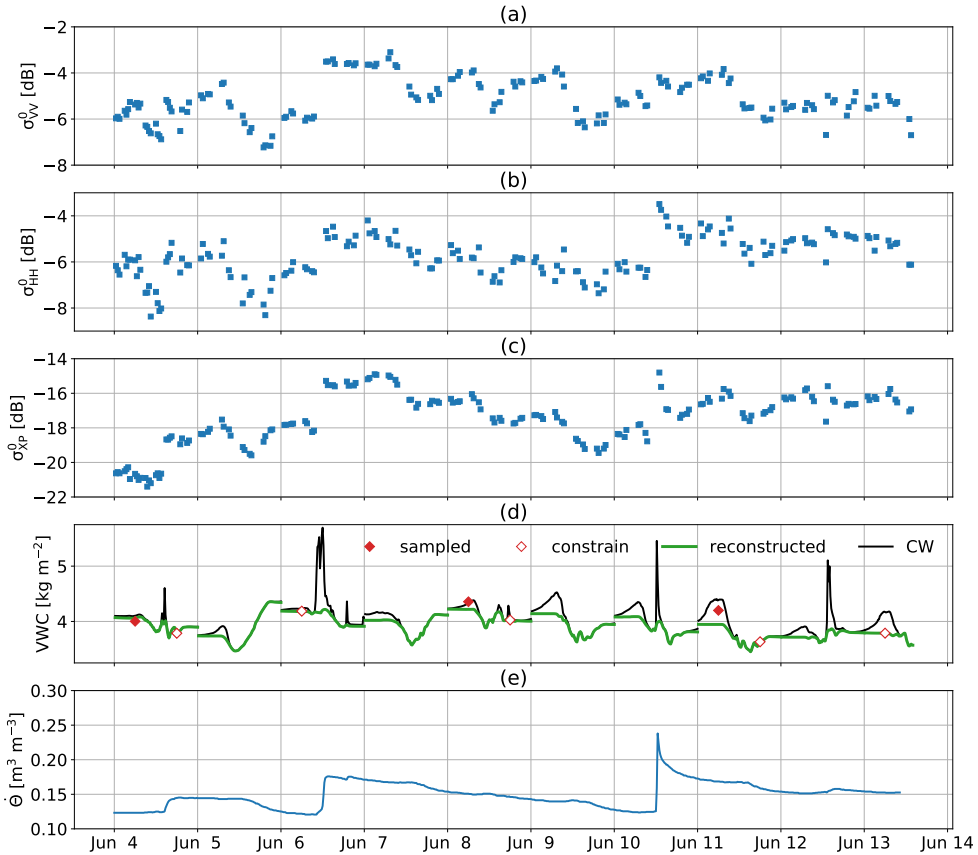


Figure 4.9: Full polarimetric L-band backscatter and separated effects for a 10 d period near the end of the growing season in 2018, with (a) VV-polarized scattering coefficient, (b) HH-polarized scattering coefficient, and (c) averaged VH- and HV-polarized scattering coefficients, (d) sampled and reconstructed VWC, total canopy water, which is the sum of reconstructed VWC and SCW, and (e) soil moisture at 5 cm depth. The measurements which are used to constrain the reconstructed line are accentuated with open markers.

increase as a result of dew formation is barely visible in the calculated backscatter. This suggests that the regression underestimates the effect of dew on backscatter.

## 4.5. DISCUSSION

### 4.5.1. SUB-DAILY VEGETATION WATER CONTENT ESTIMATES: OBSERVATIONS AND RECONSTRUCTIONS

Our results showed that, in non-stressed conditions, VWC depleted by 10%–20% during the day. This internal VWC withdrawal is approximately 10%–20% of the total daily transpiration, which is similar to findings from tropical and temperate broadleaved trees (Köcher et al., 2013; Meinzer et al., 2004). In stressed conditions, we found a 35% drop of VWC during the day.

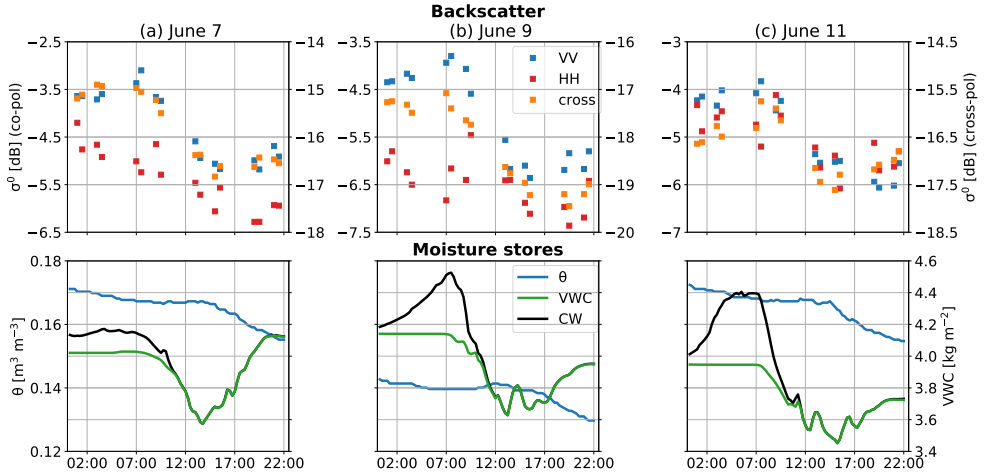


Figure 4.10: Diurnal behaviour of backscatter (VV-, HH-, and cross-pol) and moisture (soil moisture, VWC, and SCW) for 3 individual days without rainfall. These days were selected from the period presented in Fig. 4.9.

Table 4.6: Summary of multiple linear regression results.

|            | VV-pol  |        |        | HH-pol  |        |        | cross-pol |        |        |
|------------|---------|--------|--------|---------|--------|--------|-----------|--------|--------|
|            | VWC     | SCW    |        | VWC     | SCW    |        | VWC       | SCW    |        |
| coeff.     | 24.0643 | 2.9340 | 0.6190 | 39.4680 | 2.2879 | 0.3759 | 38.8273   | 2.4463 | 0.7293 |
| std. err   | 2.600   | 0.262  | 0.302  | 3.019   | 0.304  | 0.350  | 2.906     | 0.293  | 0.337  |
| t          | 9.254   | 11.203 | 2.051  | 13.075  | 7.526  | 1.073  | 13.363    | 8.360  | 2.163  |
| $P >  t $  | 0.000   | 0.000  | 0.043  | 0.000   | 0.000  | 0.286  | 0.000     | 0.000  | 0.033  |
| [0.025     | 18.900  | 2.414  | 0.020  | 33.474  | 1.684  | -0.320 | 33.058    | 1.865  | 0.060  |
| 0.975]     | 29.228  | 3.454  | 1.218  | 45.462  | 2.892  | 1.072  | 44.597    | 3.027  | 1.399  |
| $R^2$      | 0.686   |        |        | 0.690   |        |        | 0.715     |        |        |
| Adj. $R^2$ | 0.675   |        |        | 0.680   |        |        | 0.706     |        |        |

We tested the potential of a non-destructive sap flow approach to estimate sub-daily VWC variations in corn with data from our 2019 campaign. The results confirm the possibility to estimate 15 min variations in corn VWC with only sap flow sensors and a weather station. While the indirect estimation of transpiration could be considered a drawback of the method, Fig. 4.6 has shown that the diurnal VWC cycle was represented generally well. In general, we found the best agreement between reconstructed and sampled VWC when the daily cycle of transpiration was estimated from multi-day sap flow observations and  $ET_0$  estimates. Moreover, the application of CDF matching improved the reconstruction substantially on 25 July, while, on 28 August, a good agreement was already found after linear correction (Fig. 4.6). This difference could partly be explained by the suppressing effect that dew, observed on 25 July (Fig. 4.7), has on transpiration (Dawson and Goldsmith, 2018), which is not captured by  $ET_0$  (Langensiepen et al., 2009). When  $ET_0$  rates are low, estimated transpiration is lower after CDF matching than after



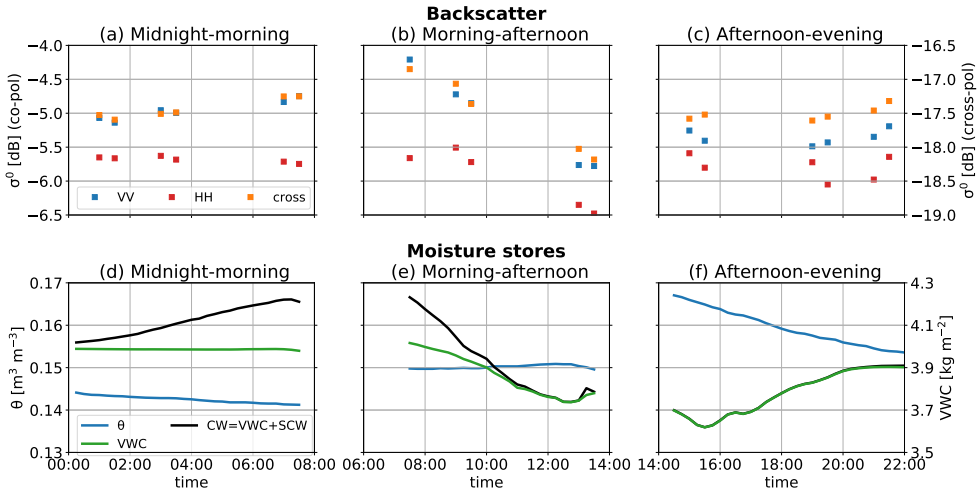


Figure 4.11: Backscatter (VV-, HH-, and cross-pol) and moisture (VWC, CW, and  $\theta$ ) data aggregated across multiple days and separated by part of the day, i.e. midnight–morning, morning–afternoon, and afternoon–midnight. Periods with disturbing rain events are excluded, which means that data in panels (a, d), (b, e), and (c, f) are aggregated across 9, 6, and 4 d, respectively. Canopy water (CW) is SCW displayed on top of VWC.

linear correction (see Fig. 4.4d). Consequently, CDF matching mimicked the suppressing effect of dew due to the reduction in transpiration rates in the morning. When we look at the period between the peak of dew (06:00 LT) and full dissipation (08:15 LT) on 25 July in Fig. 4.6, we see that  $\Delta\text{VWC}$  is  $0.17 \text{ kg m}^{-2}$  in the second row, while  $\Delta\text{VWC}$  is  $0.1 \text{ kg m}^{-2}$  in the third row. This means that CDF matching in this case led to reduction in transpiration of  $0.07 \text{ kg m}^{-2}$ . This is comparable to the estimated dew evaporation in this period, which was  $0.09 \text{ kg m}^{-2}$  (Fig. 4.7). The same holds for 23 August, when we found a transpiration reduction of about  $0.18 \text{ kg m}^{-2}$  between 06:45 and 09:45 LT after CDF matching and an estimated dew evaporation of  $0.20 \text{ kg m}^{-2}$  in the same period. On 28 August, all dew had already dissipated before sunrise and did, thus, not affect transpiration. Therefore, a reduction in transpiration rates did not improve the reconstruction of VWC. These results illustrate that the suppressing effect of dew on transpiration should be taken into account when one estimates transpiration with a weather station or flux tower.

Another effect of CDF matching was that the highest  $\text{ET}_0$  rates resulted in higher estimates of transpiration compared to those obtained using linear corrections (see Fig. 4.4d). This was particularly apparent under sunny conditions such as those on 25 July and 23 August. This means that transpiration rates exceeded sap flow rates for a longer period. Together with the gradual depletion of internal VWC in the morning, this led to a much better agreement and a shift in a diurnal minimum towards the afternoon. However, the poor agreement between the sampled and reconstructed VWC in the evening of 23 August could not be explained by the extreme hydrometeorological conditions, growth stage, or drought stress. Other potential contributors to the poor agreement could be unaccounted for errors in the sap flow, weather data, or samples. The cloudier conditions on 28 August (Fig. 4.7) could explain the small difference between linear cor-

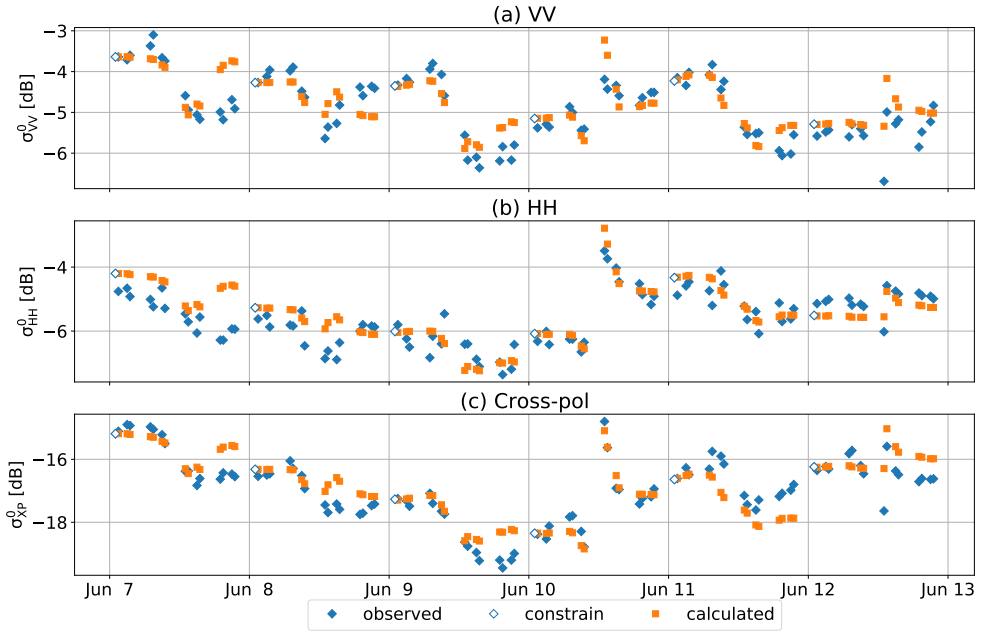


Figure 4.12: Observed and calculated (a) VV-, (b) HH-, and (c) cross-polarized  $\sigma^0$  from 7–13 June 2018. The observations which are used to constrain the predictions of sub-daily  $\sigma^0$  variability,  $\sigma_{t_0}^0$ , are accentuated with open markers. Sub-daily backscatter variation is calculated using Eq. (4.9), the coefficients found by multiple linear regression (Table 4.5), and the time series of VWC, SCW, and soil moisture.

rections and CDF matching.

When the methodology with CDF matching was applied to the 10 d period from our 2018 campaign, the diurnal minima of reconstructed VWC matched excellently with the diurnal minima in the backscatter in most cases (Fig. 4.9). This could be explained by the daily dew formation and high temperatures in this period. However, discontinuities were observed between consecutive days (Fig. 4.8), which might be related to the temporal resolution of the observations and the estimation of transpiration fluxes. The temporal resolution of the sensor observations was 15 min. At the same time, we found phase differences between  $ET_0$  and sap flow of the order of 15–45 min, which was consistent with previous studies on corn (e.g. Langensiepen et al., 2009). Increasing the ratio between phase difference and observation resolution would increase the robustness of the method. A potential solution would therefore be to increase the temporal resolution of the sensor observations. Another potential solution is related to the estimation of transpiration fluxes. Ideally, a flux tower would be used for ET estimates through the eddy covariance method, as it is a more direct measurement and widely considered as the most accurate technique for ET measurements at field scale (Maltese et al., 2018; Oguntunde et al., 2004; Zhang et al., 2014). Improved ET estimates may also reduce or eliminate the need to include CDF matching. As direct ET measurements also include evaporation from SCW and soil, it is advised to include leaf wetness sensors and micro-

lysimeters (Ding et al., 2013) to provide quantitative estimates of evaporation and determine transpiration from ET measurements. Including several in situ sensors of each type (leaf wetness, sap flow, etc.) ensures that the quantities capture field-scale dynamics.

#### 4.5.2. INTERPRETING SUB-DAILY BACKSCATTER

In Vermunt et al., 2020, sub-daily L-band backscatter variations were attributed to VWC, SCW, and soil moisture. However, the lack of sub-daily VWC data points complicated quantifying the relation between backscatter and the individual moisture stores. The VWC records generated in the current study allowed us to understand sub-daily backscatter variations with unprecedented detail and to describe the relative backscatter sensitivity to the different moisture stores.

The results presented here indicate that the effects of sub-daily variations in VWC on backscatter are considerable. Our regression analysis suggested that, on a typical dry day, the diurnal cycle of VWC led to a 2 (HH- and cross-pol) to almost 4 (VV-pol) times higher change in backscatter than the soil moisture drydown did. Note that these ratios can be different when either VWC or soil moisture content substantially change (Brisco et al., 1990) or when the crop structure changes during the day (Kimes and Kirchner, 1983). Backscatter sensitivity to VWC dynamics was most clearly observed in the period between sunrise and mid-afternoon, when both dropped significantly. During mid-afternoon to sunset, we observed a constant to slightly increasing VV- and cross-polarized backscatter, which illustrated the opposite effects of VWC refilling and soil moisture drop on backscatter. Nocturnal backscatter dynamics demonstrated the sensitivity of VV- and cross-pol to SCW.

In general, our results showed that VV-pol was more sensitive to variations in VWC than HH-pol and less sensitive to variations in soil moisture. This is in agreement with Joseph et al., 2010, who described a larger attenuation of the soil return by vegetation for VV-pol compared to HH-pol in a study on the L-band backscattering of corn. An explanation for this difference was given by Stamenković et al., 2015, who described that, at VV and HV polarizations, vertical corn stems attenuate the double-bounce scattering at L-band, which results in lower contribution from the soil. As a consequence, volume scattering and the corresponding contribution from vegetation becomes dominant. At HH-pol, there is less attenuation of the double bounce effect, which explains a higher sensitivity to soil moisture (Table 4.5).

Moreover, the nocturnal VV- and cross-polarized backscatter increase in Figs. 4.9 and 4.11 could be attributed to dew formation only because VWC was stable during the night, and soil moisture was constant or decreased slightly. Stable nocturnal VWC can be expected for crops with a hydraulic capacitance similar to or lower than corn and sufficient soil moisture availability. For vegetation with a larger hydraulic capacitance or low soil moisture availability, nocturnal refilling of VWC could be expected (Maltese et al., 2018), which could complicate the separation of signals from VWC and SCW.

Figures 4.9–4.11 and Table 4.5 showed that, compared to HH-pol, VV- and cross-polarized backscatter were not only more sensitive to changes in VWC but also to changing SCW. This is in agreement with previous findings from Brancato et al., 2017, who found a stronger effect of SCW on S- and C-band differential interferometric observables in VV polarization compared to other polarizations, particularly for vertically oriented

crops as corn. This could be related to increased scattering from wet leaves in combination with the dominance of volume scattering in VV and cross-polarizations. However, it seems that the SCW coefficients ( $c$ ) for VV- and cross-pol in Table 4.5 underestimate the effect of dew on backscatter, as the nocturnal increases in calculated  $\sigma_{VV}^0$  and  $\sigma_{XP}^0$  in Fig. 4.12 are lower than observed. This could partly be addressed by improved SCW estimates, for example, through the inclusion of more leaf wetness sensors distributed in the canopy (Vermunt et al., 2020). Moreover, additional research is needed to provide more insight into the scattering mechanisms under the presence of SCW, for example, by considering SCW in physical backscattering models.

## 4.6. CONCLUSIONS

The potential of using radar for (eco)hydrological studies is limited by the challenge to separate signals from soil and vegetation on a sub-daily timescale. To gain a better understanding of what controls sub-daily backscatter behaviour, we analysed tower-based polarimetric L-band observations from a cornfield using unique estimates of moisture fluctuations in vegetation and soil.

A method developed by the tree physiology community was adapted to estimate continuous variations in corn plant water content with unprecedented detail. The adaptations were related to the estimation of transpiration. The best agreement between sampled and estimated VWC was found when transpiration estimates were obtained after the removal of systematic differences between  $ET_0$  and sap flow. In non-stressed conditions, predawn VWC decreased by 10%–20% during the day.

Complementing the resulting record of VWC with records of soil moisture and previously estimated surface canopy water allowed us to interpret the sub-daily behaviour of polarimetric L-band observations. The results showed a significant effect of diurnal VWC cycles on L-band backscatter when the plants reached their maximum size. The highest and lowest sensitivity to VWC was found in VV- and HH-polarized backscatter, respectively. The regression results suggested that the backscatter behaviour on a typical dry day was 2 (HH- and cross-pol) to 4 (VV) times more determined by the VWC cycle than by soil moisture. Nighttime increases in VV- and cross-polarized backscatter were a result of dew formation only.

The results presented here provide unique insight into the potentially confounding influence of surface and internal vegetation water content variations on backscatter, particularly in the interpretation of sub-daily radar observations. These findings are directly relevant for current and upcoming L-band missions, but also for the design of future spaceborne SAR missions for land applications. In particular, this chapter highlights the potential difference in relative importance of VWC, SCW, or soil moisture dynamics, depending on the overpass time. This is particularly relevant given the imminent availability of sub-daily observations from, e.g., the ICEYE and Capella Space constellations.

As radar observations are increasingly used to study plant water status, the presented sap flow method is a promising way to validate sub-daily satellite observations with just meteorological data and sap flow sensors, without laborious sub-daily destructive sampling. The method is expected to be most robust when the temporal resolution of the sap flow and ET observations are significantly smaller than the phase difference between the two, which depends on the species. The number of sensors required to capture VWC

variations at footprint scale is expected to depend on the footprint size, the spatial heterogeneity of vegetation type, and factors influencing moisture supply and demand. Potentially, global database networks for sap flow measurements, i.e. SAPFLUXNET (<http://sapfluxnet.creaf.cat>, last access: 2 June 2021), and flux tower measurements, e.g. FLUXNET (<https://fluxnet.org/>, last access: 2 June 2021) and AmeriFlux (<https://ameriflux.lbl.gov/>, last access: 2 June 2021), can play an important role here.

Moreover, the utility of the tested sap flow method goes well beyond radar remote sensing. It also has huge potential for validating and interpreting a wide range of other remote sensing techniques that are sensitive to vegetation water, such as passive microwave remote sensing, global navigation satellite systems (GNSSs), and cosmic ray neutron sensors.



# 5

## TOWARDS UNDERSTANDING THE ROLE OF VERTICAL CANOPY MOISTURE DISTRIBUTION ON RADAR BACKSCATTER DYNAMICS

*Chapters 3 and 4 described how continuous estimates of vegetation water content, surface canopy water, and soil moisture from a corn field were used to quantify the effect of their individual variations on L-band backscatter. The analyses improved the interpretation of sub-daily backscatter time series in particular. Another potentially important factor which is poorly understood is the effect of vertical moisture distribution in a canopy on backscatter. This gap in knowledge can cause interpretation errors, and can be a missed opportunity for multi-frequency radars. In this chapter, we present a first step towards understanding the role of time-varying vertical canopy moisture distribution on radar backscatter dynamics. Detailed field measurements were used to establish the vertical distribution of moisture in the canopy layer and its variations during the season, during the day, and under dew and rainfall conditions. Then, these findings were used to define different layers for a multi-layer Water Cloud Model. The model simulations showed the individual layer-contributions to total backscatter.*

---

This chapter is based on:

Vermunt, P. C., S. Khabbazan, S. C. Steele-Dunne, V. Kumar, and J. Judge. Towards Understanding the Role of Dynamic Vertical Canopy Moisture Distribution on Radar Backscatter Dynamics. *Remote Sensing*, under revision.

## 5.1. INTRODUCTION

Multiple experimental studies have demonstrated that radars operating at different frequencies show substantial temporal differences in their backscatter from vegetated land, both on seasonal timescales (Inoue et al., 2002; Y. Kim et al., 2012; Monteith and Ulander, 2018) and sub-daily timescales (Brisco et al., 1990; Monteith and Ulander, 2018). Higher frequencies generally show lower sensitivity to soil moisture under the foliage, because of higher attenuation by the vegetation layer (Bouman and Hoekman, 1993; Ferrazzoli et al., 1992; Narayan et al., 2004). This depends to a great extent on the presence of moisture in the vegetation layer. It has been shown that these frequency-dependent differences in penetration depth could potentially be used to disentangle soil and vegetation contributions to the backscatter signal with multi-frequency radars (Mengen et al., 2021). Moreover, recent studies argue that multi-frequency radars have the potential to be used for determining water content across different heights in the canopy (Konings et al., 2021). However, the link between variations in backscatter and water dynamics in vegetation is still poorly understood.

Much of what we know about scattering from vegetation and how it varies with frequency, polarization and viewing geometry has been obtained by physical forward model simulations. These models are developed to understand the signal received by a sensor, and predict this signal based on a particular set of input parameters. However, widely-used electromagnetic models have not been able to account for a realistic vertical distribution of moisture in vegetation yet. For example, both the Tor Vergata model (Bracaglia et al., 1995) and the MIMICS model (Ulaby et al., 1990) are able to distinguish between leaf and stem water content. Also, some versions of these models divide the vegetation into two layers (Link et al., 2022; Ulaby et al., 1990) to account for different types and densities of scatterers in the sub-layers, e.g. trunk and crown layer. However, a (realistic) vertical distribution of moisture in vegetation has not been introduced. This also holds for the semi-empirical Water Cloud Model (WCM) (Attema and Ulaby, 1978), which assumes that the vegetation layer can be represented as a single cloud with uniform volume scattering and attenuation properties.

Some studies aimed to account for the vertical heterogeneity of moisture in the WCM. A study by Ulaby et al. (Ulaby et al., 1984) for example divided the cloud of a corn canopy into a top layer, containing all the leaves, and a bottom layer, containing the stalks. From their simulations, they concluded that most of the seasonal variations in backscatter from 8.6 - 35.6 GHz frequencies could be explained by variations in leaf area index (LAI) alone. Hoekman (Hoekman, 1987) proposed a multi-layer WCM after he analyzed the effect of height deviations on the pulse returned from a poplar stand. He found substantial differences in backscatter originating from different heights in the canopy. (L. Liu et al., 2012) modified the WCM and included a parameter that describes the moisture distribution between the top-half and bottom-half of a soybean canopy. Their results showed that backscatter simulations were significantly affected by building-in vertical inhomogeneous layers. Although these studies provided useful insights in the importance of vertical inhomogeneity of moisture on scattering, their analyses were limited by the availability of observational data to describe the vertical moisture distribution in a canopy.

Previous studies have demonstrated that the moisture distribution in a corn canopy



is non-uniform and changes during the season (Casanova et al., 2007; Steele-Dunne et al., 2017). Inspired by these findings, the objective of this Chapter was to better understand which parts of the vegetation layer are controlling the backscatter dynamics by accounting for a realistic vertical moisture distribution. We focused on a corn canopy from emergence to harvest, and L-band frequency. Using detailed destructive sampling, we quantified the vertical distribution of moisture in the vegetation and its variations during the season, during the day, and under dew and rainfall conditions. These data were used to define different layers for a multi-layer WCM. The WCM was calibrated using hyper-temporal tower-based polarimetric L-band scatterometer data, and used to quantify the contribution of the individual layers to total backscatter.

## 5.2. MATERIALS AND METHODS

### 5.2.1. EXPERIMENTAL SITES

The measurements for this chapter were mainly conducted as part of our field campaign in Florida, USA, in 2018. The experiments were conducted in Citra (29.410N, 82.179W), at the Plant Science Research and Education Unit (PSREU) of the University of Florida and the Institute of Food and Agricultural Sciences (UF|IFAS). Sweet corn was planted on April 13, and harvested on June 18 for human consumption. We measured vertical profiles of internal VWC throughout the season by destructive sampling (section 5.2.2), and surface canopy water using leaf wetness sensors (section 5.2.2). Moreover, we collected L-band backscatter observations from this field (section 5.2.3).

To determine the extent to which the vertical distribution of VWC changes during the day, we sampled multiple times per day during a follow-up campaign in Reusel (51.319N, 5.173E), the Netherlands in 2019. See Vermunt et al., 2022. In Reusel, the field corn is allowed to ripen in the field, so the growing season extends into September. Details of both experimental sites are given in Table 5.1.

Table 5.1: Details experimental sites

|                  | Citra (2018)               | Reusel (2019)            |
|------------------|----------------------------|--------------------------|
| Type of corn     | sweet corn                 | field corn               |
| Length of season | 66 days                    | 148 days                 |
| Plant density    | 7.9 plants m <sup>-2</sup> | 8 plants m <sup>-2</sup> |
| Peak dry biomass | 0.85 kg m <sup>-2</sup>    | 2.0 kg m <sup>-2</sup>   |
| Peak VWC         | 4.5 kg m <sup>-2</sup>     | 6.4 kg m <sup>-2</sup>   |
| Max. height      | 210 cm                     | 275 cm                   |
| Type of soil     | > 90% sand                 | sandy soil               |
| Climate          | humid subtropical          | temperate maritime       |

### 5.2.2. VERTICAL DISTRIBUTION OF MOISTURE

### INTERNAL VEGETATION WATER CONTENT

Samples were taken from designated sampling areas, just beyond the radar footprint, and fresh ( $m_f$ ) and dry ( $m_d$ ) biomass were determined for each 10cm stem section and each leaf from the same height (see Chapter 2, section 2.2.3). Plant density ( $\rho_{plant}$ ) was used to estimate the field-average VWC per stem section (eq. 5.1).

$$VWC = (m_f - m_d)\rho_{plant} \quad (5.1)$$

Gravimetric water content ( $M_g$ ), which is the mass of water per unit mass of fresh biomass, was calculated by eq. 5.2:

$$M_g = \frac{m_f - m_d}{m_f} \quad (5.2)$$

The same procedure was followed for leaves, tillers, tassels and ears. Because the bottom leaves die and fall off from the stem elongation stage onward, monitored leaf heights were used to ensure a leaf was assigned to the correct label and to ensure consistency through the season. Ears were labelled based on the leaf they were attached to. Tassels and any existing tillers were measured as whole organs.

### SURFACE CANOPY WATER

Dielectric leaf wetness sensors (PHYTOS 31, METER Group) were used to estimate surface water on the canopy (see section 3.2.3 for specifications). Three sensors were installed after plant emergence, mounted to a wooden pole in early season, and attached to plants once the stems were strong enough. Sensor heights were regularly adjusted as the canopy grew to ensure that there was one sensor representing each 1/3 of the plant, and that no sensor was touched by a leaf. We adjusted the angles of the sensors to correspond with the angles of neighbouring leaves. Data from the middle sensor were omitted from this chapter because its performance deteriorated as the season progressed.

It was assumed that the water droplets on other constituents were negligible compared to the water droplets on the leaves. Consequently, quantitative estimations of surface water on the plants were made using the estimated mass of water on the sensor surface [g], calculations of leaf areas ( $A_{leaf}$ ), and distance between leaves and sensors. Leaf areas were estimated by regularly measuring the leaf lengths ( $l$ ) and leaf widths ( $w$ ) of multiple plants, averaging them, and assuming an elliptical shape (eq. 5.3).

The distance between leaf height ( $H_{leaf}$ ) and sensor height ( $H_s$ ) was used to calculate a weighting factor ( $f_w$ ) between 0 and 1 for the lower sensor ( $s1$ ) and the upper sensor ( $s2$ ), see eq. 5.4. This factor is used to determine how much each sensor should contribute to the estimation of leaf surface water (eq. 5.5). The ratio between leaf area and sensor area ( $A_s$ ) was used to convert the mass of water on the sensor ( $M_w$ ) to the mass of water on a leaf. Finally, the resulting mass of water on a leaf [g] was multiplied by the plant density ( $\rho_{plant}$ ) to estimate  $SCW_{leaf}$  in [ $\text{kg m}^{-2}$ ] (eq. 5.5).

$$A_{leaf} = \pi l \frac{w}{4} \quad (5.3)$$

$$f_w(s1) = \begin{cases} 1, & \text{if } H_{leaf} \leq H_{s1} \\ 0, & \text{if } H_{leaf} \geq H_{s2} \\ 1 - \frac{H_{leaf} - H_{s1}}{H_{s2} - H_{s1}}, & \text{if } H_{s1} < H_{leaf} < H_{s2} \end{cases}$$

$$f_w(s2) = 1 - f_w(s1) \quad (5.4)$$

$$SCW_{leaf} = (f_w M_w(s1) \frac{A_{leaf}}{A_s} + f_w M_w(s2) \frac{A_{leaf}}{A_s}) \rho_{plant} \quad (5.5)$$

### 5.2.3. BACKSCATTER DATA

Radar backscatter observations ( $\sigma^0$ ) were made with the University of Florida L-band Automated Radar System (UF-LARS). UF-LARS is a tower-based scatterometer which operates at a centre frequency of 1.25 GHz, and acquires data at four polarization combinations (VV, HH, VH and HV) with a dual polarization horn antenna. The system was mounted on a Genie manlift and lifted to a height of 14m above the ground. From there, the corn field was scanned with a fixed incidence angle of 40°. Further specifications of the UF-LARS system are described in section 2.2.1.

Since VH and HV observations were similar, these were averaged and are referred to here as cross-polarized backscatter ( $\sigma_{XP}^0$ ). There are, on average, 32 acquisitions per day for most of the season. The last eight days of the season, the daily observation frequency was lowered to 16 in order to avoid radio frequency interference with other microwave sensors. The radar footprint was free of human- and material disturbance.

### 5.2.4. WATER CLOUD MODEL

#### ORIGINAL MODEL

The Water Cloud Model (WCM), developed by Attema and Ulaby, 1978, simulates the power backscattered from a vegetated area ( $\sigma^0$ ) as the incoherent sum of the contributions from the vegetation layer and the underlying soil (see equation 5.6). The backscatter contribution from the vegetation layer ( $\sigma_{veg}^0$ ) is simulated using equation 5.7, where W represents the volumetric water content of the vegetation layer, H the height of the vegetation layer,  $\theta_I$  the incidence angle, and C and D are empirically-determined model parameters. In the derivation of this equation, it is assumed that the water in the vegetation layer can be represented as a cloud with identical water droplets, uniformly distributed over the vegetation layer (Attema and Ulaby, 1978).

$$\sigma^0 = \sigma_{veg}^0 + \tau^2 \sigma_{soil}^0 \quad (5.6)$$

$$\sigma_{veg}^0 = C \cos(\theta_I) (1 - \exp(-2DW H / \cos(\theta_I))) \quad (5.7)$$

$$\tau^2 = \exp(-2DW H / \cos(\theta_I)) \quad (5.8)$$

Parameter C is a function of the radar cross section and the total attenuation cross section for one single water particle. Parameter D relates to the total attenuation cross

section for a unit of mass of water. Because all particles are assumed to be identical, parameters C and D are assumed to be frequency-dependent constants.  $W H$  equals VWC [ $\text{kg m}^{-2}$ ]. Since VWC is laborious or difficult to measure, other vegetation descriptors are often used as a substitute, such as vegetation indices from the optical and microwave domain (e.g. El Hajj et al., 2016; J. Li and Wang, 2018).

The potential backscatter from the underlying soil ( $\sigma_{soil}^0$  in equation 5.6), is typically simulated using a simple linear relation between volumetric soil moisture (SSM) backscatter, and empirically found parameters (Khabbazan et al., 2015; Steele-Dunne et al., 2017). Alternatively, a physical model such as the Integral Equation Method (IEM) (Fung, 1994) is used. The extent to which  $\sigma_{soil}^0$  is attenuated by the vegetation is modelled by a factor representing the two-way transmission through the vegetation layer ( $\tau^2$ ), and depends on the VWC (equation 5.8).

### A MULTI-LAYER WCM

The original single-layer WCM does not allow us to consider the sensitivity of total backscatter to contributions from different levels in the canopy. Based on Hoekman (Hoekman, 1987), we built in  $n$  discrete vertical layers in the water cloud and estimated the contribution from each layer to total  $\sigma_{veg}^0$  (see equation 5.9, where index  $n$  refers to the top layer and index 1 refers to the bottom layer). The vegetation scattering from the top layer  $n$ ,  $\sigma_n^0$ , can be estimated using equation 5.7, and replacing  $W H$  by VWC of layer  $n$  only. Each layer below is affected by the attenuation from the layer(s) above, which is estimated by equation 5.10. The number of layers and height of each layer were specified based on the vertical moisture profiles found by destructive sampling (section 5.3.1).

$$\sigma_{veg}^0 = \sigma_n^0 + \tau_n \sigma_{n-1}^0 + \tau_n \tau_{n-1} \sigma_{n-2}^0 + \dots + \tau_n \tau_{n-1} \dots \tau_2 \sigma_1^0 \quad (5.9)$$

$$\tau_i = \exp(-2D VWC_i / \cos(\theta_i)) \quad (5.10)$$

### CALIBRATION AND VALIDATION

The WCM was calibrated for each polarization in order to find parameters C and D. We assumed that the type of scatterers in the various layers are the same, i.e. C and D are identical for each layer. Data inputs for the calibration were the measurements of total plant VWC, backscatter observations ( $\sigma_{obs}^0$ ), and surface soil moisture (SSM). In order to increase the robustness of the calibration, VWC was estimated for the days between sampling days using linear interpolation between the measurements, and included in the data set. To exclude the effect of SCW, we only considered the observation times with negligible SCW. However, the presence of dew was generally at its maximum around predawn sampling times (06:00), which would exclude a lot of data points. From a previous study (Vermunt et al., 2022), we know that predawn VWC (around 6:00) should be more or less stable between 21:00 and 06:00. Therefore, we used the SCW and radar observations between 21:00 and the predawn sampling time with minimal SCW. If the plants were wet the night before due to rainfall, we used the first acquisitions for which dew was (almost) dissipated, around 09:00. This time should be closest to the 6am VWC sample without dew. If both were not an option and the vegetation was wet all the time, we removed the day from the data set. This was the case for five days in May and one

day in June. To reduce the random variability of backscatter observations, backscatter was averaged over 2-4 acquisitions within 1-1.5 hour, depending of the observation frequency. What remained was three time series with 49 observations of  $\sigma_{obs}^0$ , VWC and SSM, from crop emergence until harvest.

For each polarization, two-thirds of each time series was used to calibrate the WCM, and the remaining third was reserved for validation.  $\sigma_{soil}^0$  was found by the Integral Equation Method (IEM) proposed by Fung, 1994. The IEM is a physically based radiative transfer backscattering model which provides site-independent relationships between backscatter and soil moisture. Moreover, it covers the range of surface roughness values encountered with agricultural soils. The input parameters for the IEM were the frequency, incidence angle and polarization (section 5.2.3), surface roughness parameters defined as the standard deviation of the surface heights and the surface correlation length (Vermunt et al., 2020), the exponential autocorrelation function, and the dielectric constant of the soil media, which is calculated using SSM measurements and Mironov's soil dielectric model (Mironov et al., 2004). Footprint-averaged SSM was estimated using two calibrated EC-5 sensors installed at 5 cm depth and 40 m apart (see Chapter 2).

Finally, the time series of  $\sigma_{obs}^0$ ,  $\sigma_{soil}^0$  and VWC were used to calibrate parameters C and D using equations 5.6-5.8. C and D were optimized by maximizing the Kling-Gupta Efficiency (KGE; Gupta et al., 2009), see equation 5.11 .

$$KGE = 1 - \sqrt{(r-1)^2 + (\alpha-1)^2 + (\beta-1)^2} \quad (5.11)$$

where  $r$  is the linear correlation coefficient (Pearson  $R$ ) between simulated and observed  $\sigma^0$ ,  $\alpha$  is the ratio between the standard deviations of simulated and observed  $\sigma^0$ , i.e. a measure of the relative variability in the simulated and observed values, and  $\beta$  is the ratio between the mean simulated and mean observed  $\sigma^0$ , i.e. the bias (Gupta et al., 2009). KGE is a measure for the goodness-of-fit, with KGE=1 indicating perfect agreement between simulations and observations, and is used in previous studies for calibrating the WCM as well (Modanesi et al., 2021).

For cross-pol, a two-step optimization was necessary to avoid unrealistic values of D due to the limited sensitivity of total backscatter to D. A sensitivity analysis showed that when VWC is at its seasonal maximum ( $\sim 4 \text{ kg m}^{-2}$ ),  $\sigma_{sim}^0$  is mainly determined by parameter C once  $D > 0.1$ . For that reason, the first step was to optimize parameter C for the period between May 25 and June 13, assuming  $D=0.2$ . Then, this fixed value for C was used to optimize parameter D for the entire data set.

The performance of the calibration was evaluated by first simulating  $\sigma_{sim}^0$  for the validation data using the calibrated C and D parameters, and then calculating the Root Mean Squared Error (RMSE) between  $\sigma_{sim}^0$  and  $\sigma_{obs}^0$ .

## 5.3. RESULTS AND DISCUSSION

### 5.3.1. SEASONAL CHANGES OF INTERNAL VEGETATION WATER DISTRIBUTION

Figure 5.1 shows the vertical distribution of VWC (a,c,e,g) and  $M_g$  (b,d,f,h) for the different plant constituents, and their development during the season. The distribution of

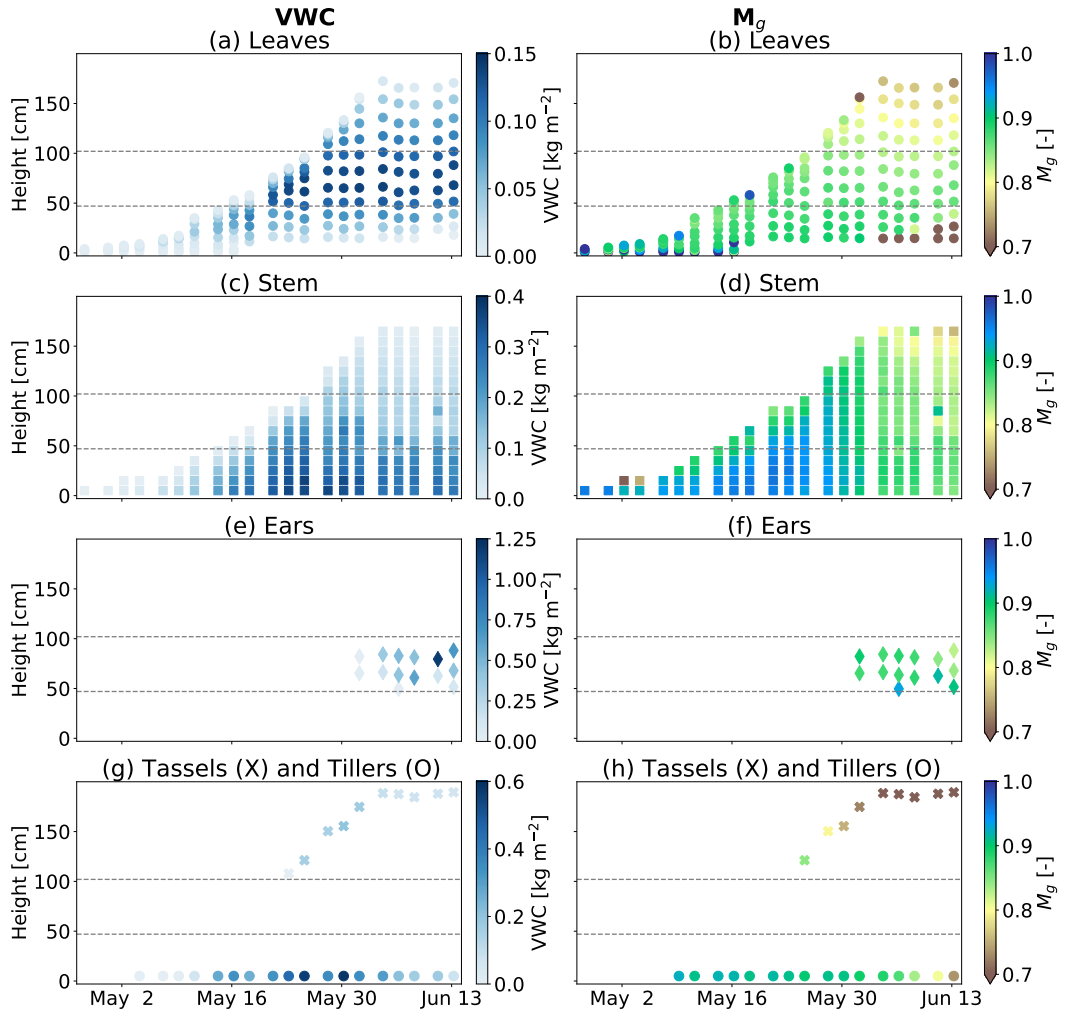


Figure 5.1: Vertical VWC (left) and  $M_g$  (right) profiles and their seasonal changes for sweet corn, with leaves (a,b), stems (c,d), ears (e,f), tillers (g), and tassels (g,h). Each marker is the average of 8 plants. Note that the VWC-axes are different among the constituents. The horizontal dashed lines represent the separation of layers for the Water Cloud Model.

VWC is first of all determined by the plant's structure. Stem water content is for example concentrated in the lowest and thickest part of the stem. The first 50 cm of the stems contained 100% (early season) to 60% (late season) of total stem VWC. The four biggest leaves, located between 50 and 100 cm, contained 60% of total leaf VWC in mid- to late season. Attached to these big leaves are the ears, which stored up to 25% of total plant VWC in the late season.

Also the aging of the plants has an important effect on the distribution of moisture. The  $M_g$  in most of the plant tissue slowly decreases after the first emergence of tassels

(May 25), and this drop accelerates after the emergence of ears (June 1; Fig. 5.1(b,d,f,h)). Leaf senescence starts when the ears separate from the stem (June 4). It starts from the ground up with the lowest leaves, followed by the top leaves from which it progresses down. The largest leaves in the middle of the plant dry out last. Simultaneously, the upper stem dries out. Because this senescence does not occur simultaneously across the vertical profile, variation in moisture across the profile increases from mid- to late season.

Finally, a plant's moisture content is determined by external factors, such as availability of root zone soil moisture and evaporative demand of the atmosphere, in combination with the hydraulic strategy of the plant. For our corn plants, the effect of these external factors was mainly visible on a sub-daily timescale (see section 5.3.2).

Roughly, we can divide the canopy into three vertical layers, marked with horizontal dashed lines in Fig. 5.1, and further visualized in Fig. 5.2. The lowest layer, hereafter referred to as layer 1, contains the entire plant in the early season. During the mid and late season, 60 to 90% of the VWC in the lower layer is stem water, respectively. The amount of water the tillers contained is significant in the mid-season, with 20-25% of total plant VWC in this layer. Compared to the other two layers, layer 1 contains most water until June 4 (Fig. 5.2(b)).

Layer 2 contains the 4 biggest leaves, the ears, and 50 cm of stem in mid- to late season (Fig. 5.2). The leaf water content in this layer is relatively stable between May 21 and June 13 and is about  $0.5 \text{ kg m}^{-2}$ . The relative contributions to total VWC in layer 2 change from 70% leaf and 30% stem on May 18 to 40% leaf and 60% stem on May 28, just before ear formation, to 25% leaf, 25% stem, and 50% ear on June 13. From June 4 onward, layer 2 contains most water (Fig. 5.2(b)).

The upper layer, layer 3, is up to twice as thick as the lower layers and has the lowest water content (Fig. 5.2). It contains the tassels, four leaves and the thinnest part of the stem. Once the layer water content reaches its peak on May 30, it stays relatively constant (Fig. 5.2(b)). Despite the decrease of their  $M_g$ , leaf and stem VWC remains  $0.2$  and  $0.3 \text{ kg m}^{-2}$ , respectively. This can be explained by the growth of the leaves and stems in this layer, and the distribution of water over increasing biomass. Tassel VWC decreased from  $0.15 \text{ kg m}^{-2}$  on May 25 to  $0.06 \text{ kg m}^{-2}$  on June 13.

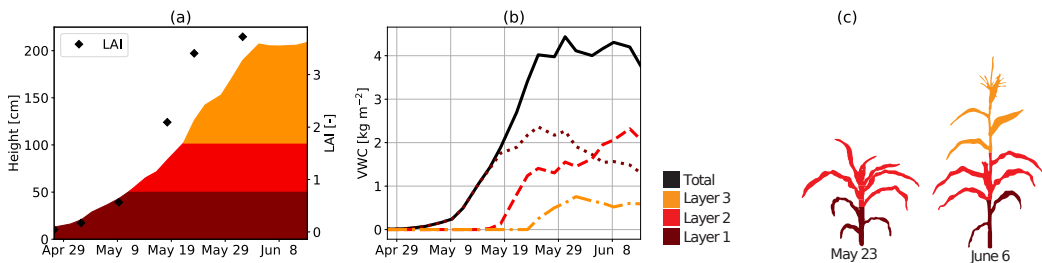


Figure 5.2: Canopy height divided into three layers including LAI (a), total plant VWC divided into three layers (b), and visualisations of the layer division in two different growth stages (c).

5.3.2. SUB-DAILY CHANGES OF INTERNAL VEGETATION WATER DISTRIBUTION

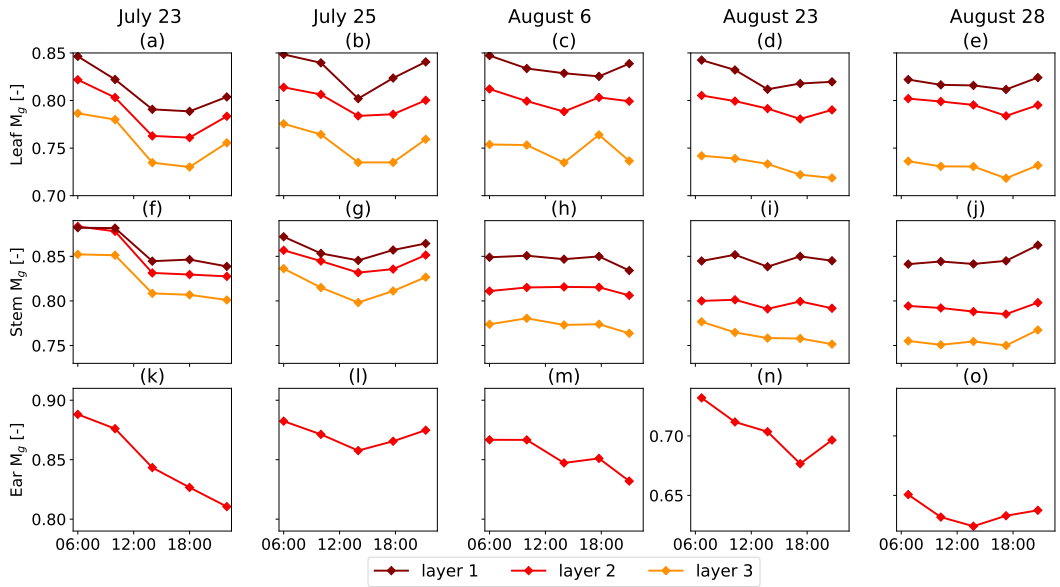


Figure 5.3: Five days of diurnal leaf, stem and ear  $M_g$  variations in field corn, and the difference between the three vertical layers in the canopy. The sampling was performed five times between sunrise and sunset in the 2019 campaign.

The architecture of a plant also plays a role when it comes to diurnal variations in moisture distribution. It determines which leaves are more or less exposed to solar radiation and wind, the temperature gradient within the canopy, and consequently the extent to which the leaves participate in photosynthesis and transpire water (Banerjee and Linn, 2018). The diurnal patterns in Figures 5.3 and 5.4 are the results of sub-daily destructive sampling from field corn in our 2019-campaign in the Netherlands. Figure 5.3 shows a slightly larger diurnal variability in leaf (a-e) and stem  $M_g$  (f-j) in layer 3 on most days, which confirms the role of architecture. However, differences between the layers are minor. Moreover, Fig. 5.4(p-t) shows that the diurnal variations in layer 3 are limited, and that most of the diurnal variation is in the lower two layers.

External factors, such as soil moisture availability and evaporative demand also affect the diurnal variability of VWC. On July 23, we observed leaf 'rolling', a mechanism for drought stressed corn plants to reduce the leaf area exposed for transpiration (Vermunt et al., 2022). In Fig. 5.3(a,f,k) we see that for this day, per constituent, the diurnal  $M_g$  pattern of all layers is similar in response to the water deficit. However, leaves, stems and ears respond differently. Where leaves recharge in the evening (a), the water content in the stems stays more or less constant (f), and ear water content still drops (k). From the VWC cycles of July 23 (Fig. 5.4(a,f,k)), we see that stem VWC dominated layer 1, and, to a lesser extent, also layer 2. The diurnal VWC patterns of layer 1 and 2 are therefore similar (Fig. 5.4(p)).



Also in these field corn plants, we observed a shift in the contribution of the lower two layers to total plant VWC. In July, the diurnal cycles in layer 2 were still dominated by stems and leaves (Fig. 5.4). VWC in layer 2 was lower than (July 23) or equal to (July 25) VWC in layer 1. Layer 2 became the dominant VWC-layer with further ear development in August. Then, the ears determined the shape of the diurnal VWC cycle in layer 2 to a great extent.

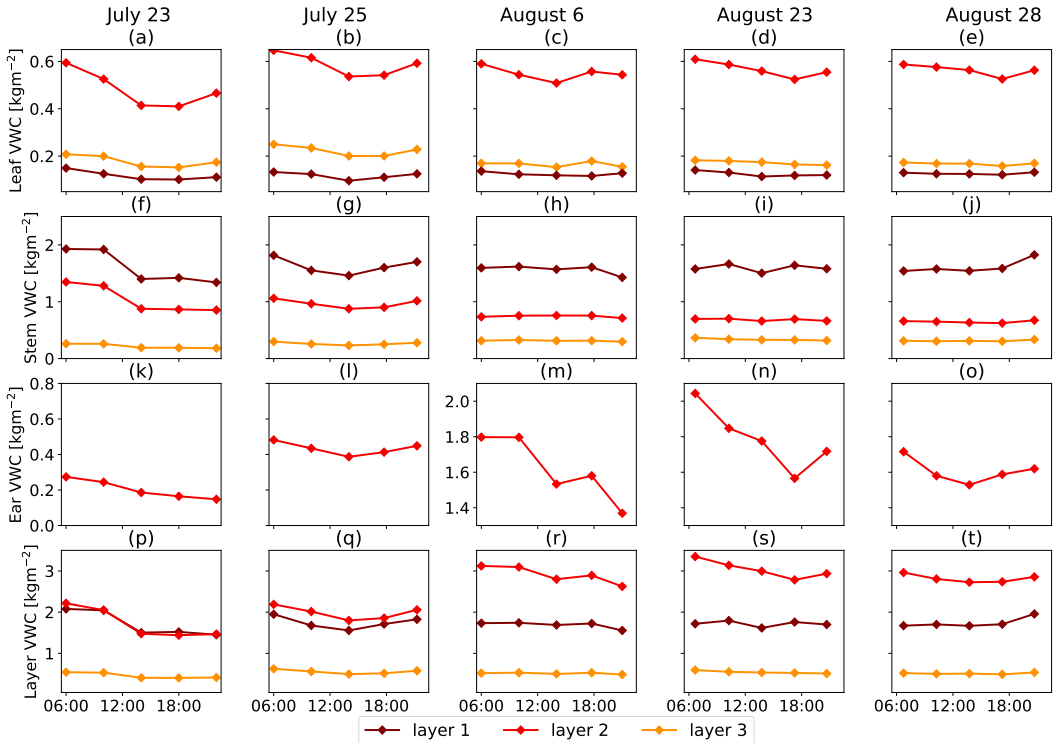


Figure 5.4: Five days of diurnal leaf, stem, ear and layer VWC variations in field corn [ $\text{kg m}^{-2}$ ], and the difference between the three vertical layers in the canopy. Layer VWC is the sum of the moisture in all constituents within a certain layer. The sampling was performed five times between sunrise and sunset in the 2019 campaign.

### 5.3.3. DISTRIBUTION OF SURFACE WATER: DEW AND RAINFALL INTERCEPTION

Figure 5.5(a) shows the difference between the mass of dew detected by the upper and lower sensor. The peak from the upper sensor is 4 times higher than the peak from the lower sensor. This suggests that the most dominant origin of the condensed water vapour was the atmosphere, i.e. dewfall. Using the vertical distribution of leaf area (Fig. 5.5(b)), dew profiles were estimated (Fig. 5.5(c)). These profiles show considerable similarities with dew profiles in corn plants found by previous experimental studies (Atzema et al., 1990; Jacobs et al., 1990). In their 16-nights study on the origin of dew in a corn

canopy, Atzema et al., 1990 found that 95% of the measured dew could be attributed to dewfall and only 5% to dewrise, which is the upward soil water vapour flux into the atmosphere during the night. This difference was explained by the fact that a tall and dense crop reduces the amplitude of the daily temperature wave in the non-saturated soil, and therefore reduces the dewrise. However, in case of a well-watered soil and a stable atmosphere above the canopy, dewrise will increase as a result of the unstable air between the cooling upper canopy and the heat supply from the soil (Atzema et al., 1990; Jacobs et al., 1990; Kabela et al., 2009).

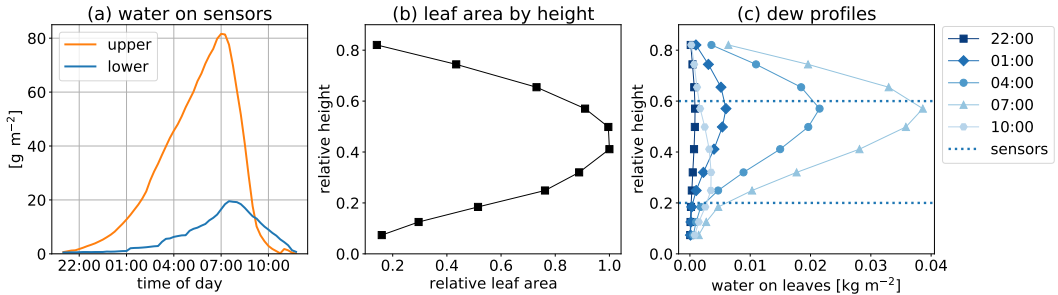


Figure 5.5: Vertical distribution of dew, with (a) water detected on upper and lower sensor [ $\text{g m}^{-2}$ ] during dew accumulation and dissipation, averaged over 14 dew events, (b) averaged vertical profiles of leaf area for mid-to-late season, with leaf area relative to maximum leaf area and height relative to maximum plant height, and (c) resulting vertical dew profiles changing during the night, including relative heights of sensors.

Unlike dew, both sensors detected similar amounts of water during rainfall (Fig. 5.6). This suggests that raindrops penetrated the entire canopy, even during light rain events. The distribution of raindrops through the cascade system of the foliage is a complex process, depending on form, texture and angle of the surface, canopy architecture and density, and number of layers in the cascade (Frasson and Krajewski, 2013; Parker, 1995). However, given the minor differences between the sensor outputs, our estimated interception profiles (Fig. 5.6(c)) strongly reflect the vertical distribution of leaf area (Fig. 5.5(b)).

### 5.3.4. MULTI-LAYER WCM: SEASONAL VARIATIONS

Table 5.2 shows the WCM calibration results, including the RMSEs between observations and simulations.

Table 5.2: WCM calibration results

| C    |      |       | D    |      |      | RMSE [dB] |      |      |
|------|------|-------|------|------|------|-----------|------|------|
| VV   | HH   | XP    | VV   | HH   | XP   | VV        | HH   | XP   |
| 0.51 | 0.39 | 0.026 | 0.14 | 0.20 | 0.13 | 1.22      | 1.28 | 1.24 |

Figure 5.7 shows the results from the 3-layer WCM, and the observed L-band backscatter ( $\sigma_{obs}^0$ ) for VV (a), HH (b), and cross-pol (c). The contribution from the different layers to total  $\sigma_{veg}^0$  changes during the season. In early season,  $\sigma_{veg}^0$  equals the contribution

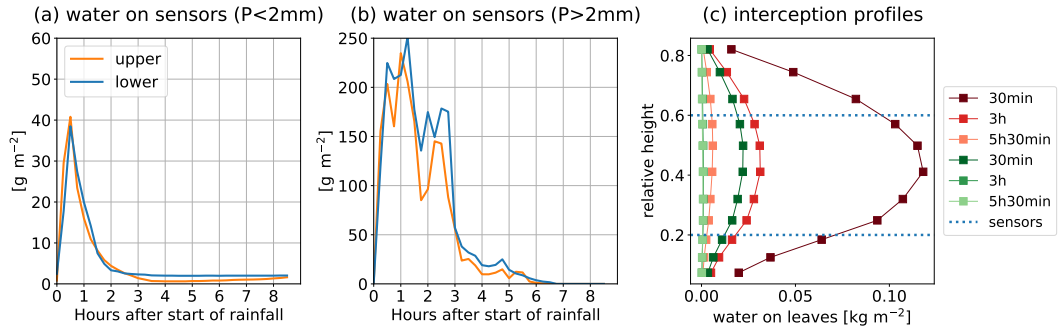


Figure 5.6: Vertical distribution of rainfall interception, with the averaged mass of water detected on upper and lower sensor [ $\text{g m}^{-2}$ ] during (a) 6 light rain events ( $P < 2\text{mm}$ ), and (b) 4 heavy rain events ( $P > 2\text{mm}$ ), in the period between June 1 and June 13, and (c) the resulting vertical interception profiles changing during light (green) and heavy (red) rain events, including relative heights of sensors. Note that the data is aggregated. Nocturnal rain events tend to lead to longer periods of canopy wetness, while rainfall interception during the day tends to evaporate rapidly.

from the lowest layer,  $\sigma_{veg,L1}^0 \cdot \sigma_{veg,L1}^0$  decreases with increasing vegetation growth above this layer. Rapid accumulation of VWC in layer 2 (Fig. 5.2) resulted in a dominant contribution from layer 2 when  $\text{VWC} > 1 \text{ kg m}^{-2}$  (from May 23 onward; Fig. 5.2(b) and Fig. 5.7), in all polarizations. The simulations showed similar sensitivity of  $\sigma_{veg}^0$  to layers 1 (lowest 50 cm) and 3 (upper 100 cm) for VV-pol and cross-pol in the last two weeks of the season. In HH-pol, layer 3 is more dominant in this phase than layer 1. Finally, the simulations showed negligible sensitivity to the attenuated soil moisture signal ( $\sigma_{soil}^0 \tau^2$ ) for co-pols (from  $\text{VWC} > 1 \text{ kg m}^{-2}$  onward) and cross-pol (from  $\text{VWC} > 0.5 \text{ kg m}^{-2}$  onward).

Fig. 5.8 shows the simulated transmissivity ( $\tau$ ) decreasing over time and depth in the vegetation layer. The transmissivity in VV-pol (a) and cross-pol (c) is largely similar. For HH-pol, the model found lower transmissivity (and thus higher attenuation). Transmissivity is directly related to Vegetation Optical Depth (VOD; Frappart et al., 2020). Consequently, Fig. 5.8 shows that dynamics in a VOD estimate would largely be due to dynamics in layer 1 in the early season and in layer 2 in the late season. This demonstrates the potential value for a multi-layer WCM to interpret VOD estimates.

So far, little research has been conducted on the relative importance of different vertical layers on the backscatter signal. However, we could compare the findings of our modelling study with the results from a recent tomography study by Joerg et al., 2018 on field corn. They estimated 3-D backscatter profiles from field corn for VV, HH and HV at different frequencies, including L-band, for two growth stages: (1) just before fruit development and (2) just after fruit development. In our modelling study, we found that the VV and XP scattering contributions from layers 1 and 2 are equally dominant just before fruit development (around May 29), and more dominant than scattering from layer 3 (Figure 5.7). In HH-pol, scattering from layer 2 was already most dominant. At this stage, model simulations showed negligible scattering from the ground. Joerg et al., 2018 found that, at this stage, the maximum scattering in all polarizations is centred at ground-level, despite a plant height of 1.9 m. This means scattering from the lowest

vegetation layer and the ground. After fruit development (around June 13), we found dominant scattering from layer 2 in all polarizations. Joerg et al., 2018 found that, at this stage, the maximum return in L-band VV-pol came from scattering at 1/2 to 1/3 of the crop height, which would also be equivalent to layer 2. In addition, they found that the maximum return in HH-pol and HV-pol came from scattering at about 1/4 of the crop height, which would be equivalent to the boundary between layers 1 and 2. This is lower than at VV-pol, and also slightly lower than our modelling results.

Compared to previous findings (Vermunt et al., 2022), simulations from the WCM used here underestimate the sensitivity to surface soil moisture in the mid- and late season. An important explanation could be that vegetation-ground interactions are not included in the WCM. Previous studies have shown that this term could be considered an important scattering mechanism in corn (e.g. Chauhan et al., 1994; Monsivais-Huertero and Judge, 2011). It is expected that considering a vegetation-ground scattering term would increase the sensitivity to surface soil moisture, and also might influence the attenuation from the vegetation layer simulated by the WCM.

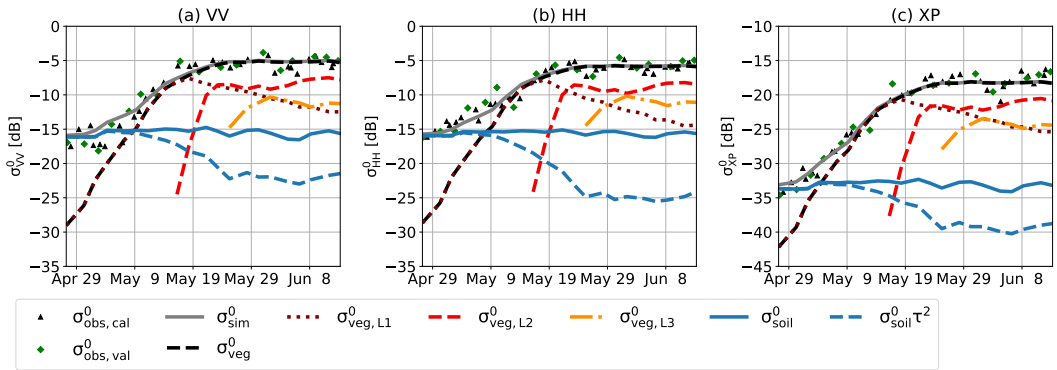


Figure 5.7: Seasonal variations in the contributions of the three different vegetation layers to total vegetation scattering ( $\sigma_{veg}^0$ ), simulated by the 3-layer Water Cloud Model. The different polarizations are separated in (a) VV, (b) HH, and (c) XP.

### 5.3.5. MULTI-LAYER WCM: SUB-DAILY VARIATIONS

The effect of free SCW on variations in layer contributions to  $\sigma^0$  was estimated by treating SCW as part of the water cloud. In other words, the SCW in a given layer, shown in Fig. 5.9(a) and 5.10(a), is added to the internal VWC of this layer. The VWC is assumed to be constant in each layer for the model simulations, to isolate the effect of SCW. For simplicity, we assumed that parameters C and D, which were calibrated for dry situations, are also valid in these wet situations, and that any geometry-related effect accounted for in C and D remains the same regardless of whether the water is VWC or SCW.

Fig. 5.9 and 5.10 show the effects of dew and rainfall interception on the variations in layer contributions to  $\sigma^0$ , respectively. Observed  $\sigma^0$  from dew events could be aggregated and was added to the figure. This was not possible for  $\sigma^0$  from interception events due to the difference in backscatter acquisition timing since the start of the events. From

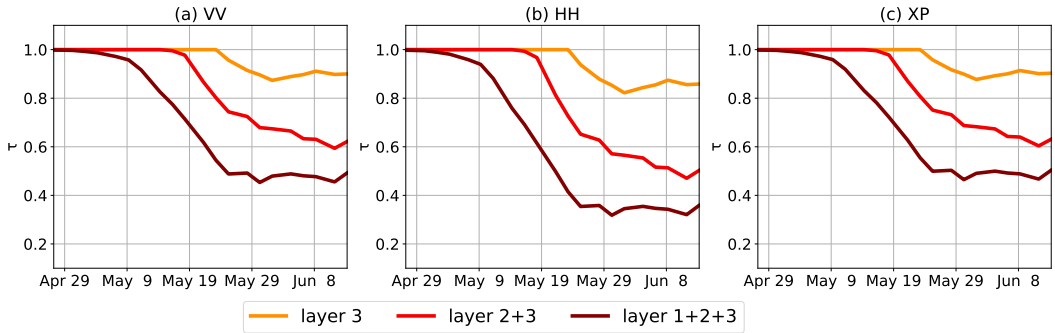


Figure 5.8: Seasonal variations in the transmissivity ( $\tau$ ) at different depths of the vegetation layer, simulated by the 3-layer Water Cloud Model. The different polarizations are separated in (a) VV, (b) HH, and (c) XP.

Fig. 5.9(a), it can be seen that nocturnal dew accumulation mainly occurs in layers 2 and 3. When using these estimates as inputs for the WCM, a significant increase in backscatter from layer 3 was found. However, scattering from layer 2 was almost constant, or even had a counterbalancing effect (HH) on  $\sigma^0$ . The latter also holds for layer 1 in all polarizations. The effect of all layers combined was a simulated  $\sigma^0$  variation of 0.15 dB (VV), 0.10 dB (HH) and 0.16 dB (cross-pol). The fact that dew affects cross-pol and VV-pol more than HH-pol  $\sigma^0$  is consistent with the observations and previous findings (Vermunt et al., 2022). Both VV- (b) and cross-pol (d)  $\sigma_{obs}^0$  show a gradual increase corresponding to dew accumulation, and a sharp drop corresponding to dew dissipation. This behaviour was not observed in HH-pol (c). However, the amplitude of the simulated nocturnal ‘cycle’ is much smaller than what is observed in VV-pol and cross-pol. For rainfall interception, we found similar dynamics, except that there was simply more surface water from interception, particularly in layer 2. As a consequence, backscattering from layer 2 had a stronger effect on variation in  $\sigma_{sim}^0$ , which was 0.3 dB (VV), 0.2 dB (HH), and 0.3 dB (XP).

Fig. 5.11(a) shows the layer contribution to diurnal VWC variation for July 25, 2019. It can be seen from (b) and (c) that,  $\sigma^0$  is dominated by scattering from layer 2 in all polarizations, with also significant contributions from layers 1 and 3. Simulated  $\sigma^0$  varied with 0.38 dB (VV), 0.25 dB (HH) and 0.40 dB (XP). However results from Vermunt et al., 2022 suggest that diurnal variations in  $\sigma^0$  should be in the order of 2 dB, as a result of these changes in VWC. Together with differences between observed and simulated  $\sigma^0$  during dew events (Fig. 5.9), this suggests that sub-daily variations in the WCM simulations are highly underestimated. This is further illustrated in Figure 5.12. This figure shows the observed and simulated backscatter variations in the last six days of the season. Sub-daily VWC is based on Vermunt et al., 2022. The sum of SCW and VWC was considered the moisture input for the WCM. Since the difference between simulated  $\sigma^0$  and  $\sigma_{veg}^0$  was negligible at this stage, only  $\sigma_{veg}^0$  is depicted. From the analysis in three previous studies (Khabbazan et al., 2022; Vermunt et al., 2020; Vermunt et al., 2022), we found that variations in VWC, SCW and soil moisture affected  $\sigma^0$  significantly at this stage of the season.

Here, ignoring the vegetation-ground scattering term in the WCM could also play a role. Moreover, high attenuation prevents sub-daily backscattering variations to be captured, which becomes for example apparent from the difference in backscatter contributions from layers 2 and 3 in Fig. 5.9. Comparable amounts of dew were added to layers 2 and 3, but because of much higher attenuation in layer 2 (see Fig. 5.8), we found no nocturnal cycle of  $\sigma_{veg,L2}^0$  compared to a strong nocturnal cycle of  $\sigma_{veg,L3}^0$ . It could be that the WCM simulations overestimated attenuation by the vegetation layer.

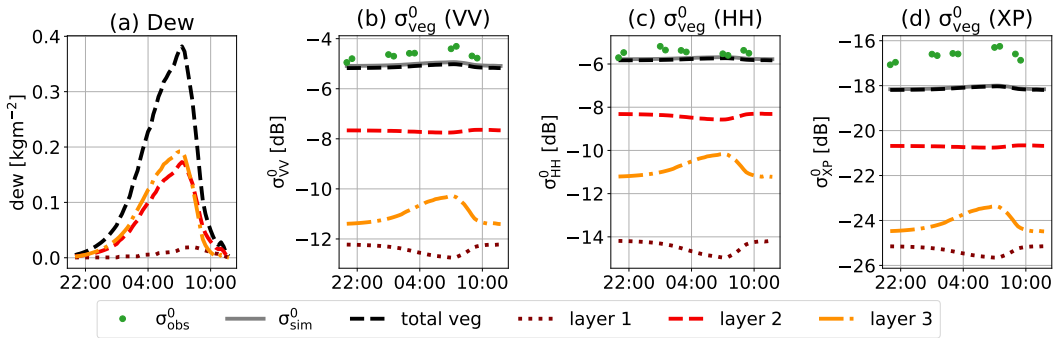


Figure 5.9: Averaged dew estimates from 2018 separated by layer (a), and the corresponding nocturnal variations in the layer contributions to total vegetation scattering ( $\sigma_{veg}^0$ ), simulated by the Water Cloud Model and separated by VV (b), HH (c) and cross-polarization (d).

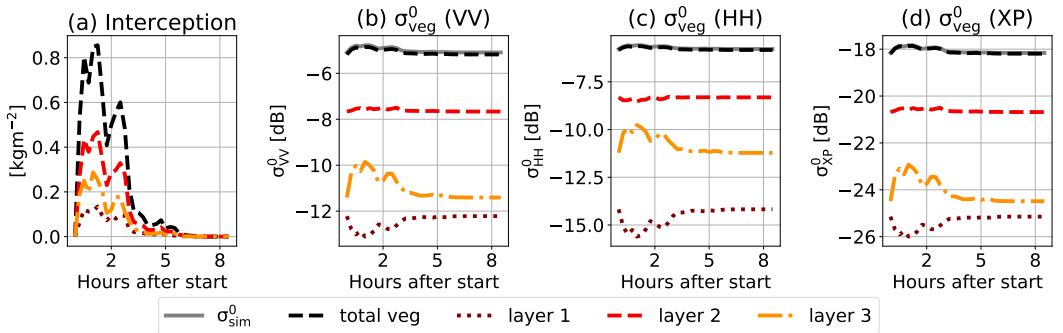


Figure 5.10: Averaged heavy rainfall interception estimates from 2018 separated by layer (a), and the corresponding variations in the layer contributions to total vegetation scattering ( $\sigma_{veg}^0$ ), simulated by the Water Cloud Model and separated by VV (b), HH (c) and cross-polarization (d).

## 5.4. CONCLUSIONS

The aim of this chapter was to better understand which parts of the vegetation layer control the L-band backscatter dynamics from a corn canopy. Destructive sampling and sensor-based measurements were conducted to illustrate the dynamic vertical distribution of both internal and surface canopy water, respectively, throughout the season. This

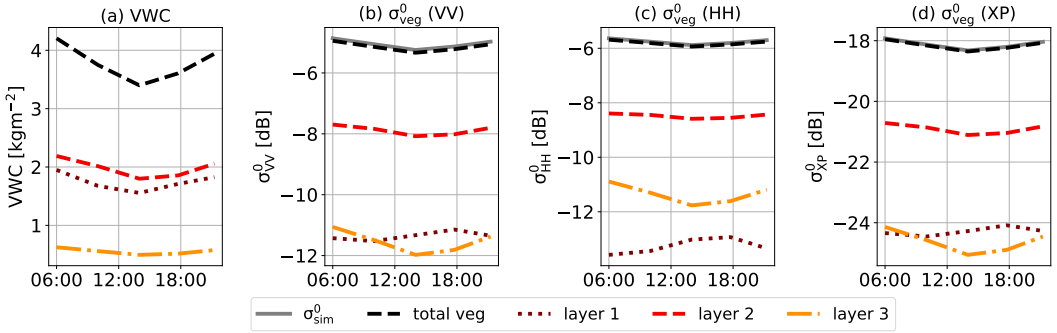


Figure 5.11: Diurnal WVC estimates for July 25 (2019) separated by layer (a), and the corresponding diurnal variations in the layer contributions to total vegetation scattering ( $\sigma_{veg}^0$ ), simulated by the Water Cloud Model and separated by VV (b), HH (c) and cross-polarization (d).

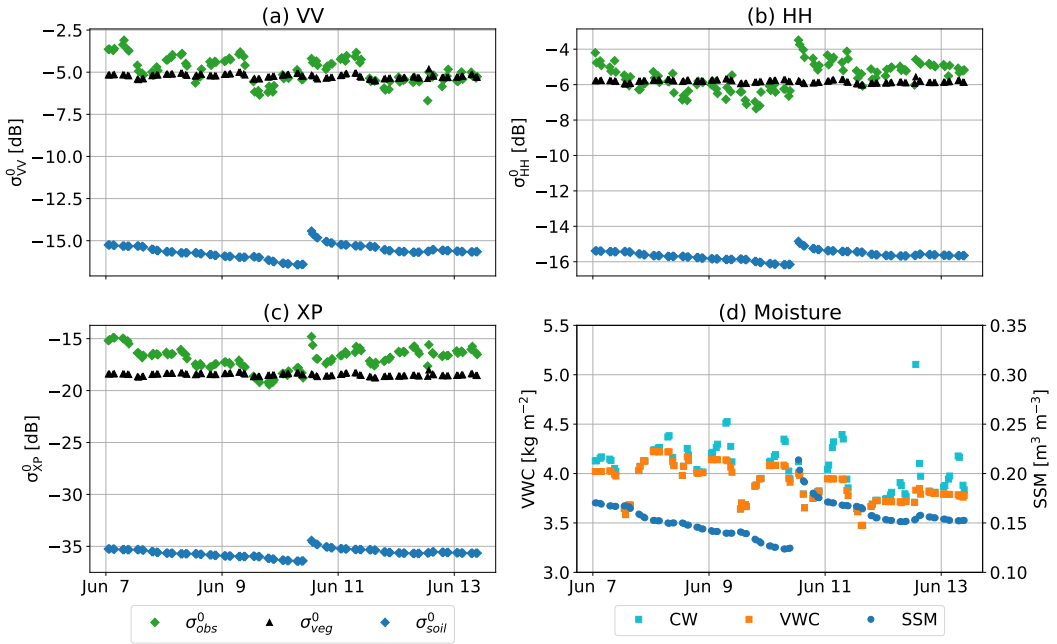


Figure 5.12: Six-day time series with observed backscatter ( $\sigma_{obs}^0$ ), simulated  $\sigma_{veg}^0$  from the WCM, and simulated  $\sigma_{soil}^0$  from the IEM, for VV (a), HH (b), and cross-pol (c). Moisture variations which served as inputs for the models are shown in (d), with surface soil moisture (SSM) as input for the IEM, VWC and CW, which is the VWC supplemented with dew or rainfall interception, and is used as input for the WCM. Sub-daily VWC variations are based on Vermunt et al., 2022

information was used to define three layers for a multi-layer WCM, and simulate the individual layer-contributions to total backscatter.

We found that the vertical moisture distribution of VWC is highly dynamic in time.

Seasonal changes were mainly affected by the plant's architecture and age, diurnal changes were mainly affected by moisture demand and availability. Diurnal dynamics in gravimetric water content were similar across different heights in the canopy. However, the lower parts of the stem and the biggest leaves governed the diurnal VWC cycle, together with the ears from mid-season onward. Dew was mainly found in the upper and middle part of the canopy, while rainfall penetrated the entire canopy.

This heterogeneity in moisture distribution means that the contribution of the different vertical layers to total  $\sigma_{veg}^0$  varies during the season. Water Cloud Model simulations showed maximum scattering from the layer with the biggest leaves and the ears in mid-to-late season. The contribution to  $\sigma^0$  from the lowest 50 cm, which contains most water and mainly from stems, was comparable to the contribution from the top 100 cm for VV- and cross-pol in this phase of the season. HH-pol simulations found more sensitivity to the top 100 cm than to the lowest 50 cm due to slightly higher attenuation. On a sub-daily timescale, variations in  $\sigma^0$  are sensitive to different parts of the canopy, depending on whether they are caused by dew, interception or fluctuations in VWC. However, variations simulated  $\sigma^0$  are highly underestimated. This may be explained by overestimated attenuation of the vegetation layers by the WCM, or by the importance of the missing vegetation-ground scattering term. It is essential for subsequent studies to understand this issue, because of the implications this has on the simulated contributions from the different layers on total backscatter.

This study provides new and unique insights into the contribution of different 'depths' in a canopy on radar backscatter. Modelling studies, together with other techniques such as tomography, can provide useful insights into the sensitivity of  $\sigma^0$  to scattering from distinct vertical levels. Our results demonstrate the potential importance of accounting for the vertical moisture distribution when understanding and interpreting backscatter dynamics or products such as vegetation optical depth (VOD).

An important task for future research is to modify the WCM, or other electromagnetic models, in such a way that they are able to capture sub-daily backscatter dynamics. It is expected that this will improve the estimates of layer contributions to total backscatter. Also considering ground-vegetation scattering should improve the simulated contributions from the different layers. Moreover, future research should focus on the scattering mechanisms related to surface canopy water. The interactions between microwaves with free water on the canopy surfaces (dew, rainfall interception) are still poorly understood.

To properly understand the potential of using multiple frequencies to determine water content across different heights, it is advised to repeat this experiment with a multi-frequency radar. Also shifting the type of vegetation to trees could be interesting. Backscattering from different levels in the canopy may be even more relevant in complex forest systems. A challenge for future research is to understand the backscatter dependence on moisture distribution in forests. The methodology and results presented in this chapter contribute to increased interpretation capability of the scattering mechanisms in canopies.



# 6

## CONCLUSIONS

*In the previous chapters, we extended our physical understanding of the relationship between vegetation water dynamics and radar backscatter. In the context of the previous chapters, this final chapter discusses to what extent the research objectives presented in the Introduction have been achieved. It also discusses the implications for the use of current satellite-based radar data and the design of future missions. Finally, recommendations and an outlook for future research are presented.*

## 6.1. MAIN FINDINGS

This dissertation aimed to better understand the physical relationship between vegetation water dynamics and radar backscatter. Extensive field experiments have been conducted to quantify the water movement and storage in a corn field. Estimates of vegetation water content (VWC), surface canopy water (SCW) and surface soil moisture (SSM) were used to interpret temporal dynamics in ground-based, VV-, HH-, and cross-polarized L-band backscatter ( $\sigma^0$ ) using both statistical analyses and electromagnetic models.

It was shown that, contrary to what is often assumed, the diurnal VWC cycle plays an important role in sub-daily  $\sigma^0$  variations. The VWC of the studied corn plants varied by 35% on a drought-stressed day, compared to 10-20% in non-stressed conditions. In the second half of the season, these percentages translate to substantial masses of water in the order of 0.5 - 1.5 kg m<sup>-2</sup>. It turned out that these variations in VWC were large enough to significantly affect  $\sigma^0$ , particularly on days without rainfall. Multiple linear regression showed that, on a typical dry day in mid-to-late growing season, backscatter behaviour was 2 (HH- and cross-pol) to 4 (VV-pol) times more determined by variations in VWC than by the drydown of soil moisture. In early season, sub-daily fluctuations in  $\sigma^0$  were mainly governed by changes in surface soil moisture and dew deposition on the topsoil.

Furthermore, it has been shown that surface canopy water (SCW), i.e. dew or rainfall intercepted by the foliage, does have a non-negligible effect on sub-daily variations of  $\sigma^0$ . This effect was largely ignored in previous research. The free SCW added an estimated maximum of 10% (dew) to 20% (interception) to the mass of moisture in the vegetation layer during an event. Although smaller than the effect of the diurnal VWC cycle, we observed clear nocturnal increase of  $\sigma^0$  in VV- and cross-pol, closely following the slow accumulation of dew, and reaching a maximum just before dew dissipation started. These observations suggest that also rainfall interception plays an important role in increased scattering and attenuation. However, isolating effects of rainfall interception was difficult due to the simultaneous increase in soil moisture during most events.

Finally, it has been demonstrated that certain parts of the vertical vegetation column control the backscatter dynamics, depending on stage in the season. Field observations showed that the vertical moisture distribution of VWC is non-uniform and highly dynamic in time. When incorporating this vertical moisture distribution in the Water Cloud Model, simulations suggest a shift in the relative importance of different vertical layers on the backscatter signal over the season. Dominant vegetation scattering in all polarizations changes from the lowest 50cm to 50-100cm once the latter contains  $\geq 1$  kg m<sup>-2</sup> of moisture, and the former  $\leq 2.3$  kg m<sup>-2</sup>. Ear formation in 50-100cm further increases scattering from this layer, and also increases the attenuating effect on the lowest layer. Although the lowest layer, dominated by stem water content, contains  $>2$  times more water than the top half of the canopy, VV- and cross-pol scattering from both were comparable in the late season. HH-pol simulations showed more sensitivity to the top half than to the lowest quarter of the plants at this stage.

## 6.2. IMPLICATIONS

We have shown, within the scope of our research (i.e. ground-based, L-band frequency, and corn), which information about vegetation water dynamics is captured within the time series of the different polarizations. Here, it will be argued that our findings indirectly demonstrate the potential to use radar to measure vegetation water dynamics on larger scales from space with future instruments. They also show implications for the use of the current generation of spaceborne instruments.

For example, the sensitivity to sub-daily variations in VWC and SCW means that the overpass time of current satellites may have important consequences for the retrieval of biophysical variables (e.g. LAI or dry biomass) or soil moisture. Most satellites carrying radar instruments are in near-polar, sun-synchronous orbits with morning/evening local overpass times between 4:00 AM/PM and 10:00 AM/PM. Future SAR missions such as ROSE-L and NISAR are expected to be in similar orbits (Pierdicca et al., 2019; Rosen et al., 2017). During morning overpasses, dew will be frequently present on vegetation, particularly in temperate regions (Hornbuckle et al., 2010; Kabela et al., 2009; Khabbazan et al., 2021; Vermunt et al., 2020). In a recent study, it was shown that the presence of dew significantly affects the retrieval of biophysical variables (Khabbazan et al., 2022). Similarly, it is expected that the evening refill of internal VWC, which depends on the specific hydrometeorological conditions during a day, affects retrievals of biophysical variables or soil moisture from the evening overpasses. This is particularly relevant since many of the current retrieval algorithms consider that VWC is constant during the day (Bindlish et al., 2009; S.-B. Kim et al., 2017; Panciera et al., 2014). It will have to be examined to what extent this causes errors in studies using these retrievals. In any case, these sub-daily effects should be considered when combining overpass times or selecting an observation time for future missions.

In addition, backscatter sensitivity to sub-daily VWC and SCW also offers unique opportunities. Particularly the availability of multiple satellite observations per day offers a range of possibilities. In Chapters 3 and 4, we demonstrated that we can largely differentiate between the timing and shapes of nocturnal dew accumulation, the diurnal VWC cycle, transient interception events and soil moisture variations. Consequently, having sub-daily spaceborne backscatter time series will make it much easier to disentangle these signals and isolate the signal of interest. This is certainly the case if different polarizations are available as well. For example, we showed that sub-daily variations of VV-polarized backscatter were highly sensitive to the nocturnal cycle of SCW and the diurnal cycle of VWC. HH-polarized backscatter was much less sensitive to these cycles, and showed higher sensitivity to soil moisture instead. These two polarizations could thus be used to separate soil moisture from vegetation water dynamics.

This also means, and that was the point of departure for this dissertation (see Section 1.1), that rapid vegetation water dynamics (i.e. VWC, SCW) could be monitored from space, when sub-daily observations become available. This provides opportunities for assessing vegetation health and studying the diurnal water cycle from a new perspective. Studies on drought-induced water stress, drought propagation, the role of dew uptake as a source of water, and ecosystem sensitivity to global change could benefit from sub-daily measurements of VWC and SCW (Gerlein-Safdi, 2021; Konings et al., 2021; Xu et al., 2021; Yebra et al., 2019).

The availability of sub-daily radar observations does not only pertain to the distant future. Commercial providers CapellaSpace and ICEYE are currently populating constellations of X-band SAR systems in Low Earth Orbit (Farquharson et al., 2021; Ignatenko et al., 2020). These constellations will ensure multiple observations per day. In February 2021, HydroTerra, one of the candidate missions bidding to become the ESA's 10th Pathfinder mission, was not selected for further design consolidation and feasibility assessment. This concept mission was a C-band geostationary SAR which was specifically designed to study the diurnal water cycle by delivering sub-daily data (Hobbs et al., 2019). Research as presented in this dissertation can support further development of concept missions like HydroTerra.

The results from studying the effect of vertical moisture distribution on backscatter (Chapter 5) is currently primarily of academic value. They provide unique insights into the contribution of different depths in a vegetation layer on radar backscatter. These insights serve as starting point for further exploring this issue with more sophisticated electromagnetic models (see Section 6.3.2). Although understanding what controls the signal is valuable in itself, future research may reveal which parts of the vegetation layer control backscatter from different frequencies. Ultimately, this will contribute to better understanding the potential for multi-frequency radars. It is expected that at least, multi-frequency backscatter would benefit the disentangling of signals from soil and vegetation (Mengen et al., 2021). Moreover, in theory, multi-frequency backscatter could provide us with a detailed picture of the water dynamics in a field or forest, from soil moisture to water content across different heights in the canopy, including dew deposition at the leaf surfaces (Gerlein-Safdi, 2021; Konings et al., 2021). This would shed new light on plant hydraulics across scales, and the role of vegetation in the climate system. Finally, insights into the influence of vertical moisture distribution on attenuation, and thus VOD, will also be interesting for passive multi-frequency microwave instruments, such as the planned Copernicus Imaging Microwave Radiometer (CIMR).

## 6.3. DIRECTIONS FOR FURTHER RESEARCH

### 6.3.1. CALIBRATION/VALIDATION CAMPAIGNS FOR MICROWAVE REMOTE SENSING OF VEGETATION

In our extensive experimental campaigns (Chapter 2), we collected a wide range of quantitative information on hydrodynamic activity in the fields with unprecedented temporal resolution. It was the first time that variations in radar backscatter were linked to continuous and simultaneous estimates of soil moisture, surface canopy water and internal vegetation water content. It was demonstrated that particularly the use of sap flow and leaf wetness sensors to estimate VWC and SCW, respectively, have a huge value for future calibration/validation campaigns, given the importance of these estimates, and the laboriousness to measure them. The utility of insights from these campaigns goes well beyond active microwave remote sensing of vegetation, and is useful for passive microwave remote sensing and exploring the potential for techniques as GNSS and cosmic ray neutron.

It is strongly recommended to repeat the analyses of Chapter 5 with observations from a multi-frequency radar. With these observations, the potential of using multiple

frequencies for determining water content across different heights and disentangling VWC, SCW and SSM could be properly understood. Moreover, it could be investigated which frequency would be most suitable to monitor sub-daily vegetation water dynamics.

Another recommendation for future campaigns is to install a denser network of leaf wetness sensors. We observed that the variations in the raw data from the leaf wetness sensors were consistent with the accumulation of dew during humid periods, interception during rain and irrigation events and the dissipation of both in response to net radiation. These suggest that the sensors reflect field scale phenomena. However, the certainty of the SCW estimates was limited by the number of sensors available for the campaigns. In addition, a denser network of sensors could provide better insight into spatial and vertical heterogeneity. Given the value of these sensors, the user-friendliness, and the relatively low costs, it is recommended to use multiple leaf wetness sensors for future calibration and validation campaigns.

In Chapter 4, we used sap flow sensors and reference ET to extrapolate VWC. This methodology gave us the opportunity to link sub-daily backscatter to diurnal VWC variations. However, the resulting time series was limited to mid-to-late-season due to the large diameters of the sap flow gauges we had available. Moreover, it was demonstrated that the extrapolations and observations did not always match. Poor estimates of diurnal VWC cycles risk an underestimation of the effect of VWC on backscatter. Given the value of continuous VWC estimates for calibration or validation of microwave observables, it is important to further develop this method and reduce the uncertainty. Potential improvements could be the use of eddy covariance systems to estimate ET, and the use of multiple sap flow sensors. It is also recommended to increase the temporal resolution of the sensor observations to increase the robustness of the method.

For the field campaigns in this dissertation, we used corn as vegetation type. However, our measurements can also be applied to campaigns focused on forests, such as TropiScat (Albinet et al., 2012) and BorealScat (Monteith et al., 2016). In fact, it is expected that estimates of continuous VWC variations using sap flow sensors are more accurate for trees than for agricultural crops, because of the longer phase lags between transpiration and basal sap flow, and thus higher robustness. Other types of sensors have also proven their utility for relating vegetation water changes to microwave observables, such as automated psychrometers to measure plant water potential (Guo et al., 2020; Holtzman et al., 2021; Momen et al., 2017) and dendrometers to estimate variations in stem diameter as an indication of variations in stem water storage (van Emmerik et al., 2017). It is important to note that dielectric constant is directly related to water content, and not to water potential. It is therefore essential to further develop methods to measure water content continuously.

Much of the necessary data is also collected in scientific measurement networks, some of which have been set up recently. These networks could make a major contribution to the validation of (sub-daily) satellite observations. Examples of these networks are FLUXNET (Baldocchi et al., 2001) and AMERIFLUX (Novick et al., 2018), from which ET could be derived, SAPFLUXNET (Poyatos et al., 2021), with sap flow data, sometimes corresponding to FLUXNET observations, and Globe-LFMC (Yebra et al., 2019), which is a data set containing VWC data from all over the world.

### 6.3.2. ELECTROMAGNETIC MODELLING

The regression analysis in Chapter 4 gave us valuable insights into the dependence of sub-daily backscatter variations on changes in the different moisture stores in the field. However, the calibration and fitted relationships are site- and crop-specific. Electromagnetic models on a physical basis, such as the Michigan Microwave Canopy Scattering Model (MIMICS) (Ulaby et al., 1990) and the Tor Vergata Model (TVM) (Bracaglia et al., 1995), have a broader validity and can be used to extrapolate insights to other situations. These models are broadly used to explain variations in backscatter time series related to changing properties on the ground.

The models we used for forward modelling in this dissertation were not able to capture the sub-daily dynamics in observed  $\sigma^0$ . This could have several reasons. It could be that the backscatter observations from the UF-LARS system were more sensitive to sub-daily variations in the field than the observations from instruments on which the models were initially developed. To investigate whether this could be a reason, it is recommended to repeat the experiments described in this dissertation with other instruments, ground-based or airborne, with different configurations, and compare the observations with model simulations.

The more likely explanation is related to the fact that the models were initially developed for capturing seasonal variations of vegetation growth. Both the Water Cloud Model and the Tor Vergata Model simulated seasonal variations of  $\sigma^0$  reasonably well. However, sub-daily dynamics were structurally underestimated. This is a problem because in their current form, the models cannot be used for explaining sub-daily variability in  $\sigma^0$ . Moreover, this suggests that some processes in the model are not well described, which also has implications for the validity of seasonal scale modelling (see Chapter 5).

For these reasons, it is of utmost importance to update these models in such a way that they are able to simulate sub-daily dynamics of  $\sigma^0$  properly. First attempts were already made within the time of writing this dissertation. We for example found that a WCM which incorporates an extra vegetation descriptor showed stronger sub-daily dynamics of  $\sigma^0$  than the original WCM. However, this modified WCM performance was worse in the period of strong seasonal backscatter increase. Choices in the TVM can improve the representation of sub-daily variations as well; for example through changing the linear vegetation mixing model from Mätzler (Matzler, 1994) for the exponential dual-dispersion model described in Ulaby and El-Rayes (Ulaby and El-rayes, 1987).

However, the modifications mentioned above were not sufficient to capture sub-daily variability. Both the WCM and the TVM do not include scattering from surface canopy water. When we added estimates of SCW to the water cloud of the vegetation layers, WCM simulations underestimated their effect on  $\sigma^0$  (Chapter 5). We should bear in mind that scattering from free water on the canopy could be different than the scattering from water captured in vegetation tissue. Given the importance of SCW on sub-daily backscatter shown in this dissertation, it is recommended to work on the incorporation of surface water on vegetation in electromagnetic models.

It is also recommended to repeat the analysis in Chapter 5 by building-in multiple layers in the TVM. The simplicity of the WCM does not allow vegetation-ground scattering and scattering between vegetation layers. Our simulations from the WCM sug-

gest that the vegetation-ground scattering plays an important role. The TVM does allow vegetation-ground scattering and scattering between layers because of the built-in matrix doubling algorithm (Eom and Fung, 1984). In addition, there is an option to use elementary sublayers, i.e. sublayers within layers, using "additive" doubling. These options are potentially interesting for further studying scattering from different vertical layers with a more sophisticated model. A modified version of the TVM should be able to account for these scattering mechanisms, and is expected to better represent scattering from the different vertical layers.

While we work on extending our physical understanding, we should also, above all, continue working on inferring information of vegetation water dynamics from variations in backscatter. In the end, we want to use radar to study processes on the Earth surface. Improvements in inverse modelling would bring the potential for using radar a step further.

## 6.4. CONCLUDING REMARKS

The use of radar remote sensing for environmental studies remains challenging due to the complexity of the data. At the same time, the variety of hidden information in the data makes it interesting to explore the potential of this technique. This dissertation provides important observational evidence for the potential of using radar to monitor rapid vegetation water dynamics from different layers in a canopy. This means that sub-daily and multi-frequency satellite-based radar could become a crucial data source for applications in the fields of hydrology, land surface modelling, earth system modelling and plant physiology, once these instruments are in orbit.

It is essential to continue efforts to improve our understanding of complex radar observations. A lot of what we know about radar remote sensing of vegetation is based on field experiments from decades ago, and electromagnetic models which were developed to capture seasonal growth. However, understanding the potential of monitoring detailed vegetation water dynamics using radar requires continued field research and modelling. Experimental campaigns are expensive but crucial if we want to exploit the potential of radar remote sensing. Moreover, the possibilities of today's sensors are greater than ever before. An update of forward models is needed to better capture the effect of vegetation water dynamics. Finally, it is essential to master inferring information on rapid vegetation water dynamics from a backscatter time series using inverse modelling. The findings in this dissertation open a new avenue for these developments.





## REFERENCES

- Albinet, C., Borderies, P., Koleck, T., Rocca, F., Tebaldini, S., Villard, L., Le Toan, T., Hamadi, A., & Ho Tong Minh, D. (2012). TropiSCAT: A Ground Based Polarimetric Scatterometer Experiment in Tropical Forests. *IEEE Journal of Selected Topics in Applied Earth Observations and Remote Sensing*, 5(3), 1060–1066. <https://doi.org/10.1109/JSTARS.2012.2201917>
- Allen, C., & Ulaby, F. T. (1984). Modelling the polarization dependence of the attenuation in vegetation canopies, In *Proceedings of IGARSS'84 Symposium*, Strasbourg, France.
- Allen, R. G., Pereira, L. S., Raes, D., & Smith, M. (1998). Crop evapotranspiration: Guidelines for computing crop water requirements, FAO Drainage and Irrigation Paper 56.
- Allen, S. T., Aubrey, D. P., Bader, M. Y., Coenders-Gerrits, M., Friesen, J., Gutmann, E. D., Guillemette, F., Jiménez-Rodríguez, C., Keim, R. F., Klammerus-Iwan, A., Mendieta-Leiva, G., Porada, P., Qualls, R. G., Schilperoort, B., Stubbins, A., & Van Stan II, J. T. (2020). Key Questions on the Evaporation and Transport of Intercepted Precipitation (I. Van Stan J. T., E. Gutmann, & J. Friesen, Eds.). In I. Van Stan J. T., E. Gutmann, & J. Friesen (Eds.), *Precipitation Partitioning by Vegetation: A Global Synthesis*. Cham, Springer International Publishing. [https://doi.org/10.1007/978-3-030-29702-2\\_16](https://doi.org/10.1007/978-3-030-29702-2_16)
- Álvarez-Mozos, J., González-Audícana, M., Casali, J., & Larranaga, A. (2008). Effective versus measured correlation length for radar-based surface soil moisture retrieval. *International Journal of Remote Sensing*, 29(17–18), 5397–5408. <https://doi.org/10.1080/01431160802036367>
- Attema, E. P. W., & Ulaby, F. T. (1978). Vegetation modeled as a water cloud. *Radio Science*, 13(2), 357–364. <https://doi.org/10.1029/RS013i002p00357>
- Atzema, A. J., Jacobs, A. F. G., & Wartena, L. (1990). Moisture distribution within a maize crop due to dew. *Netherlands Journal of Agricultural Science*, 38(2), 117–129. <https://doi.org/10.18174/njas.v38i2.16599>
- Baldocchi, D., Falge, E., Gu, L., Olson, R., Hollinger, D., Running, S., Anthoni, P., Bernhofer, C., Davis, K., Evans, R., Fuentes, J., Goldstein, A., Katul, G., Law, B., Lee, X., Malhi, Y., Meyers, T., Munger, W., Oechel, W., . . . Wofsy, S. (2001). FLUXNET: A New Tool to Study the Temporal and Spatial Variability of Ecosystem-Scale Carbon Dioxide, Water Vapor, and Energy Flux Densities. *Bulletin of the American Meteorological Society*, 82(11), 2415–2434. [https://doi.org/10.1175/1520-0477\(2001\)082<2415:FANTTS>2.3.CO;2](https://doi.org/10.1175/1520-0477(2001)082<2415:FANTTS>2.3.CO;2)
- Banerjee, T., & Linn, R. (2018). Effect of Vertical Canopy Architecture on Transpiration, Thermoregulation and Carbon Assimilation. *Forests*, 9(4), 198. <https://doi.org/10.3390/f9040198>

- Bartholomeus, R., de Louw, P., Witte, F., van Dam, J., van Deijl, D., Hoefsloot, P., van Huijgevoort, M., Hunink, J., America, I., Pouwels, J., & de Wit, J. (2020). *Droogte in zandgebieden van Zuid-, Midden-en Oost-Nederland: Het verhaal: Analyse van droogte 2018 en 2019 en tussentijdse bevindingen*. (tech. rep.). KWR. <https://edepot.wur.nl/534198>
- Bindlish, R., Jackson, T., Sun, R., Cosh, M., Yueh, S., & Dinardo, S. (2009). Combined Passive and Active Microwave Observations of Soil Moisture During CLASIC. *IEEE Geoscience and Remote Sensing Letters*, 6(4), 644–648. <https://doi.org/10.1109/LGRS.2009.2028441>
- Blyth, E., & Harding, R. J. (2011). Methods to separate observed global evapotranspiration into the interception, transpiration and soil surface evaporation components. *Hydrological Processes*, 25(26), 4063–4068. <https://doi.org/10.1002/hyp.8409>
- Bongiovanni, T., Liu, P.-W., Nagarajan, K., Preston, D., Rush, P., Duan, X., Chen, G., Terwilleger, R., Monsivais-Huertero, A., Judge, J., Morris, M., Williams, O., Marks, L., Cardozo, C., Moghaddam, M., & England, A. (2015). Field Observations during the Tenth Microwave Water and Energy Balance Experiment (MicroWEX-10): From March 1, 2011, through January 5, 2012 [Agricultural and Biological Engineering Department, UF/IFAS Extension, University of Florida.].
- Bongiovanni, T., Liu, P.-W., Nagarajan, K., Preston, D., Rush, P., Monsivais-Huertero, A., Judge, J., Steele-Dunne, S. C., Wallace, M., & England, A. (2018). Field Observations during the Eleventh Microwave Water and Energy Balance Experiment (MicroWEX-11): From April 25, 2012, through December 6, 2012 [Agricultural and Biological Engineering Department, UF/IFAS Extension, University of Florida.].
- Bouman, B. A. M., & Hoekman, D. H. (1993). Multi-temporal, multi-frequency radar measurements of agricultural crops during the Agriscatt-88 campaign in The Netherlands. *International Journal of Remote Sensing*, 14(8), 1595–1614. <https://doi.org/10.1080/01431169308953988>
- Bouten, W., Swart, P. J. F., & De Water, E. (1991). Microwave transmission, a new tool in forest hydrological research. *Journal of Hydrology*, 124(1), 119–130. [https://doi.org/10.1016/0022-1694\(91\)90009-7](https://doi.org/10.1016/0022-1694(91)90009-7)
- Bracaglia, M., Ferrazzoli, P., & Guerriero, L. (1995). A fully polarimetric multiple scattering model for crops. *Remote Sensing of Environment*, 54(3), 170–179. [https://doi.org/10.1016/0034-4257\(95\)00151-4](https://doi.org/10.1016/0034-4257(95)00151-4)
- Brancato, V., Liebisch, F., & Hajnsek, I. (2017). Impact of Plant Surface Moisture on Differential Interferometric Observables: A Controlled Electromagnetic Experiment. *IEEE Transactions on Geoscience and Remote Sensing*, 55(7), 3949–3964. <https://doi.org/10.1109/TGRS.2017.2684814>
- Brisco, B., Brown, R. J., Koehler, J. A., Sofko, G. J., & McKibben, M. J. (1990). The diurnal pattern of microwave backscattering by wheat. *Remote Sensing of Environment*, 34(1), 37–47. [https://doi.org/10.1016/0034-4257\(90\)90082-W](https://doi.org/10.1016/0034-4257(90)90082-W)
- Brocca, L., Hasenauer, S., Lacava, T., Melone, F., Moramarco, T., Wagner, W., Dorigo, W., Matgen, P., Martínez-Fernández, J., Llorens, P., Latron, J., Martin, C., & Bittelli, M. (2011). Soil moisture estimation through ASCAT and AMSR-E sensors: An intercomparison and validation study across Europe. *Remote Sensing of Environment*, 115(12), 3390–3408. <https://doi.org/10.1016/j.rse.2011.08.003>

- Casanova, J. J., Judge, J., & Jang, M. (2007). Modeling Transmission of Microwaves Through Dynamic Vegetation. *IEEE Transactions on Geoscience and Remote Sensing*, 45(10), 3145–3149. <https://doi.org/10.1109/TGRS.2007.902302>
- Čermák, J., Kučera, J., Bauerle, W. L., Phillips, N., & Hinckley, T. M. (2007). Tree water storage and its diurnal dynamics related to sap flow and changes in stem volume in old-growth Douglas-fir trees. *Tree Physiology*, 27(2), 181–198. <https://doi.org/10.1093/treephys/27.2.181>
- Chauhan, N., Le Vine, D., & Lang, R. (1994). Discrete scatter model for microwave radar and radiometer response to corn: Comparison of theory and data. *IEEE Transactions on Geoscience and Remote Sensing*, 32(2), 416–426. <https://doi.org/10.1109/36.295056>
- Cloude, S., & Pottier, E. (1997). An entropy based classification scheme for land applications of polarimetric SAR. *IEEE Transactions on Geoscience and Remote Sensing*, 35(1), 68–78. <https://doi.org/10.1109/36.551935>
- Cobos, D. (2013). Predicting the amount of water on the surface of the LWS dielectric leaf wetness sensor [Application Note]. Decagon Devices Inc.
- Cosh, M. H., Kabela, E. D., Hornbuckle, B., Gleason, M. L., Jackson, T. J., & Prueger, J. H. (2009). Observations of dew amount using in situ and satellite measurements in an agricultural landscape. *Agricultural and Forest Meteorology*, 149(6), 1082–1086. <https://doi.org/10.1016/j.agrformet.2009.01.004>
- Cosh, M. H., Ochsner, T. E., McKee, L., Dong, J., Basara, J. B., Evett, S. R., Hatch, C. E., Small, E. E., Steele-Dunne, S. C., Zreda, M., & Sayde, C. (2016). The Soil Moisture Active Passive Marena, Oklahoma, In Situ Sensor Testbed (SMAP-MOISST): Testbed Design and Evaluation of In Situ Sensors. *Vadose Zone Journal*, 15(4), 1–11. <https://doi.org/10.2136/vzj2015.09.0122>
- Dawson, T. E., & Goldsmith, G. R. (2018). The value of wet leaves. *New Phytologist*, 219(4), 1156–1169. <https://doi.org/10.1111/nph.15307>
- De Jong, J., Klaassen, W., & Kuiper, P. (2002). Monitoring of rain water storage in forests with satellite radar. *IEEE Transactions on Geoscience and Remote Sensing*, 40(2), 338–347. <https://doi.org/10.1109/36.992793>
- de Jong, S. M., & Jetten, V. G. (2007). Estimating spatial patterns of rainfall interception from remotely sensed vegetation indices and spectral mixture analysis. *International journal of geographical information science*, 21(5), 529–545. <https://doi.org/10.1080/13658810601064884>
- Della Vecchia, A., Ferrazzoli, P., Guerriero, L., Blaes, X., Defourny, P., Dente, L., Mattia, F., Satalino, G., Strozzi, T., & Wegmuller, U. (2006). Influence of geometrical factors on crop backscattering at C-band. *IEEE Transactions on Geoscience and Remote Sensing*, 44(4), 778–790. <https://doi.org/10.1109/TGRS.2005.860489>
- Dickey, F. M., King, C., Holtzman, J. C., & Moore, R. K. (1974). Moisture Dependency of Radar Backscatter from Irrigated and Non-Irrigated Fields at 400 MHz and 13.3 GHz. *IEEE Transactions on Geoscience Electronics*, 12(1), 19–22. <https://doi.org/10.1109/TGE.1974.294326>
- Ding, R., Kang, S., Zhang, Y., Hao, X., Tong, L., & Du, T. (2013). Partitioning evapotranspiration into soil evaporation and transpiration using a modified dual crop coef-

- ficient model in irrigated maize field with ground-mulching. *Agricultural Water Management*, 127, 85–96. <https://doi.org/10.1016/j.agwat.2013.05.018>
- Dobriyal, P., Qureshi, A., Badola, R., & Hussain, S. A. (2012). A review of the methods available for estimating soil moisture and its implications for water resource management. *Journal of Hydrology*, 458-459, 110–117. <https://doi.org/10.1016/j.jhydrol.2012.06.021>
- Drusch, M., Wood, E. F., & Gao, H. (2005). Observation operators for the direct assimilation of TRMM microwave imager retrieved soil moisture. *Geophysical Research Letters*, 32(15), L15403. <https://doi.org/10.1029/2005GL023623>
- Dubois, P., van Zyl, J., & Engman, T. (1995). Measuring soil moisture with imaging radars. *IEEE Transactions on Geoscience and Remote Sensing*, 33(4), 915–926. <https://doi.org/10.1109/36.406677>
- El Hajj, M., Baghdadi, N., Wigneron, J.-P., Zribi, M., Albergel, C., Calvet, J.-C., & Fayad, I. (2019). First Vegetation Optical Depth Mapping from Sentinel-1 C-band SAR Data over Crop Fields. *Remote Sensing*, 11(23), 2769. <https://doi.org/10.3390/rs11232769>
- El Hajj, M., Baghdadi, N., Zribi, M., Belaud, G., Cheviron, B., Courault, D., & Charron, F. (2016). Soil moisture retrieval over irrigated grassland using X-band SAR data. *Remote Sensing of Environment*, 176, 202–218. <https://doi.org/10.1016/j.rse.2016.01.027>
- El-rayes, M. A., & Ulaby, F. T. (1987). Microwave Dielectric Spectrum of Vegetation-Part I: Experimental Observations. *IEEE Transactions on Geoscience and Remote Sensing*, GE-25(5), 541–549. <https://doi.org/10.1109/TGRS.1987.289832>
- Entekhabi, D., Njoku, E. G., O'Neill, P. E., Kellogg, K. H., Crow, W. T., Edelstein, W. N., Entin, J. K., Goodman, S. D., Jackson, T. J., Johnson, J., Kimball, J., Piepmeier, J. R., Koster, R. D., Martin, N., McDonald, K. C., Moghaddam, M., Moran, S., Reichle, R., Shi, J. C., ... Zyl, J. V. (2010). The Soil Moisture Active Passive (SMAP) Mission. *Proceedings of the IEEE*, 98(5), 704–716. <https://doi.org/10.1109/JPROC.2010.2043918>
- Eom, H. J., & Fung, A. K. (1984). A scatter model for vegetation up to Ku-band. *Remote Sensing of Environment*, 15(3), 185–200. [https://doi.org/10.1016/0034-4257\(84\)90030-0](https://doi.org/10.1016/0034-4257(84)90030-0)
- Farquharson, G., Castelletti, D., Stringham, C., & Eddy, D. (2021). An Update on the Capella Space Radar Constellation, In *EUSAR 2021; 13th European Conference on Synthetic Aperture Radar*, Online.
- Ferrazzoli, P., Paloscia, S., Pampaloni, P., Schiavon, G., Solimini, D., & Coppo, P. (1992). Sensitivity of microwave measurements to vegetation biomass and soil moisture content: A case study. *IEEE Transactions on Geoscience and Remote Sensing*, 30(4), 750–756. <https://doi.org/10.1109/36.158869>
- Fisher, J. B., Melton, F., Middleton, E., Hain, C., Anderson, M., Allen, R., McCabe, M. F., Hook, S., Baldocchi, D., Townsend, P. A., Kilic, A., Tu, K., Miralles, D. D., Perret, J., Lagouarde, J.-P., Waliser, D., Purdy, A. J., French, A., Schimel, D., ... Wood, E. F. (2017). The future of evapotranspiration: Global requirements for ecosystem functioning, carbon and climate feedbacks, agricultural management, and

- water resources. *Water Resources Research*, 53(4), 2618–2626. [https://doi.org/10.1002/2016WR020175@10.1002/\(ISSN\)1944-9208.COMHES1](https://doi.org/10.1002/2016WR020175@10.1002/(ISSN)1944-9208.COMHES1)
- Frappart, F., Wigneron, J.-P., Li, X., Liu, X., Al-Yaari, A., Fan, L., Wang, M., Moisy, C., Le Masson, E., Aoulad Lafkih, Z., Vallé, C., Ygorra, B., & Baghdadi, N. (2020). Global Monitoring of the Vegetation Dynamics from the Vegetation Optical Depth (VOD): A Review. *Remote Sensing*, 12(18), 2915. <https://doi.org/10.3390/rs12182915>
- Frasson, R. P. d. M., & Krajewski, W. F. (2013). Rainfall interception by maize canopy: Development and application of a process-based model. *Journal of Hydrology*, 489, 246–255. <https://doi.org/10.1016/j.jhydrol.2013.03.019>
- Friesen, J., Steele-Dunne, S. C., & van de Giesen, N. (2012). Diurnal Differences in Global ERS Scatterometer Backscatter Observations of the Land Surface. *IEEE Transactions on Geoscience and Remote Sensing*, 50(7), 2595–2602. <https://doi.org/10.1109/TGRS.2012.2193889>
- Frolking, S., Milliman, T., Palace, M., Wisser, D., Lammers, R., & Fahnestock, M. (2011). Tropical forest backscatter anomaly evident in SeaWinds scatterometer morning overpass data during 2005 drought in Amazonia. *Remote Sensing of Environment*, 115(3), 897–907. <https://doi.org/10.1016/j.rse.2010.11.017>
- Fung, A. K. (1994). *Microwave scattering and emission models and their applications*. Artech House.
- Gerlein-Safdi, C. (2021). Seeing dew deposition from satellites: Leveraging microwave remote sensing for the study of water dynamics in and on plants. *New Phytologist*, 231(1), 5–7. <https://doi.org/10.1111/nph.17418>
- Gillespie, T. J., Brisco, B., Brown, R. J., & Sofko, G. J. (1990). Radar Detection of a Dew Event in Wheat. *Remote Sensing of Environment*, 33(3), 151–156. [https://doi.org/10.1016/0034-4257\(90\)90026-I](https://doi.org/10.1016/0034-4257(90)90026-I)
- Goldstein, G., Andrade, J. L., Meinzer, F. C., Holbrook, N. M., Cavelier, J., Jackson, P., & Celis, A. (1998). Stem water storage and diurnal patterns of water use in tropical forest canopy trees. *Plant, Cell & Environment*, 21(4), 397–406. <https://doi.org/10.1046/j.1365-3040.1998.00273.x>
- Guo, J. S., Hultine, K. R., Koch, G. W., Kropp, H., & Ogle, K. (2020). Temporal shifts in iso/anisohydry revealed from daily observations of plant water potential in a dominant desert shrub. *New Phytologist*, 225(2), 713–726. <https://doi.org/10.1111/nph.16196>
- Gupta, H. V., Kling, H., Yilmaz, K. K., & Martinez, G. F. (2009). Decomposition of the mean squared error and NSE performance criteria: Implications for improving hydrological modelling. *Journal of Hydrology*, 377(1), 80–91. <https://doi.org/10.1016/j.jhydrol.2009.08.003>
- Hamadi, A., Albinet, C., Borderies, P., Koleck, T., Villard, L., Ho Tong Minh, D., & Le Toan, T. (2014). Temporal Survey of Polarimetric P-Band Scattering of Tropical Forests. *IEEE Transactions on Geoscience and Remote Sensing*, 52(8), 4539–4547. <https://doi.org/10.1109/TGRS.2013.2282357>
- Herold, M., Pathe, C., & Schmullius, C. (2001). The effect of free vegetation water on the multi-frequency and polarimetric radar backscatter—First, results from the TerraDew 2000 campaign. *Proceedings of the IEEE 2001 International Geoscience*

- and Remote Sensing Symposium, Sydney, Australia, 5, 2445–2447. <https://doi.org/10.1109/IGARSS.2001.978030>*
- Hobbs, S. E., Guarnieri, A. M., Broquetas, A., Calvet, J.-C., Casagli, N., Chini, M., Ferretti, R., Nagler, T., Pierdicca, N., Prudhomme, C., & Wadge, G. (2019). G-CLASS: Geosynchronous radar for water cycle science – orbit selection and system design. *The Journal of Engineering, 2019*(21), 7534–7537. <https://doi.org/10.1049/joe.2019.0601>
- Hoekman, D. H. (1987). Measurements of the backscatter and attenuation properties of forest stands at X-, C- and L-band. *Remote Sensing of Environment, 23*(3), 397–416. [https://doi.org/10.1016/0034-4257\(87\)90098-8](https://doi.org/10.1016/0034-4257(87)90098-8)
- Holtzman, N. M., Anderegg, L. D. L., Kraatz, S., Mavrovic, A., Sonnentag, O., Pappas, C., Cosh, M. H., Langlois, A., Lakhankar, T., Tesser, D., Steiner, N., Colliander, A., Roy, A., & Konings, A. G. (2021). L-band vegetation optical depth as an indicator of plant water potential in a temperate deciduous forest stand. *Biogeosciences, 18*(2), 739–753. <https://doi.org/10.5194/bg-18-739-2021>
- Hornbuckle, B. K., Rowlandson, T. L., Russell, E., Kaleita, A., Logsdon, S., Kruger, A., Yueh, S., & DeRoo, R. (2010). How does dew affect L-band backscatter? Analysis of PALS data at the Iowa validation site and implications for SMAP. *2010 IEEE International Geoscience and Remote Sensing Symposium, 4835–4838. <https://doi.org/10.1109/IGARSS.2010.5650792>*
- Hosseini, M., McNairn, H., Merzouki, A., & Pacheco, A. (2015). Estimation of Leaf Area Index (LAI) in corn and soybeans using multi-polarization C-and L-band radar data. *Remote Sensing of Environment, 170*, 77–89. <https://doi.org/10.1016/j.rse.2015.09.002>
- Hu, C., Li, Y., Dong, X., Cui, C., & Long, T. (2016). Impacts of Temporal-Spatial Variant Background Ionosphere on Repeat-Track GEO D-InSAR System. *Remote Sensing, 8*(11), 916. <https://doi.org/10.3390/rs8110916>
- Ignatenko, V., Laurila, P., Radius, A., Lamentowski, L., Antropov, O., & Muff, D. (2020). ICEYE Microsatellite SAR Constellation Status Update: Evaluation of First Commercial Imaging Modes, Online, IGARSS - IEEE International Geoscience; Remote Sensing Symposium. <https://doi.org/10.1109/IGARSS39084.2020.9324531>
- Inoue, Y., Kurosu, T., Maeno, H., Uratsuka, S., Kozu, T., Dabrowska-Zielinska, K., & Qi, J. (2002). Season-long daily measurements of multifrequency (Ka, Ku, X, C, and L) and full-polarization backscatter signatures over paddy rice field and their relationship with biological variables. *Remote Sensing of Environment, 81*(2), 194–204. [https://doi.org/10.1016/S0034-4257\(01\)00343-1](https://doi.org/10.1016/S0034-4257(01)00343-1)
- Jacobs, A. F. G., Pul, W. A. J. v., & Dijken, A. v. (1990). Similarity Moisture Dew Profiles within a Corn Canopy. *Journal of Applied Meteorology and Climatology, 29*(12), 1300–1306. [https://doi.org/10.1175/1520-0450\(1990\)029<1300:SMDPWA>2.0.CO;2](https://doi.org/10.1175/1520-0450(1990)029<1300:SMDPWA>2.0.CO;2)
- Jang, M.-y., Tien, K.-j. C., Casanova, J., & Judge, J. (2005). Measurements of Soil Surface Roughness During the Fourth Microwave Water and Energy Balance Experiment: April 18 through June 13, 2005. Tech. rep.



- Jiménez, C., Prigent, C., Mueller, B., Seneviratne, S. I., McCabe, M. F., Wood, E. F., Rossow, W. B., Balsamo, G., Betts, A. K., Dirmeyer, P. A., Fisher, J. B., Jung, M., Kanamitsu, M., Reichle, R. H., Reichstein, M., Rodell, M., Sheffield, J., Tu, K., & Wang, K. (2011). Global intercomparison of 12 land surface heat flux estimates. *Journal of Geophysical Research: Atmospheres*, 116. <https://doi.org/10.1029/2010JD014545>
- Joerg, H. (2018). *Multi-Frequency Polarimetric SAR Tomography for the 3-D Characterization and Monitoring of Agricultural Crops* (Doctoral Thesis). ETH Zurich.
- Joerg, H., Pardini, M., Hajnsek, I., & Papathanassiou, K. P. (2018). Sensitivity of SAR Tomography to the Phenological Cycle of Agricultural Crops at X-, C-, and L-band. *IEEE Journal of Selected Topics in Applied Earth Observations and Remote Sensing*, 11(9), 3014–3029. <https://doi.org/10.1109/JSTARS.2018.2845127>
- Joseph, A. T., van der Velde, R., O'Neill, P. E., Lang, R. H., & Gish, T. (2008). Soil Moisture Retrieval During a Corn Growth Cycle Using L-Band (1.6 GHz) Radar Observations. *IEEE Transactions on Geoscience and Remote Sensing*, 46(8), 2365–2374. <https://doi.org/10.1109/TGRS.2008.917214>
- Joseph, A. T., van der Velde, R., O'Neill, P. E., Lang, R., & Gish, T. (2010). Effects of corn on C- and L-band radar backscatter: A correction method for soil moisture retrieval. *Remote Sensing of Environment*, 114(11), 2417–2430. <https://doi.org/10.1016/j.rse.2010.05.017>
- Kabela, E. D., Hornbuckle, B. K., Cosh, M. H., Anderson, M. C., & Gleason, M. L. (2009). Dew frequency, duration, amount, and distribution in corn and soybean during SMEX05. *Agricultural and Forest Meteorology*, 149(1), 11–24. <https://doi.org/10.1016/j.agrformet.2008.07.002>
- Khabbazan, S., Steele-Dunne, S. C., Vermunt, P., Judge, J., Vreugdenhil, M., & Gao, G. (2022). The influence of surface canopy water on the relationship between L-band backscatter and biophysical variables in agricultural monitoring. *Remote Sensing of Environment*, 268, 112789. <https://doi.org/10.1016/j.rse.2021.112789>
- Khabbazan, S., Vermunt, P., Steele-Dunne, S., & Judge, J. (2021). The Importance of Overpass Time in Agricultural Applications of Radar [ISSN: 2153-7003], In *2021 IEEE International Geoscience and Remote Sensing Symposium IGARSS*. ISSN: 2153-7003. <https://doi.org/10.1109/IGARSS47720.2021.9553391>
- Khabbazan, S., Hosseini, M., Saradjian, M. R., Motagh, M., & Magagi, R. (2015). Accuracy Assessment of IWC Soil Moisture Estimation Model in Different Frequency and Polarization Bands. *Journal of the Indian Society of Remote Sensing*, 43(4), 859–865. <https://doi.org/10.1007/s12524-015-0455-3>
- Khabbazan, S., Vermunt, P. C., Steele-Dunne, S. C., Ratering Arntz, L., Marinetti, C., van der Valk, D., Iannini, L., Molijn, R., Westerdijk, K., & van der Sande, C. (2019). Crop Monitoring Using Sentinel-1 Data: A Case Study from The Netherlands. *Remote Sensing*, 11(16), 1887. <https://doi.org/10.3390/rs11161887>
- Kim, S.-B., Zyl, J. J. v., Johnson, J. T., Moghaddam, M., Tsang, L., Colliander, A., Dunbar, R. S., Jackson, T. J., Jaruwatanadilok, S., West, R., Berg, A., Caldwell, T., Cosh, M. H., Goodrich, D. C., Livingston, S., López-Baeza, E., Rowlandson, T., Thibeault, M., Walker, J. P., ... Yueh, S. H. (2017). Surface Soil Moisture Retrieval Using the L-Band Synthetic Aperture Radar Onboard the Soil Moisture Active–Passive Satellite and Evaluation at Core Validation Sites. *IEEE Transactions on Geoscience*

- and Remote Sensing*, 55(4), 1897–1914. <https://doi.org/10.1109/TGRS.2016.2631126>
- Kim, Y., Jackson, T., Bindlish, R., Lee, H., & Hong, S. (2012). Radar Vegetation Index for Estimating the Vegetation Water Content of Rice and Soybean. *IEEE Geoscience and Remote Sensing Letters*, 9(4), 564–568. <https://doi.org/10.1109/LGRS.2011.2174772>
- Kim, Y., & van Zyl, J. J. (2009). A Time-Series Approach to Estimate Soil Moisture Using Polarimetric Radar Data. *IEEE Transactions on Geoscience and Remote Sensing*, 47(8), 2519–2527. <https://doi.org/10.1109/TGRS.2009.2014944>
- Kimes, D. S., & Kirchner, J. A. (1983). Diurnal variations of vegetation canopy structure. *International Journal of Remote Sensing*, 4(2), 257–271. <https://doi.org/10.1080/01431168308948545>
- Klamerus-Iwan, A., Link, T. E., Keim, R. F., & Van Stan II, J. T. (2020). Storage and Routing of Precipitation Through Canopies (I. Van Stan John T., E. Gutmann, & J. Friesen, Eds.). In I. Van Stan John T., E. Gutmann, & J. Friesen (Eds.), *Precipitation Partitioning by Vegetation: A Global Synthesis*. Cham, Springer International Publishing. [https://doi.org/10.1007/978-3-030-29702-2\\_2](https://doi.org/10.1007/978-3-030-29702-2_2)
- Köcher, P., Horna, V., & Leuschner, C. (2013). Stem water storage in five coexisting temperate broad-leaved tree species: Significance, temporal dynamics and dependence on tree functional traits. *Tree Physiology*, 33(8), 817–832. <https://doi.org/10.1093/treephys/tpt055>
- Konings, A. G., Rao, K., & Steele-Dunne, S. C. (2019). Macro to micro: Microwave remote sensing of plant water content for physiology and ecology. *New Phytologist*, 223(3), 1166–1172. <https://doi.org/10.1111/nph.15808>
- Konings, A. G., Saatchi, S. S., Frankenberg, C., Keller, M., Leshyk, V., Anderegg, W. R. L., Humphrey, V., Matheny, A. M., Trugman, A., Sack, L., Agee, E., Barnes, M. L., Binks, O., Cawse-Nicholson, K., Christoffersen, B. O., Entekhabi, D., Gentine, P., Holtzman, N. M., Katul, G. G., ... Zuidema, P. A. (2021). Detecting forest response to droughts with global observations of vegetation water content. *Global Change Biology*, 27(23), 6005–6024. <https://doi.org/10.1111/gcb.15872>
- Konings, A. G., Yu, Y., Xu, L., Yang, Y., Schimel, D. S., & Saatchi, S. S. (2017). Active microwave observations of diurnal and seasonal variations of canopy water content across the humid African tropical forests. *Geophysical Research Letters*, 44(5), 2290–2299. <https://doi.org/10.1002/2016GL072388>
- Kurum, M., Lang, R. H., O'Neill, P. E., Joseph, A. T., Jackson, T. J., & Cosh, M. H. (2009). L-Band Radar Estimation of Forest Attenuation for Active/Passive Soil Moisture Inversion. *IEEE Transactions on Geoscience and Remote Sensing*, 47(9), 3026–3040. <https://doi.org/10.1109/TGRS.2009.2026641>
- Langensiepen, M., Fuchs, M., Bergamaschi, H., Moreshet, S., Cohen, Y., Wolff, P., Jutzi, S. C., Cohen, S., Rosa, L. M. G., Li, Y., & Fricke, T. (2009). Quantifying the uncertainties of transpiration calculations with the Penman–Monteith equation under different climate and optimum water supply conditions. *Agricultural and Forest Meteorology*, 149(6), 1063–1072. <https://doi.org/10.1016/j.agrformet.2009.01.001>



- Leblon, B., Kasischke, E., Alexander, M., Doyle, M., & Abbott, M. (2002). Fire Danger Monitoring Using ERS-1 SAR Images in the Case of Northern Boreal Forests. *Natural Hazards*, 27(3), 231–255. <https://doi.org/10.1023/A:1020375721520>
- Li, J., & Wang, S. (2018). Using SAR-Derived Vegetation Descriptors in a Water Cloud Model to Improve Soil Moisture Retrieval. *Remote Sensing*, 10(9), 1370. <https://doi.org/10.3390/rs10091370>
- Li, Z.-L., Leng, P., Zhou, C., Chen, K.-S., Zhou, F.-C., & Shang, G.-F. (2021). Soil moisture retrieval from remote sensing measurements: Current knowledge and directions for the future. *Earth-Science Reviews*, 218, 103673. <https://doi.org/10.1016/j.earscirev.2021.103673>
- Liao, T.-H., Kim, S.-B., Tan, S., Tsang, L., Su, C., & Jackson, T. J. (2016). Multiple scattering effects with cyclical correction in active remote sensing of vegetated surface using vector radiative transfer theory. *IEEE Journal of Selected Topics in Applied Earth Observation and Remote Sensing*, 9(4), 1414–1429. <https://doi.org/10.1109/JSTARS.2015.2505638>
- Link, M., Jagdhuber, T., Ferrazzoli, P., Guerriero, L., & Entekhabi, D. (2022). Relationship Between Active and Passive Microwave Signals Over Vegetated Surfaces [Conference Name: IEEE Transactions on Geoscience and Remote Sensing]. *IEEE Transactions on Geoscience and Remote Sensing*, 60, 1–15. <https://doi.org/10.1109/TGRS.2021.3053586>
- Liu, L., Shao, Y., Li, K., & Gong, H. (2012). A two layer water cloud model, In *2012 IEEE International Geoscience and Remote Sensing Symposium*. <https://doi.org/10.1109/IGARSS.2012.6352281>
- Liu, P.-W. (2013). Integration of active and passive microwave signatures for characterization of soil properties [PhD Dissertation]. University of Florida.
- Liu, P.-W., Judge, J., DeRoo, R. D., England, A. W., Bongiovanni, T., & Luke, A. (2016). Dominant backscattering mechanisms at l-band during dynamic soil moisture conditions for sandy soils. *Remote Sensing of Environment*, 178, 104–112. <https://doi.org/10.1016/j.rse.2016.02.062>
- Mahdianpari, M., Mohammadimanesh, F., McNairn, H., Davidson, A., Rezaee, M., Salehi, B., & Homayouni, S. (2019). Mid-season crop classification using dual-, compact-, and full-polarization in preparation for the radarsat constellation mission (rcm). *Remote Sensing*, 11(13), 1582. <https://doi.org/10.3390/rs11131582>
- Maltese, A., Awada, H., Capodici, F., Ciruolo, G., La Loggia, G., & Rallo, G. (2018). On the Use of the Eddy Covariance Latent Heat Flux and Sap Flow Transpiration for the Validation of a Surface Energy Balance Model. *Remote Sensing*, 10(2), 195. <https://doi.org/10.3390/rs10020195>
- Mao, J., Fu, W., Shi, X., Ricciuto, D. M., Fisher, J. B., Dickinson, R. E., Wei, Y., Shem, W., Piao, S., Wang, K., Schwalm, C. R., Tian, H., Mu, M., Arain, A., Ciais, P., Cook, R., Dai, Y., Hayes, D., Hoffman, F. M., . . . Zhu, Z. (2015). Disentangling climatic and anthropogenic controls on global terrestrial evapotranspiration trends. *Environmental Research Letters*, 10(9), 094008. <https://doi.org/10.1088/1748-9326/10/9/094008>

- Matar, J., Rodriguez-Cassola, M., Krieger, G., López-Dekker, P., & Moreira, A. (2020). MEO SAR: System Concepts and Analysis. *IEEE Transactions on Geoscience and Remote Sensing*, 58(2), 1313–1324. <https://doi.org/10.1109/TGRS.2019.2945875>
- Matzler, C. (1994). Microwave (1-100 GHz) dielectric model of leaves. *IEEE Transactions on Geoscience and Remote Sensing*, 32(4), 947–949. <https://doi.org/10.1109/36.298024>
- McDonald, K. C., Dobson, M. C., & Ulaby, F. T. (1990). Using MIMICS to model L-band multiangle and multitemporal backscatter from a walnut orchard. *IEEE Trans. Geosci. Remote Sens.*, 28(4), 477–491. <https://doi.org/10.1109/TGRS.1990.572925>
- McDonald, K. C., Zimmermann, R., & Kimball, J. S. (2002). Diurnal and spatial variation of xylem dielectric constant in Norway Spruce (*Picea abies* [L.] Karst.) as related to microclimate, xylem sap flow, and xylem chemistry. *IEEE Trans. Geosci. Remote Sens.*, 40(9), 2063–2082. <https://doi.org/10.1109/TGRS.2002.803737>
- McDonald, K. C., Zimmermann, R., Way, J., & Oren, R. A. M. (1992). An investigation of the relationship between tree water potential and dielectric constant. *Proc. 12th Annu. IGARSS*, 523–525. <https://doi.org/10.1109/IGARSS.1992.576758>
- McNairn, H., Jiali Shang, Xianfeng Jiao, & Champagne, C. (2009). The Contribution of ALOS PALSAR Multipolarization and Polarimetric Data to Crop Classification. *IEEE Transactions on Geoscience and Remote Sensing*, 47(12), 3981–3992. <https://doi.org/10.1109/TGRS.2009.2026052>
- Meier, W., Bleiholder, H., Buhr, L., Feller, C., Hack, H., Heß, M., P.D. Lancashire, Schnock, U., Stauß, R., Van den Boom, T., Weber, E., & Zwerger, P. (2009). The BBCH system to coding the phenological growth stages of plants – history and publications –. *Journal für Kulturpflanzen*, 61(2), 41–52.
- Meinzer, F. C., James, S. A., & Goldstein, G. (2004). Dynamics of transpiration, sap flow and use of stored water in tropical forest canopy trees. *Tree Physiology*, 24(8), 901–909. <https://doi.org/10.1093/treephys/24.8.901>
- Mengen, D., Brogi, C., & Jakobi, J. (2021). The Sarsense Campaign: Air- and Space-Borne C- and L-Band SAR for the Analysis of Soil and Plant Parameters in Agriculture. *Remote Sensing*, 13, 825. <https://doi.org/10.3390/rs13040825>
- Mercier, A., Betbeder, J., Baudry, J., Le Roux, V., Spicher, F., Lacoux, J., Roger, D., & Hubert-Moy, L. (2020). Evaluation of sentinel-1 and 2 time series for predicting wheat and rapeseed phenological stages. *ISPRS Journal of Photogrammetry and Remote Sensing*, 163, 231–256. <https://doi.org/10.1016/j.isprsjprs.2020.03.009>
- METER Group Inc. (2019). PHYTOS 31, Dielectric Leaf Wetness Sensor, Product Manual. METER Group Inc., Pullman, WA, USA.
- Mironov, V., Dobson, M., Kaupp, V., Komarov, S., & Kleshchenko, V. (2004). Generalized refractive mixing dielectric model for moist soils. *IEEE Transactions on Geoscience and Remote Sensing*, 42(4), 773–785. <https://doi.org/10.1109/TGRS.2003.823288>
- Modanesi, S., Massari, C., Gruber, A., Lievens, H., Tarpanelli, A., Morbidelli, R., & De Lannoy, G. J. M. (2021). Optimizing a backscatter forward operator using Sentinel-1 data over irrigated land. *Hydrology and Earth System Sciences*, 25(12), 6283–6307. <https://doi.org/10.5194/hess-25-6283-2021>

- Momen, M., Wood, J. D., Novick, K. A., Pangle, R., Pockman, W. T., McDowell, N. G., & Konings, A. G. (2017). Interacting Effects of Leaf Water Potential and Biomass on Vegetation Optical Depth. *Journal of Geophysical Research: Biogeosciences*, *122*(11), 3031–3046. <https://doi.org/10.1002/2017JG004145>
- Monsivais-Huertero, A., & Judge, J. (2011). Comparison of Backscattering Models at L-Band for Growing Corn. *IEEE Geoscience and Remote Sensing Letters*, *8*(1), 24–28. <https://doi.org/10.1109/LGRS.2010.2050459>
- Monsivais-Huertero, A., Liu, P.-W., & Judge, J. (2018). Phenology-Based Backscattering Model for Corn at L-Band. *IEEE Transactions on Geoscience and Remote Sensing*, *56*(9), 4989–5005. <https://doi.org/10.1109/TGRS.2018.2803153>
- Monteith, A. R., Soja, M. J., Ulander, L. M. H., & Eriksson, L. E. B. (2016). BorealScat: A tower-based tomographic and polarimetric radar experiment in the boreal forest at P-, L- and C-band, In *2016 IEEE International Geoscience and Remote Sensing Symposium (IGARSS)*. <https://doi.org/10.1109/IGARSS.2016.7730945>
- Monteith, A. R., & Ulander, L. M. H. (2018). Temporal Survey of P- and L-Band Polarimetric Backscatter in Boreal Forests. *IEEE Journal of Selected Topics in Applied Earth Observations and Remote Sensing*, *11*(10), 3564–3577. <https://doi.org/10.1109/JSTARS.2018.2814825>
- Monteith, A. R., & Ulander, L. M. H. (2021). Temporal Characteristics of P-Band Tomographic Radar Backscatter of a Boreal Forest. *IEEE Journal of Selected Topics in Applied Earth Observations and Remote Sensing*, *14*, 1967–1984. <https://doi.org/10.1109/JSTARS.2021.3050611>
- Mueller, B., Hirschi, M., Jimenez, C., Ciaia, P., Dirmeyer, P. A., Dolman, A. J., Fisher, J. B., Jung, M., Ludwig, F., Maignan, F., Miralles, D. G., McCabe, M. F., Reichstein, M., Sheffield, J., Wang, K., Wood, E. F., Zhang, Y., & Seneviratne, S. I. (2013). Benchmark products for land evapotranspiration: LandFlux-EVAL multi-data set synthesis. *Hydrology and Earth System Sciences*, *17*(10), 3707–3720. <https://doi.org/10.5194/hess-17-3707-2013>
- Nagarajan, K., Liu, P., DeRoo, R., Judge, J., Akbar, R., Rush, P., Feagle, S., Preston, D., & Terwilliger, R. (2014). Automated L-Band Radar System for Sensing Soil Moisture at High Temporal Resolution. *IEEE Geoscience and Remote Sensing Letters*, *11*(2), 504–508. <https://doi.org/10.1109/LGRS.2013.2270453>
- Narayan, U., Lakshmi, V., & Njoku, E. G. (2004). Retrieval of soil moisture from passive and active L/S band sensor (PALS) observations during the Soil Moisture Experiment in 2002 (SMEX02). *Remote Sensing of Environment*, *92*(4), 483–496. <https://doi.org/10.1016/j.rse.2004.05.018>
- Nelson, J. A., Carvalhais, N., Migliavacca, M., Reichstein, M., & Jung, M. (2018). Water-stress-induced breakdown of carbon–water relations: Indicators from diurnal FLUXNET patterns. *Biogeosciences*, *15*(8), 2433–2447. <https://doi.org/10.5194/bg-15-2433-2018>
- Novick, K. A., Biederman, J. A., Desai, A. R., Litvak, M. E., Moore, D. J. P., Scott, R. L., & Torn, M. S. (2018). The AmeriFlux network: A coalition of the willing. *Agricultural and Forest Meteorology*, *249*, 444–456. <https://doi.org/10.1016/j.agrformet.2017.10.009>

- Oguntunde, P. G., Giesen, N. C. v. d., Vlek, P. L. G., & Eggers, H. (2004). Water Flux in a Cashew Orchard during a Wet-to-Dry Transition Period: Analysis of Sap Flow and Eddy Correlation Measurements. *Earth Interactions*, 8(15), 1–17. [https://doi.org/10.1175/1087-3562\(2004\)8<1:WFIACO>2.0.CO;2](https://doi.org/10.1175/1087-3562(2004)8<1:WFIACO>2.0.CO;2)
- O'Neill, P. E., Chauhan, N. S., & Jackson, T. J. (1996). Use of active and passive microwave remote sensing for soil moisture estimation through corn. *International Journal of Remote Sensing*, 17(10), 1851–1865. <https://doi.org/10.1080/01431169608948743>
- Paget, A. C., Long, D. G., & Madsen, N. M. (2016). RapidScat Diurnal Cycles Over Land. *IEEE Transactions on Geoscience and Remote Sensing*, 54(6), 3336–3344. <https://doi.org/10.1109/TGRS.2016.2515022>
- Paloscia, S., Macelloni, G., Pampaloni, P., & Sigismondi, S. (1999). The potential of C- and L-band SAR in estimating vegetation biomass: The ERS-1 and JERS-1 experiments. *IEEE Transactions on Geoscience and Remote Sensing*, 37(4), 2107–2110. <https://doi.org/10.1109/36.774723>
- Panciera, R., Walker, J. P., Jackson, T. J., Gray, D. A., Tanase, M. A., Ryu, D., Moneris, A., Yardley, H., Rüdiger, C., Wu, X., Gao, Y., & Hacker, J. M. (2014). The Soil Moisture Active Passive Experiments (SMAPEX): Toward Soil Moisture Retrieval From the SMAP Mission. *IEEE Transactions on Geoscience and Remote Sensing*, 52(1), 490–507. <https://doi.org/10.1109/TGRS.2013.2241774>
- Parker, G. (1995). Structure and microclimate of forest canopies (M. Lowman & N. Nadkarny, Eds.). In M. Lowman & N. Nadkarny (Eds.), *Forest Canopies*. San Diego, CA, Academic Press.
- Phillips, N. G., Scholz, F. G., Bucci, S. J., Goldstein, G., & Meinzer, F. C. (2008). Using branch and basal trunk sap flow measurements to estimate whole-plant water capacitance: Comment on Burgess and Dawson (2008). *Plant and Soil*, 315(1), 315–324. <https://doi.org/10.1007/s11104-008-9741-y>
- Pierdicca, N., Davidson, M., Chini, M., Dierking, W., Djavidnia, S., Haarpaintner, J., Hajdich, G., Laurin, G. V., Lavallo, M., López-Martínez, C., Nagler, T., & Su, B. (2019). The Copernicus L-band SAR mission ROSE-L (Radar Observing System for Europe), In *Active and Passive Microwave Remote Sensing for Environmental Monitoring III*, International Society for Optics; Photonics. <https://doi.org/10.1117/12.2534743>
- Porporato, A., Laio, F., Ridolfi, L., & Rodriguez-Iturbe, I. (2001). Plants in water-controlled ecosystems: Active role in hydrologic processes and response to water stress: III. Vegetation water stress. *Advances in Water Resources*, 24(7), 725–744. [https://doi.org/10.1016/S0309-1708\(01\)00006-9](https://doi.org/10.1016/S0309-1708(01)00006-9)
- Poyatos, R., Granda, V., Flo, V., Adams, M. A., Adorján, B., Aguadé, D., Aidar, M. P. M., Allen, S., Alvarado-Barrientos, M. S., Anderson-Teixeira, K. J., Aparecido, L. M., Arain, M. A., Aranda, I., Asbjornsen, H., Baxter, R., Beamesderfer, E., Berry, Z. C., Berveiller, D., Blakely, B., . . . Martínez-Vilalta, J. (2021). Global transpiration data from sap flow measurements: The SAPFLUXNET database. *Earth System Science Data*, 13(6), 2607–2649. <https://doi.org/10.5194/essd-13-2607-2021>
- Qi, Z., Yeh, A. G.-O., Li, X., & Lin, Z. (2012). A novel algorithm for land use and land cover classification using RADARSAT-2 polarimetric SAR data. *Remote Sensing of Environment*, 118, 21–39. <https://doi.org/10.1016/j.rse.2011.11.001>

- Quegan, S., Le Toan, T., Chave, J., Dall, J., Exbrayat, J.-F., Minh, D. H. T., Lomas, M., D'Alessandro, M. M., Paillou, P., Papathanassiou, K., Rocca, F., Saatchi, S., Scipal, K., Shugart, H., Smallman, T. L., Soja, M. J., Tebaldini, S., Ulander, L., Villard, L., & Williams, M. (2019). The European Space Agency BIOMASS mission: Measuring forest above-ground biomass from space. *Remote Sensing of Environment*, 227, 44–60. <https://doi.org/10.1016/j.rse.2019.03.032>
- Rafi, Z., Merlin, O., Le Dantec, V., Khabba, S., Mordelet, P., Er-Raki, S., Amazirh, A., Olivera-Guerra, L., Ait Hssaine, B., Simonneaux, V., Ezzahar, J., & Ferrer, F. (2019). Partitioning evapotranspiration of a drip-irrigated wheat crop: Inter-comparing eddy covariance-, sap flow-, lysimeter- and FAO-based methods. *Agricultural and Forest Meteorology*, 265, 310–326. <https://doi.org/10.1016/j.agrformet.2018.11.031>
- Rahman, I. M. M., & Hasegawa, H. (2012). *Water Stress*. BoD – Books on Demand.
- Reddy, A. R., Chaitanya, K. V., & Vivekanandan, M. (2004). Drought-induced responses of photosynthesis and antioxidant metabolism in higher plants. *Journal of Plant Physiology*, 161(11), 1189–1202. <https://doi.org/10.1016/j.jplph.2004.01.013>
- Reiche, J., Hamunyela, E., Verbesselt, J., Hoekman, D., & Herold, M. (2018). Improving near-real time deforestation monitoring in tropical dry forests by combining dense Sentinel-1 time series with Landsat and ALOS-2 PALSAR-2. *Remote Sensing of Environment*, 204, 147–161. <https://doi.org/10.1016/j.rse.2017.10.034>
- Reichle, R. H., & Koster, R. D. (2004). Bias reduction in short records of satellite soil moisture. *Geophysical Research Letters*, 31(19), L19501. <https://doi.org/10.1029/2004GL020938>
- Rosen, P. A., Kim, Y., Kumar, R., Misra, T., Bhan, R., & Sagi, V. R. (2017). Global persistent SAR sampling with the NASA-ISRO SAR (NISAR) mission, In *2017 IEEE Radar Conference (RadarConf)*. <https://doi.org/10.1109/RADAR.2017.7944237>
- Saatchi, S., Asefi-Najafabady, S., Malhi, Y., Aragão, L. E. O. C., Anderson, L. O., Myneni, R. B., & Nemani, R. (2013). Persistent effects of a severe drought on Amazonian forest canopy. *Proceedings of the National Academy of Sciences*, 110(2), 565–570. <https://doi.org/10.1073/pnas.1204651110>
- Saatchi, S., Halligan, K., Despain, D. G., & Crabtree, R. L. (2007). Estimation of Forest Fuel Load From Radar Remote Sensing. *IEEE Transactions on Geoscience and Remote Sensing*, 45(6), 1726–1740. <https://doi.org/10.1109/TGRS.2006.887002>
- Sakuratani, T. (1981). A Heat Balance Method for Measuring Water Flux in the Stem of Intact Plants. *Journal of Agricultural Meteorology*, 37(1), 9–17. <https://doi.org/10.2480/agrmet.37.9>
- Salas, W. A., Ranson, J. K., Rock, B. N., & Smith, K. T. (1994). Temporal and spatial variations in dielectric constant and water status of dominant forest species from New England. *Remote Sens. Environ.*, 47(2), 109–119. [https://doi.org/10.1016/0034-4257\(94\)90148-1](https://doi.org/10.1016/0034-4257(94)90148-1)
- Santoro, M., Beaudoin, A., Beer, C., Cartus, O., Fransson, J. E. S., Hall, R. J., Pathe, C., Schmullius, C., Schepaschenko, D., Shvidenko, A., Thurner, M., & Wegmüller, U. (2015). Forest growing stock volume of the northern hemisphere: Spatially explicit estimates for 2010 derived from Envisat ASAR. *Remote Sensing of Environment*, 168, 316–334. <https://doi.org/10.1016/j.rse.2015.07.005>

- Sarabandi, K., & Ulaby, F. T. (1990). A convenient technique for polarimetric calibration of single-antenna radar systems. *IEEE Transactions on Geoscience and Remote Sensing*, 28(6), 1022–1033. <https://doi.org/10.1109/36.62627>
- Satalino, G., Mattia, F., Balenzano, A., Lovergine, F. P., Rinaldi, M., De Santis, A. P., Ruggieri, S., Nafria Garcia, D. A., Gomez, V. P., Ceschia, E., Planells, M., Toan, T. L., Ruiz, A., & Moreno, J. (2018). Sentinel-1 & Sentinel-2 Data for Soil Tillage Change Detection, In *IGARSS 2018 - 2018 IEEE International Geoscience and Remote Sensing Symposium*, Valencia, IEEE. <https://doi.org/10.1109/IGARSS.2018.8519103>
- Schroeder, R., McDonald, K. C., Azarderakhsh, M., & Zimmermann, R. (2016). ASCAT MetOp-A diurnal backscatter observations of recent vegetation drought patterns over the contiguous U.S.: An assessment of spatial extent and relationship with precipitation and crop yield. *Remote Sensing of Environment*, 177, 153–159. <https://doi.org/10.1016/j.rse.2016.01.008>
- Shao, H.-B., Chu, L.-Y., Jaleel, C. A., & Zhao, C.-X. (2008). Water-deficit stress-induced anatomical changes in higher plants. *Comptes Rendus Biologies*, 331(3), 215–225. <https://doi.org/10.1016/j.crv.2008.01.002>
- Stamenković, J., Ferrazzoli, P., Guerriero, L., Tuia, D., & Thiran, J.-P. (2015). Joining a Discrete Radiative Transfer Model and a Kernel Retrieval Algorithm for Soil Moisture Estimation From SAR Data. *IEEE Journal of Selected Topics in Applied Earth Observations and Remote Sensing*, 8(7), 3463–3475. <https://doi.org/10.1109/JSTARS.2015.2432854>
- Steele-Dunne, S. C., Friesen, J., & van de Giesen, N. (2012). Using Diurnal Variation in Backscatter to Detect Vegetation Water Stress. *IEEE Transactions on Geoscience and Remote Sensing*, 50(7), 2618–2629. <https://doi.org/10.1109/TGRS.2012.2194156>
- Steele-Dunne, S. C., Hahn, S., Wagner, W., & Vreugdenhil, M. (2019). Investigating vegetation water dynamics and drought using Metop ASCAT over the North American Grasslands. *Remote Sensing of Environment*, 224, 219–235. <https://doi.org/10.1016/j.rse.2019.01.004>
- Steele-Dunne, S. C., McNairn, H., Monsivais-Huertero, A., Judge, J., Liu, P.-W., & Papatthanassiou, K. (2017). Radar Remote Sensing of Agricultural Canopies: A Review. *IEEE Journal of Selected Topics in Applied Earth Observations and Remote Sensing*, 10(5), 2249–2273. <https://doi.org/10.1109/JSTARS.2016.2639043>
- Stringham, C., Farquharson, G., Castelletti, D., Quist, E., Riggi, L., Eddy, D., & Soenen, S. (2019). The Capella X-band SAR Constellation for Rapid Imaging, In *IGARSS 2019 - 2019 IEEE International Geoscience and Remote Sensing Symposium*. <https://doi.org/10.1109/IGARSS.2019.8900410>
- Swanson, R. H. (1994). Significant historical developments in thermal methods for measuring sap flow in trees. *Agricultural and Forest Meteorology*, 72(1), 113–132. [https://doi.org/10.1016/0168-1923\(94\)90094-9](https://doi.org/10.1016/0168-1923(94)90094-9)
- Thiel, C., Drezet, P., Weise, C., Quegan, S., & Schmullius, C. (2006). Radar remote sensing for the delineation of forest cover maps and the detection of deforestation. *Forestry: An International Journal of Forest Research*, 79(5), 589–597. <https://doi.org/10.1093/forestry/cpl036>



- Thompson, A. A. (2015). Overview of the RADARSAT Constellation Mission. *Canadian Journal of Remote Sensing*, 41(5), 401–407. <https://doi.org/10.1080/07038992.2015.1104633>
- Tian, F., Wigneron, J.-P., Ciais, P., Chave, J., Ogée, J., Peñuelas, J., Ræbild, A., Domec, J.-C., Tong, X., Brandt, M., Mialon, A., Rodriguez-Fernandez, N., Tagesson, T., Al-Yaari, A., Kerr, Y., Chen, C., Myneni, R. B., Zhang, W., Ardö, J., & Fensholt, R. (2018). Coupling of ecosystem-scale plant water storage and leaf phenology observed by satellite. *Nature Ecology & Evolution*, 2(9), 1428–1435. <https://doi.org/10.1038/s41559-018-0630-3>
- Torres, R., Snoeij, P., Geudtner, D., Bibby, D., Davidson, M., Attema, E., Potin, P., Rommen, B., Floury, N., Brown, M., Traver, I. N., Deghaye, P., Duesmann, B., Rosich, B., Miranda, N., Bruno, C., L'Abbate, M., Croci, R., Pietropaolo, A., ... Rostan, F. (2012). GMES Sentinel-1 mission. *Remote Sensing of Environment*, 120, 9–24. <https://doi.org/10.1016/j.rse.2011.05.028>
- Trenberth, K. E., & Asrar, G. R. (2014). Challenges and Opportunities in Water Cycle Research: WCRP Contributions. *Surveys in Geophysics*, 35(3), 515–532. <https://doi.org/10.1007/s10712-012-9214-y>
- Ulaby, F. T., Allen, C. T., Eger, G., & Kanemasu, E. (1984). Relating the microwave backscattering coefficient to leaf area index. *Remote Sensing of Environment*, 14(1), 113–133. [https://doi.org/10.1016/0034-4257\(84\)90010-5](https://doi.org/10.1016/0034-4257(84)90010-5)
- Ulaby, F. T., Bush, T., & Batlivala, P. (1975). Radar response to vegetation II: 8-18 GHz band. *IEEE Transactions on Antennas and Propagation*, 23(5), 608–618. <https://doi.org/10.1109/TAP.1975.1141133>
- Ulaby, F. T. (1974). Radar measurement of soil moisture content. *IEEE Transactions on Antennas and Propagation*, 22(2), 257–265. <https://doi.org/10.1109/TAP.1974.1140761>
- Ulaby, F. T. (1975). Radar response to vegetation. *IEEE Transactions on Antennas and Propagation*, 23(1), 36–45. <https://doi.org/10.1109/TAP.1975.1140999>
- Ulaby, F. T. (1982). Effects of Vegetation Cover on the Radar Sensitivity to Soil Moisture. *IEEE Transactions on Geoscience and Remote Sensing*, GE-20(4), 476–481. <https://doi.org/10.1109/TGRS.1982.350413>
- Ulaby, F. T., & Batlivala, P. P. (1976). Diurnal Variations of Radar Backscatter from a Vegetation Canopy. *IEEE Transactions on Antennas and Propagation*, 24(1), 11–17. <https://doi.org/10.1109/TAP.1976.1141298>
- Ulaby, F. T., & El-rayes, M. A. (1987). Microwave Dielectric Spectrum of Vegetation - Part II: Dual-Dispersion Model. *IEEE Transactions on Geoscience and Remote Sensing*, GE-25(5), 550–557. <https://doi.org/10.1109/TGRS.1987.289833>
- Ulaby, F. T., Sarabandi, K., McDonald, K., Whitt, M., & Dobson, M. C. (1990). Michigan microwave canopy scattering model. *International Journal of Remote Sensing*, 11(7), 1223–1253. <https://doi.org/10.1080/01431169008955090>
- UMS GmbH. (2011). T4/T4e Pressure Transducer Tensiometer, User Manual. UMS GmbH, München, Germany.
- van Dijk, A. I. J. M., Gash, J. H., van Gorsel, E., Blanken, P. D., Cescatti, A., Emmel, C., Gielen, B., Harman, I. N., Kiely, G., Merbold, L., Montagnani, L., Moors, E., Sotocornola, M., Varlagin, A., Williams, C. A., & Wohlfahrt, G. (2015). Rainfall in-

- terception and the coupled surface water and energy balance. *Agricultural and Forest Meteorology*, 214-215, 402–415. <https://doi.org/10.1016/j.agrformet.2015.09.006>
- van Emmerik, T., Steele-Dunne, S. C., Judge, J., & Giesen, N. v. d. (2015). Impact of Diurnal Variation in Vegetation Water Content on Radar Backscatter From Maize During Water Stress. *IEEE Transactions on Geoscience and Remote Sensing*, 53(7), 3855–3869. <https://doi.org/10.1109/TGRS.2014.2386142>
- van Emmerik, T., Steele-Dunne, S. C., Paget, A., Oliveira, R. S., Bittencourt, P. R. L., Barros, F. d. V., & Giesen, N. v. d. (2017). Water stress detection in the Amazon using radar. *Geophysical Research Letters*, 44(13), 6841–6849. <https://doi.org/10.1002/2017GL073747>
- Veloso, A., Mermoz, S., Bouvet, A., Le Toan, T., Planells, M., Dejoux, J.-F., & Ceschia, E. (2017). Understanding the temporal behavior of crops using Sentinel-1 and Sentinel-2-like data for agricultural applications. *Remote Sensing of Environment*, 199, 415–426. <https://doi.org/10.1016/j.rse.2017.07.015>
- Vermunt, P. C., Khabbazan, S., Steele-Dunne, S. C., Judge, J., Monsivais-Huertero, A., Guerriero, L., & Liu, P.-W. (2020). Response of Subdaily L-Band Backscatter to Internal and Surface Canopy Water Dynamics. *IEEE Transactions on Geoscience and Remote Sensing*, 59(9), 7322–7337. <https://doi.org/10.1109/TGRS.2020.3035881>
- Vermunt, P. C., Steele-Dunne, S. C., Khabbazan, S., Judge, J., & van de Giesen, N. C. (2022). Extrapolating continuous vegetation water content to understand sub-daily backscatter variations. *Hydrology and Earth System Sciences*, 26(5), 1223–1241. <https://doi.org/10.5194/hess-26-1223-2022>
- Vreugdenhil, M., Wagner, W., Bauer-Marschallinger, B., Pfeil, I., Teubner, I., Rüdiger, C., & Strauss, P. (2018). Sensitivity of Sentinel-1 Backscatter to Vegetation Dynamics: An Austrian Case Study. *Remote Sensing*, 10(9), 1396. <https://doi.org/10.3390/rs10091396>
- Wang, L., & Qu, J. J. (2009). Satellite remote sensing applications for surface soil moisture monitoring: A review. *Frontiers of Earth Science in China*, 3(2), 237–247. <https://doi.org/10.1007/s11707-009-0023-7>
- Weber, J., & Ustin, S. (1991). Diurnal water relations of walnut trees: Implications for remote sensing. *IEEE Transactions on Geoscience and Remote Sensing*, 29(6), 864–874. <https://doi.org/10.1109/TGRS.1991.1019470>
- Wood, D., McNairn, H., Brown, R. J., & Dixon, R. (2002). The effect of dew on the use of RADARSAT-1 for crop monitoring: Choosing between ascending and descending orbits. *Remote Sensing of Environment*, 80(2), 241–247. [https://doi.org/10.1016/S0034-4257\(01\)00304-2](https://doi.org/10.1016/S0034-4257(01)00304-2)
- Woodhouse, I. H. (2017). *Introduction to Microwave Remote Sensing*. Boca Raton, CRC Press. <https://doi.org/10.1201/9781315272573>
- Xu, X., Konings, A. G., Longo, M., Feldman, A., Xu, L., Saatchi, S., Wu, D., Wu, J., & Moorcroft, P. (2021). Leaf surface water, not plant water stress, drives diurnal variation in tropical forest canopy water content. *New Phytologist*, 231(1), 122–136. <https://doi.org/10.1111/nph.17254>



- Ye, N., Walker, J. P., Wu, X., de Jeu, R., Gao, Y., Jackson, T. J., Jonard, F., Kim, E., Merlin, O., Pauwels, V. R. N., Renzullo, L. J., Rüdiger, C., Sabaghy, S., von Hebel, C., Yueh, S. H., & Zhu, L. (2021). The Soil Moisture Active Passive Experiments: Validation of the SMAP Products in Australia. *IEEE Transactions on Geoscience and Remote Sensing*, 59(4), 2922–2939. <https://doi.org/10.1109/TGRS.2020.3007371>
- Yebra, M., Scortechini, G., Badi, A., Beget, M. E., Boer, M. M., Bradstock, R., Chuvieco, E., Danson, F. M., Dennison, P., Resco de Dios, V., Di Bella, C. M., Forsyth, G., Frost, P., Garcia, M., Hamdi, A., He, B., Jolly, M., Kraaij, T., Martín, M. P., . . . Ustin, S. (2019). Globe-LFMC, a global plant water status database for vegetation eco-physiology and wildfire applications. *Scientific Data*, 6(1), 155. <https://doi.org/10.1038/s41597-019-0164-9>
- Yu, Y., & Saatchi, S. (2016). Sensitivity of L-Band SAR Backscatter to Aboveground Biomass of Global Forests. *Remote Sensing*, 8(6), 522. <https://doi.org/10.3390/rs8060522>
- Zhang, Z., Tian, F., Hu, H., & Yang, P. (2014). A comparison of methods for determining field evapotranspiration: Photosynthesis system, sap flow, and eddy covariance. *Hydrology and Earth System Sciences*, 18(3), 1053–1072. <https://doi.org/10.5194/hess-18-1053-2014>
- Zimmermann, R., McDonald, K., Oren, R., & Way, J. (1995). Xylem dielectric constant, water status, and transpiration of young Jack Pine (*Pinus banksiana* Lamb.) in the southern boreal zone of Canada. *Proc. IGARSS*, 2, 1006–1008.
- Zotarelli, L., Dukes, M. D., Romero, C. C., Migliaccio, K. W., & Morgan, K. (2010). Step by Step Calculation of the Penman-Monteith Evapotranspiration (FAO-56 Method), Institute of Food and Agricultural Sciences, University of Florida, FL, USA.



# ACKNOWLEDGEMENTS

This part of the book concerns the thanks I owe to the many persons who have contributed directly or indirectly to this work.

First and foremost, Susan, I am extremely grateful to you for giving me the opportunity and the confidence to work on your Vidi project. I have enjoyed the responsibilities you have given me during the field campaigns. Thank you for your critical questions, quick responses, scientific discussions, sharing your experience, your enthusiasm for the research, sense of humour and for always seeing possibilities.

Nick, bedankt voor je rake adviezen tijdens de progress meetings, die me dwongen om na te denken over het grotere plaatje: van proefschrift tot carrière. En natuurlijk voor je suggesties voor Hoofdstuk 4.

I owe special thanks to Saeed Khabbazan, with whom I worked in tandem on the research objectives of the project. Saeed, I admire your flexibility to co-organize and execute the field experiments under tiring conditions, and I appreciate that you shared your expertise on microwave remote sensing with me. Our time together in the field and in Florida left me with tons of memories.

Many thanks to the people from UF center for Remote Sensing. Thank you Jasmeet for giving us the opportunity to become part of your group, as well as your hospitality and advice for our papers. A huge thanks for making sure we had L-band data from the UF-LARS system! I also wish to thank Daniel, Pat, Rachel, Fernando, Shar, Hamideh, Ratna, Allegra, Eduardo, Karin and other colorful people I met in Gainesville for the very warm welcome, introduction to The Gator Nation, help, fun and hospitality. Daniel, I am grateful for your help in many difficult situations. I also appreciate the help from Alvin, Juan, Jim and their team in Citra. Thanks all for making my time in Florida an unforgettable experience.

Ik heb veel te danken aan Jacob van den Borne en Paul van Zoggel voor hun interesse in het project, en voor het bieden van de kans om ons experimenteel onderzoek voort te zetten in Reusel. Ik waardeer hun gastvrijheid en de hulp van hun team en studenten. Ook ben ik dank verschuldigd aan Thom Bogaard en Armand Middeldorp voor het helpen faciliteren van ons labwerk in het WaterLab.

I am indebted to Leila Guerriero for her patience and time to carefully explain me the details and possibilities of the Tor Vergata model. Hopefully, we can meet in person in the future. I also wish to thank Pang-Wei Liu, Roger de Roo and Alex Monsivais-Huertero for teaching me valuable information about the UF-LARS system, and Michael van Bavel, for answering my questions about the sap flow system.

Special thanks to all members of the examination committee for the time they have taken to assess this dissertation. I am also grateful to the 11 reviewers of the peer-reviewed journal articles in this dissertation, whose comments greatly improved the chapters and forced me to think from different perspectives.

The past few years wouldn't have been the same without some amazing people I met at the TU. I would like to express my gratitude to all my colleagues of the Water Management department. Bas dT, Juancho, Boran, Laurène, Jerom, Monica, David A., Gaby, David S., Ties, Vineet, Ruud, Bart, Wim, Bas W., Luuk, Fransje, Chelsea, Martin, Erik, Coco, Judith, Lydia, and all the other staff, short-term visitors and students: thanks for the enjoyable time on the fourth floor, during the lunch walks, in Luxembourg, at parties, and at EGU! Thank you Lydia, Betty, Tamara and Fleur for arranging all the logistics that come with a PhD project. Also thanks to those who joined the Thursday drinks at/outside PSOR. Despite the pandemic and the related restrictions, I will particularly remember all the good times with you!

En tot slot de mensen die misschien weinig met mijn werk te maken hebben, maar zeer belangrijk zijn voor het relativeren van alles wat met werk te maken heeft. Mijn vrienden wil ik graag bedanken voor de humor en gesprekken in de weekenden en tijdens avonden, activiteiten, vakanties en feestjes. Bedankt (schoon)familie voor de interesse en de goede zorgen. In het bijzonder mam, pap en Dorith: ik heb veel gehad aan jullie optimisme, advies en steun, met name tijdens de laatste loodjes. Imme, ik ben dankbaar voor onze avonturen, je gevraagd en ongevraagd advies, maar bovenal, voor je liefde en vrolijkheid.

*Paul*

*Utrecht, February 2022*

# CURRICULUM VITÆ

## Paul Christian VERMUNT

24-08-1992      Born in Etten-Leur, The Netherlands.

### EDUCATION

2017–2022      Ph.D. in Water Resources Management  
Delft University of Technology  
*Thesis:*      Understanding radar backscatter sensitivity to vegetation water dynamics: sub-daily variations in ground-based experiments  
*Promoters:* Prof. dr. ir. Susan C. Steele-Dunne  
Prof. dr. ir. Nick C. van de Giesen

2014–2016      M.Sc. in Hydrology  
Utrecht University

2010–2013      B.Sc. in Environmental Sciences  
Utrecht University

2004–2010      Gymnasium  
Katholieke Scholengemeenschap Etten-Leur



# LIST OF PUBLICATIONS

## PEER-REVIEWED JOURNAL ARTICLES

4. **Vermunt, P. C.**, Steele-Dunne, S. C., Khabbazan, S., Judge, J., and Van de Giesen, N. C. (2022). Extrapolating Continuous Vegetation Water Content To Understand Sub-daily Backscatter Variations, *Hydrology and Earth System Sciences* **26**, 1223-1241 .
3. **Vermunt, P. C.**, Khabbazan, S., Steele-Dunne, S. C., Judge, J., Monsivais-Huertero, A., Guerriero, L., and Liu, P. W. (2020). Response of Subdaily L-Band Backscatter to Internal and Surface Canopy Water Dynamics, *IEEE Transactions on Geoscience and Remote Sensing* **59**, (9), 7322 - 7337.
2. Khabbazan, S., Steele-Dunne, S. C., **Vermunt, P. C.**, Judge, J., Vreugdenhil, M., and Gao G. (2022). The influence of surface canopy water on the relationship between L-band backscatter and biophysical variables in agricultural monitoring, *Remote Sensing of Environment* **268**, 112789.
1. Khabbazan, S., **Vermunt, P. C.**, Steele-Dunne, S. C., Ratering Arntz, L., Marinetti, C., Van der Valk, D., Iannini, L., Molijn, R., Westerdijk, K. and Van der Sande, C. (2019). Crop monitoring using Sentinel-1 data: a case study from The Netherlands, *Remote Sensing* **11**, (16), 1887.

## JOURNAL ARTICLES IN REVIEW

1. **Vermunt, P. C.**, S. Khabbazan, S. C. Steele-Dunne, V. Kumar, and J. Judge. Towards Understanding the Role of Dynamic Vertical Canopy Moisture Distribution on Radar Backscatter Dynamics. *Remote Sensing*, in review.

## CONFERENCE PAPERS

2. Khabbazan, S., **Vermunt, P. C.**, Steele-Dunne, S. C. and Judge, J. The Importance of Overpass Time in Agricultural Applications of Radar. *IGARSS 2021*, pp. 6084-6087.
1. Steele-Dunne, S. C., Khabbazan, S., **Vermunt, P. C.**, Ratering Arntz, L., Marinetti, C., Iannini, L., Westerdijk, K. and Van der Sande, C. Monitoring Key Agricultural crops in the Netherlands using Sentinel-1. *IGARSS 2018*, pp. 6639-6642.



